Characterization of the Mechanisms Underlying Cell Surface ACE2 Receptor Modulation by Seasonal Human Coronavirus NL63

Caroline Silveira Falleiros Silva

Thesis submitted to the University of Ottawa in partial fulfillment of the requirements for the Master's degree in Microbiology and Immunology.

Supervisor: Dr. Marc-André Langlois

Department of Biochemistry, Microbiology and Immunology
Microbiology and Immunology Graduate Program
Faculty of Medicine
University of Ottawa

ABSTRACT

Seasonal human coronaviruses, including sHCoV-NL63, sHCoV-229E, sHCoV-OC43, and sHCoV-HKU1, belong to the Coronaviridae family. While typically causing mild respiratory infections, sHCoVs can trigger severe complications in vulnerable populations. Among them, sHCoV-NL63 uses the ACE2 receptor, the same entry receptor used by SARS-CoV-2. Previous work from our laboratory showed that sHCoV-NL63 upregulates the ACE2 receptor after infection, potentially increasing the risk of co-infection and of emerging recombinants. The mechanisms underlying this regulation of ACE2 expression remain unknown. This study investigated whether individual sHCoV-NL63 viral proteins modulate ACE2 surface expression. Expression vectors encoding individual sHCoV-NL63 proteins were transfected into HEK293T+ACE2 and LLC-MK2 permissive cell lines. These were used to analyze protein expression and ACE2 receptor levels by fluorescence microscopy, flow cytometry and western blot. While most viral proteins were successfully expressed, none significantly increased ACE2 surface expression, suggesting that ACE2 receptor regulation may depend on coordinated events associated with productive viral infection and/or the cell-intrinsic antiviral response. Further investigation of viral proteases, host cell signalling pathways, and interferon responses may help elucidate the mechanisms responsible for ACE2 receptor modulation.

ACKNOWLEGMENTS

I think it took me longer to write these acknowledgments than the thesis itself. There were so many moments, so many lessons learned, like a rollercoaster of emotions, that it becomes difficult to put into words what the heart has to say.

First, I would like to thank my supervisor, Marc-André Langlois. I am deeply grateful for the opportunity and the trust placed in me. I truly believe God blessed me by giving me the chance to be mentored by you. You are much more than just a supervisor to your students. No matter how busy you are, you always find the time to guide us through every step of the process. I hope I have met your expectations. ``YOU WERE LIKE YODA TEACHING A JEDI DISCOVERING THE FORCE.´´

When I started my master's degree, I had just finished my honours project, and I truly thought I knew what it meant to be a researcher. Looking back, I realize I had no idea. To be honest, I think I only truly understood what research really is while writing this thesis. It took me two years, but better late than never.

These past two years have been filled with every emotion imaginable and countless hours of troubleshooting experiments, but they have also given me incredible opportunities to grow, both personally and professionally.

I would also like to extend my gratitude to the entire lab and core facility. Especially to Negar, for all her guidance, patience and help with experiments; To Nicholas, for helping me at crucial points in my project; To Isaac, for dedicating valuable time to help me when I decided to process almost 90 samples in a single day; and to Amparo, who is like the mother of the lab, always giving us her full support and guidance. I also thank Justino and Muhammad for their help whenever I needed it. It genuinely contributed to the success of this research.

This lab became like a second family to me. I am grateful for everyone's encouragement, kindness and friendship. Most importantly, thank you for holding me up when the loss of my sister took the ground out from under me. I will never forget the compassion and support you showed me.

I could never thank my husband, Pablo, enough. You sacrificed so much so that I could pursue this dream. You dedicated yourself alongside me throughout this process, supporting me and never letting me lose heart. Even though science is not your field, you discussed my experiments with me, trying to help me troubleshoot it. ``EU TE AMO PRA SEMPRE, VOCÊ É UM MARIDO INCRÍVEL!!!´´.

I also thank my mother, Ilce, for always encouraging and supporting me in all my dreams. You also played an essential role in the completion of this dream. ``EU TE AMO MUITÃO´´.

To my sister, Tatiana, for listening to hours of me talking about failed experiments and celebrating with me when they finally worked. Even from far away, I was never alone. To my bother, Manoel, who swears that I am a genius, for all his support and encouragement throughout this journey.

I would also like to sincerely thank my examiners, Dr. Seung-Hwan Lee and Dr. Allyson MacLean, for their valuable feedback and thoughtful suggestions, which greatly contributed to improving the quality and clarity of this thesis.

Last, but not least, to my psychologist, Priscila, for guiding my mental health throughout this entire process.

Above all, I thank God for giving me this opportunity and for giving me the resources and people to support me along the way, so that I could reach the promise!

TABLE OF CONTENTS

LIST OF FIGURES

Appendices

LIST OF TABLES

Appendices

LIST OF ABBREVIATIONS

2-5a – 2'-5'-oligoadenylate synthetase

3CLpro – 3C-like protease

ACE – angiotensin-converting enzyme

ACE2 – Angiotensin-converting enzyme 2

ADAM17 - A Disintegrin And Metalloproteinase 17

ANOVA - Analysis of Variance

APN – Aminopeptidase N

BSA – Bovine Serum Albumin

cGAMP – cyclic GMP–AMP / Cyclic guanosine monophosphate–adenosine monophosphate

cGAS – Cyclic GMP–AMP synthase

CMV – cytomegalovirus

CO_2 - Carbon dioxide

CPE - cytopathic effect

dACE2 – deltaACE2 / truncated ACE2 isoform

DMEM - Dulbecco's Modified Eagle Medium

DMVs – Double membrane vesicles

DNA - Deoxyribonucleic Acid

DPI – Days post-infection

dsRNA – Double-stranded RNA

DUB – Deubiquitinase

E – Envelope protein

ECL - enhanced chemiluminescence

EDTA - Ethylenediaminetetraacetic acid

eIF2a – Eukaryotic translation initiation factor 2 alpha

ER – Endoplasmic reticulum

ERGIC – Endoplasmic reticulum Golgi intermediate compartment

FBS – Fetal bovine serum

FITC – fluorescein isothiocyanate (fluorophore)

flACE2 – full-length angiotensin-converting enzyme

FSC - Forward Scatter

GFP – Green fluorescent protein

gMFI – Geometric mean fluorescence intensity

hACE2 – human angiotensin-converting enzyme 2

HCoVs (HCoV) – Human coronaviruses

HLA – human leukocyte antigen

hMPV – human metapneumovirus

HR1 – heptad repeat 1

HR2 – heptad repeat 2

HRP - Horseradish peroxidase

HRSV – human respiratory syncytial virus

HSPGs – Heparan sulfate proteoglycans

IFIT – Interferon Induced proteins with tetratricopeptide repeats

IFN – Interferon

IFNAR – Interferon-α/β receptor

IFNLR – Interferon Lambda Receptor

IKK – Inhibitor of nuclear factor kappa-B kinase

IRES – Internal ribosome entry site

IRF – Interferon regulatory factor

ISG – Interferon-Stimulated Genes

ISGF3 – Interferon-Stimulated Gene Factor

JAK1 – Janus kinase 1

Kb – Kilobase

M – Membrane protein

MAVS – Mitochondrial Antiviral Signaling Protein

MDA5 – Melanoma differentiation-associated protein 5

MDM2 – Murine double minute 2

MEM - Minimum Essential Medium

MERS-CoV - Middle East respiratory syndrome coronavirus

MOI - multiplicity of infection

Mpro – main protease

mRNA – Messenger RNA or messenger ribonucleic acid

MyD88 – Myeloid differentiation primary response gene 88

N – Nucleocapsid protein

NCBI - National Center for Biotechnology Information

NF-kB – nuclear factor kappa B

Nsps – non-structural proteins

OAS – Oligoadenylate Synthetase

ORF1 – Open Reading Frame 1

P/S – Penicillin/Streptomycin

PAMPs – Pathogen associated molecular patterns

PBS – Phosphate-Buffered Saline

PE – phycoerythrin (fluorophore)

pe – Plasmid expressing

PFA – paraformaldehyde

PKR – Protein Kinase R

PLP – Papain-like protease

PLpro – papain-like protease

Pp1a – Polyprotein 1a

Pp1ab – polyprotein 1ab

PRRs – Pattern recognition receptors

PVDF – polyvinylidene fluoride

RAAS – renin–angiotensin–aldosterone system

RBD – receptor-binding domain

RdRp – RNA-Dependent RNA Polymerase

RIG-I – retinoic acid-inducible gene I

RIPA – radioimmunoprecipitation assay buffer

RLRs – RIG-I-like receptors

RNase L – Ribonuclease L

RTC – Replicase transcriptase complex

S – Spike protein

sACE2 – soluble angiotensin-converting enzyme

SARS-CoV - severe acute respiratory syndrome coronavirus

SARS-CoV-2 - severe acute respiratory syndrome coronavirus 2

SDS - Sodium Dodecyl Sulfate

SDS-PAGE – sodium dodecyl sulfate–polyacrylamide gel electrophoresis

sHCoVs (sHCoV) – Seasonal Human Coronaviruses

SSC - Side Scatter

ssRNA – Single-stranded RNA

STAT – Signal transducer and activator of transcription

STING – Stimulator of Interferon Genes

TBK1 – TANK-binding kinase 1

TBST - Tris-buffered saline with Tween 20

TLRs – Toll-like receptors

TMD – transmembrane domain

TMPRSS2 – transmembrane protease serine 2

TRAF – Tumor necrosis factor receptor-associated factors

TRIF – TIR-domain-containing adapter-inducing IFN-β

TYK2 – Tyrosine Kinase 2

INTRODUCTION

Origin of Seasonal Human Coronaviruses

Seasonal human coronaviruses (sHCoVs) belong to a larger group of human coronaviruses (HCoVs), which is composed of seven zoonotic viruses, as illustrated in Figure 1. This group includes the highly pathogenic viruses SARS-CoV, SARS-CoV-2, and MERS-CoV, as well as four endemic viruses referred to as seasonal human coronaviruses, which are sHCoV-NL63, sHCoV-229E, sHCoV-OC43, and sHCoV-HKU1 (Xin Li et al., 2019).

The sHCoV-NL63 and sHCoV-229E are classified within the genus *Alphacoronavirus*, whereas sHCoV-OC43 and sHCoV-HKU1 belong to the *Betacoronavirus* genus. Phylogenetic and evolutionary analyses suggest that sHCoV-NL63 and sHCoV-229E probably originated from bat coronaviruses. In the case of sHCoV-229E, dromedary camels and alpacas have also been identified as potential intermediate hosts. The sHCoV-OC43 is most associated with a bovine origin, with a few papers also mentioning rodents. However, more extensive analyses including open reading frames encoding the envelope, membrane, nucleocapsid, and spike proteins, along with whole-genome sequences, indicate that its origin may go beyond bovine to include murine, rabbit, and canine hosts. In contrast, sHCoV-HKU1 is believed to have originated from a murine coronavirus (Otieno, J.R et al., 2022; Lagacé-Wiens, P et al., 2021). Comparative genomic analyses have demonstrated that recombination rates vary across the genera and among seasonal human coronaviruses. Recombination events have been identified across the coronavirus genome, involving regions encoding both non-structural and structural proteins. One of the most notable locations is the spike protein, associated with viral adaptation, where genetic variation may influence receptor interactions, host specificity, and viral fitness. sHCoV-229E and sHCoV-OC43 display the highest recombination rates, whereas sHCoV-NL63 and sHCoV-HKU1 accumulate more nucleotide substitutions per recombination event, indicating

that the relative contributions of recombination and point mutation to viral evolution differ among sHCoVs. (Otieno, J.R. et al., 2022; Nicola F. Müller et al., 2021).

sHCoV-229E was first identified in 1966 by researchers at the University of Chicago during investigations of respiratory specimens from individuals presenting common cold symptoms. sHCoV-OC43 was subsequently isolated in 1967 from volunteers at the Common Cold Unit in Salisbury, United Kingdom, using nasopharyngeal swab samples. sHCoV-NL63 was discovered in 2004 in the Netherlands in a child presenting with bronchiolitis, coryza, fever, and conjunctivitis. More recently, sHCoV-HKU1 was identified in 2005 in Hong Kong in adult patients diagnosed with pneumonia (van der Hoek et al., 2004; H.F. Boncristiani et al., 2009; Chang-Xing Li et al., 2021; Jeremy Huynh et al., 2012).

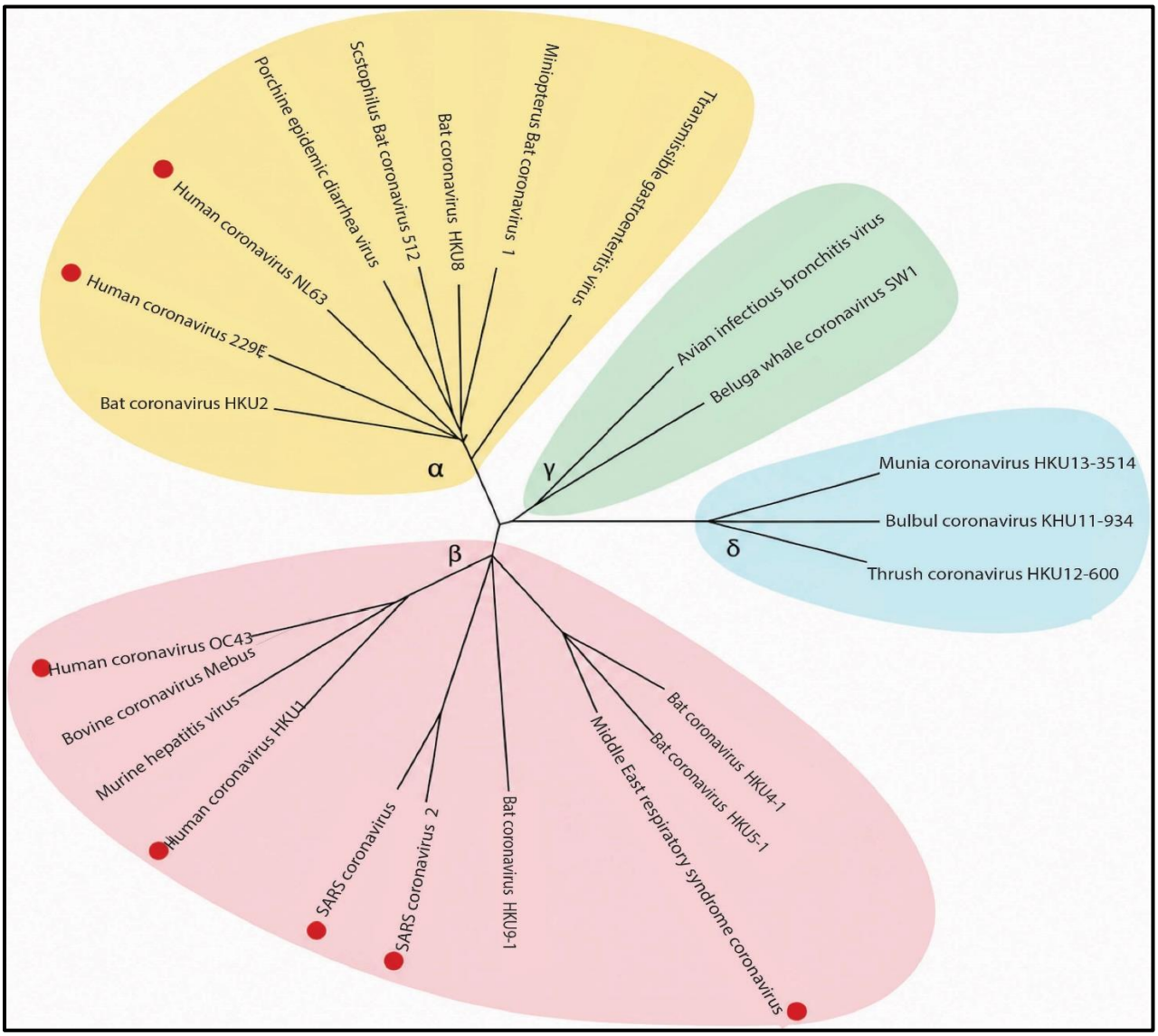

Figure 1. Phylogenetic tree representing members of the Coronaviridae family. Coronaviruses are classified into four genera: *Alphacoronavirus* (α), *Betacoronavirus* (β), *Gammacoronavirus* (γ), and *Deltacoronavirus* (δ). The human coronaviruses are highlighted with red circles and include the seasonal human coronaviruses sHCoV-NL63, sHCoV-229E, sHCoV-OC43, and sHCoV-HKU1, as well as the highly pathogenic coronaviruses SARS-CoV, SARS-CoV-2, and MERS-CoV. Reproduced and adapted figure from Lamkiewicz et al. (2023).

Transmission and Pathogenesis

Seasonal human coronaviruses have successfully established endemic circulation due to characteristics, as illustrated in Figure 2, that facilitate persistent transmission, such as efficient human-to-human transmission, widespread global circulation, and relatively low disease severity. sHCoVs are estimated to be responsible for approximately 5% to 30% of all human respiratory tract infections. Their circulation typically begins in late October, reaches its highest level by the end of January or early February, remains highly active between January and March, and gradually declines until early June (Harrison, C.M et al., 2023; Lagacé-Wiens P et al., 2021; Marie E. et al., 2006; Rory Wilson et al., 2024). Across epidemiological studies, sHCoV-OC43 has been the most prevalent circulating species among the sHCoVs, followed by sHCoV-NL63, sHCoV-229E, and sHCoV-HKU1. In addition, some epidemiological reviews show that the majority of the test positivity rates for sHCoV-OC43 and sHCoV-NL63 were observed among pediatric populations, whereas sHCoV-229E and sHCoV-HKU1 were more frequently detected among adults (Rory Wilson et al., 2024; Ye R-Z, Gong C et al., 2023).

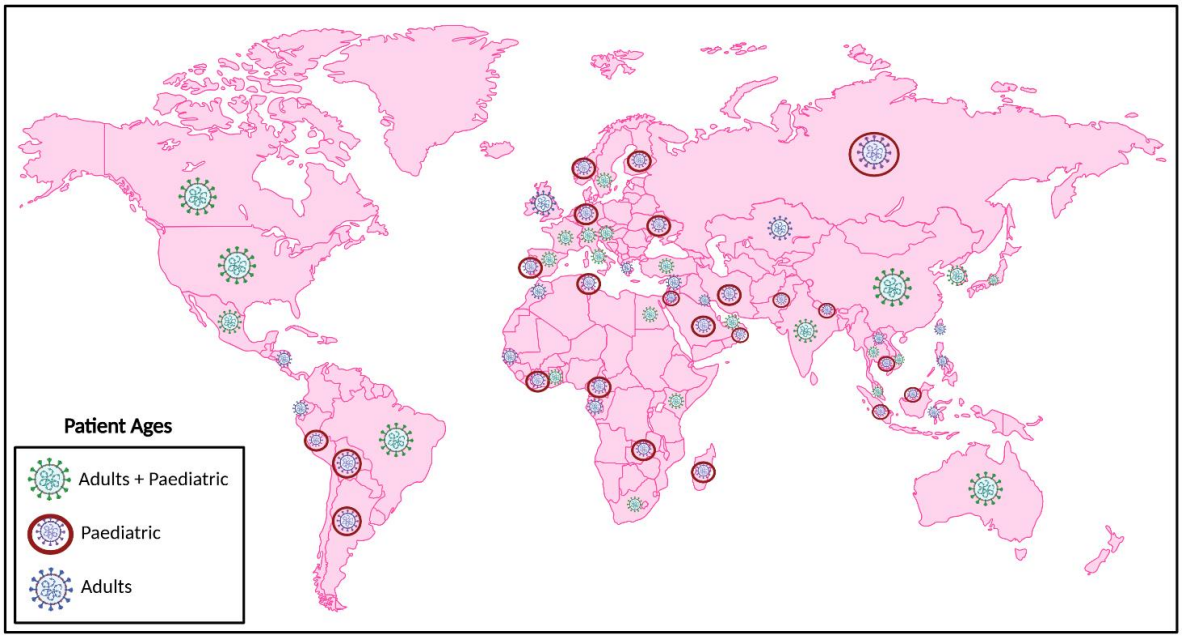

Figure 2. Geographical Distribution of Seasonal Human Coronaviruses Based on Published Reports. Geographical representation of studies reporting seasonal human coronavirus infections, classified according to the age group of included participants (adults, pediatric patients, or both). Author's illustration, adapted from published data (Su et al., 2016; Wilson et al., 2024).

Human coronaviruses are transmitted predominantly via respiratory droplets. Additional routes of transmission include direct contact with contaminated surfaces and the fecal-oral route (Andrew G et al., 2020; Ye et al., 2020).

The clinical manifestations are similar among the seasonal human coronaviruses. Common symptoms include malaise, headache, runny nose, sneezing, sore throat, fever, and cough, with an incubation period ranging from approximately 2 to 5 days. In more severe cases, sHCoV-NL63 is associated with tachypnea, hypoxia, and obstructive laryngitis symptoms, whereas sHCoV-HKU1 has also led to dyspnea. While seasonal human coronavirus infections are typically mild, they may progress to more severe disease in young children, the elderly, and immunocompromised individuals (Chang-Xing Li et al., 2022; Lia Van Der Hoek et al., 2006).

Single infections with seasonal human coronaviruses have been associated only with respiratory outcomes. Nevertheless, isolated exceptions have been reported. For instance, one patient with a single sHCoV-HKU1 infection developed meningitis, whereas another patient infected only with sHCoV-OC43 experienced seizures (Lia Van Der Hoek et al., 2006; Esper F et al., 2006).

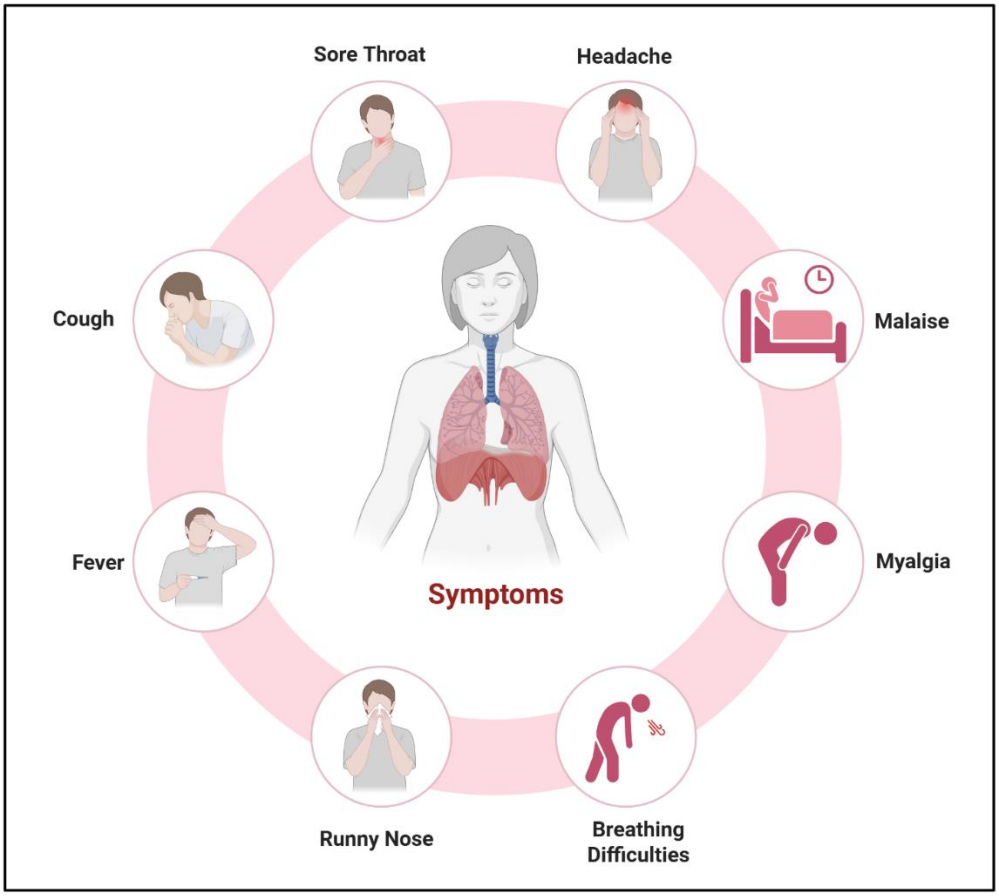

Figure 3. Symptoms associated with seasonal human coronavirus infections. Common clinical manifestations include respiratory symptoms such as cough, sore throat, runny nose, and breathing difficulties, as well as systemic symptoms including fever, headache, malaise, and myalgia (Author's illustration).

Epidemiological studies have shown that coinfection with other respiratory viruses, including human respiratory syncytial virus (HRSV), human metapneumovirus (hMPV), and influenza viruses, is relatively common, occurring in 11% to 41% of coronavirus-positive respiratory samples. Interestingly, patients with sHCoV-NL63 coinfections exhibit significantly lower viral loads than patients infected exclusively with sHCoV-NL63. There are a few possible explanations for this: one is direct competition between respiratory viruses for the same target cells within the respiratory tract. Another hypothesis is that the innate immune response induced by one respiratory virus suppresses sHCoV-NL63 replication. It is also possible that sHCoV-NL63 establishes infection before the second infection, and by the time the subsequent virus produces clinical symptoms, the sHCoV-NL63 infection may already be under effective immune control, resulting in reduced viral replication. Nevertheless, coinfections have been reported more frequently among hospitalized patients than among outpatients, suggesting that the detection of an additional respiratory virus may be associated with more severe disease (van der Hoek et al., 2005; A Koetz et al., 2006; Huang et al., 2017).

The occurrence of coinfection between seasonal human coronaviruses and SARS-CoV-2 has been documented in a few clinical settings. However, it is considered rarer compared with other respiratory viruses.

Case reports have identified simultaneous infections involving sHCoV-OC43 and sHCoV-HKU1 in patients with underlying comorbidities. The reports of symptom aggravation are still not clear, but there is concern due to the increased release of inflammatory cytokines, which may affect disease severity (Mponponsuo et al., 2023; Madaras et al., 2025; Chuang et al., 2020). Although some studies have found no significant difference in disease severity between SARS-CoV-2 monoinfection and coinfection with other respiratory viruses, severe outcomes have occasionally been reported (Chekuri et al., 2021; Carstens et al., 2025). A case report from Hong Kong described a patient with comorbidities who progressed to a fatal outcome while presenting coinfection with SARS-CoV-2

and sHCoV-229E (Lau SKP et al., 2021). Furthermore, studies conducted in different regions, including Korea and Iran, have documented the continued circulation of sHCoVs alongside SARS-CoV-2, with reported cases involving sHCoV-229E, sHCoV-NL63, and sHCoV-OC43. These observations support the importance of comprehensive screening to better assess the potential impact of these viral interactions on disease progression (Roh et al., 2021; Valian et al., 2021).

Viral Entry Receptor

Even though the sHCoVs are from the same family, they use different entry receptors. sHCoV-229E uses aminopeptidase N (APN)/CD13, a zinc-dependent metallopeptidase membrane protein with multiple biological functions that include enzyme activity, receptor activity, and immune signalling (Nwokolo et al., 2025; Lim, Ng, Tam, & Liu, 2016; Lu et al., 2020). sHCoV-OC43 and sHCoV-HKU1 recognize glycan-based receptors carrying 9-O-acetylated sialic acid, a key factor for metallopeptidases for entry. Besides the receptor role, its exact function is not well-defined. However, evidence suggests that sialoglycans have a role in cell surface and glycoprotein protection against proteases, formation of blood vessel lumen, and immune cell trafficking (R.J.G. Hulswit et al., 2019; Tomris I et al., 2024; Visser et al., 2021). Nevertheless, sHCoV-NL63 utilizes angiotensin-converting enzyme 2 (ACE2) for cell entry, which is also a metallopeptidase membrane protein that modulates inflammatory immune responses and oxidative stress and acts as a receptor. ACE2 is a key entry point for SARS-CoV-2, suggesting a potential overlap in receptor usage between seasonal and pandemic-causing coronaviruses (Devarakonda CKV et al., 2020; Lim, Ng, Tam, & Liu, 2016; Amelimojarad & Amelimojarad, 2025).

Recent studies have attempted to better understand the cell entry mechanisms of the seasonal human coronaviruses. One of them, working with lentiviral pseudovirus-based models, showed that sHCoV-NL63, sHCoV-229E, and sHCoV-HKU1 rely primarily on endosomal entry mechanisms rather than cellular serine protease activity. These findings indicate that

proteolytic activation of the spike proteins can occur through cathepsins within the endosomal compartment. They also demonstrated that arginine residues located at the S1/S2 cleavage site were necessary for efficient entry of sHCoV-NL63 and sHCoV-229E but were dispensable for sHCoV-HKU1 (Sabari Nath Neerukonda et al., 2025).

Another recent study on structural and functional analyses demonstrated that the sHCoV-HKU1 spike glycoprotein initiates infection by interacting with host cell surface sialoglycans and requires transmembrane protease serine 2 (TMPRSS2) to promote more efficient viral entry. However, the absence of TMPRSS2 does not inhibit viral entry (McCallum et al., 2024; Sabari Nath Neerukonda et al., 2025).

In contrast, sHCoV-OC43 has been reported to bind either cell surface sialic acids or HLA class I molecules for internalization. Viral entry then occurs through caveolae-mediated endocytosis rather than clathrin-mediated endocytosis. (Owczarek et al., 2018; Szczepański et al., 2019).

sHCoV-NL63 and sHCoV-229E Structure

sHCoV-NL63 and sHCoV-229E are enveloped, non-segmented, positive-sense single-stranded RNA viruses belonging to the *Alphacoronavirus* genus. Their genomes range from approximately 27 to 30 kb. The virions are spherical particles of approximately 120 nm in diameter, surrounded by a lipid envelope that contains the major structural proteins, including the spike (S), membrane (M), envelope (E), and nucleocapsid (N) proteins. The viral genome contains two large open reading frames, ORF1a and ORF1b. sHCoVs encode accessory proteins that vary between viral species. sHCoV-NL63 contains accessory protein 3 (P3), whereas sHCoV-229E encodes accessory proteins 4 (4A and 4B) (Otieno et al., 2022; Liu, Liang, & Fung, 2021; van der Hoek L, Pyrc, & Berkhout, 2006; National Center for Biotechnology Information [NCBI], n.d.; ViralZone, n.d.).

The genomic organization of sHCoV-NL63 follows the order: 5'-cap-ORF1a-ORF1b-S-ORF3-E-M-N-poly(A) tail-3' and consists of 27,553 bp. The ORF1ab encodes 16 non-structural proteins (nsps), including nsp3, which encodes the Papain-Like Protease or PLpro (PLP1 and PLP2), responsible for cleaving from nsp1 to nsp3, and nsp5, which encodes the Main Protease or Mpro, also known as 3C-like proteinase or 3CLpro, responsible for cleaving from nsp4 to nsp16. Additionally, the nsp12 encodes the RNA-dependent RNA polymerase (RdRp), and nsp13 encodes Helicase (Figure 4) (National Center for Biotechnology Information [NCBI], n.d.; Chazal N et al., 2021; Pyrc, 2005), whereas sHCoV-229E displays the genomic arrangement: 5'-cap-ORF1a-ORF1b-S-ORF4-E-M-N-poly(A) tail-3', with a total genome size of 27,317 bp. Similar to sHCoV-NL63, the ORF1ab encodes 16 nsps, including nsp3 encoding Papain-Like Protease or PLpro (PLP1 and PLP2), responsible for cleaving from nsp1 to nsp3, and nsp5, which encodes the Main Protease or Mpro/ also known as the 3C-like proteinase or 3CLpro, responsible for cleaving from nsp4 to nsp16. Additionally, nsp12 encodes the RNA-dependent RNA polymerase (RdRp), and nsp13 encodes Helicase (Figure 5) (National Center for Biotechnology Information [NCBI], n.d.; ViralZone, n.d.).

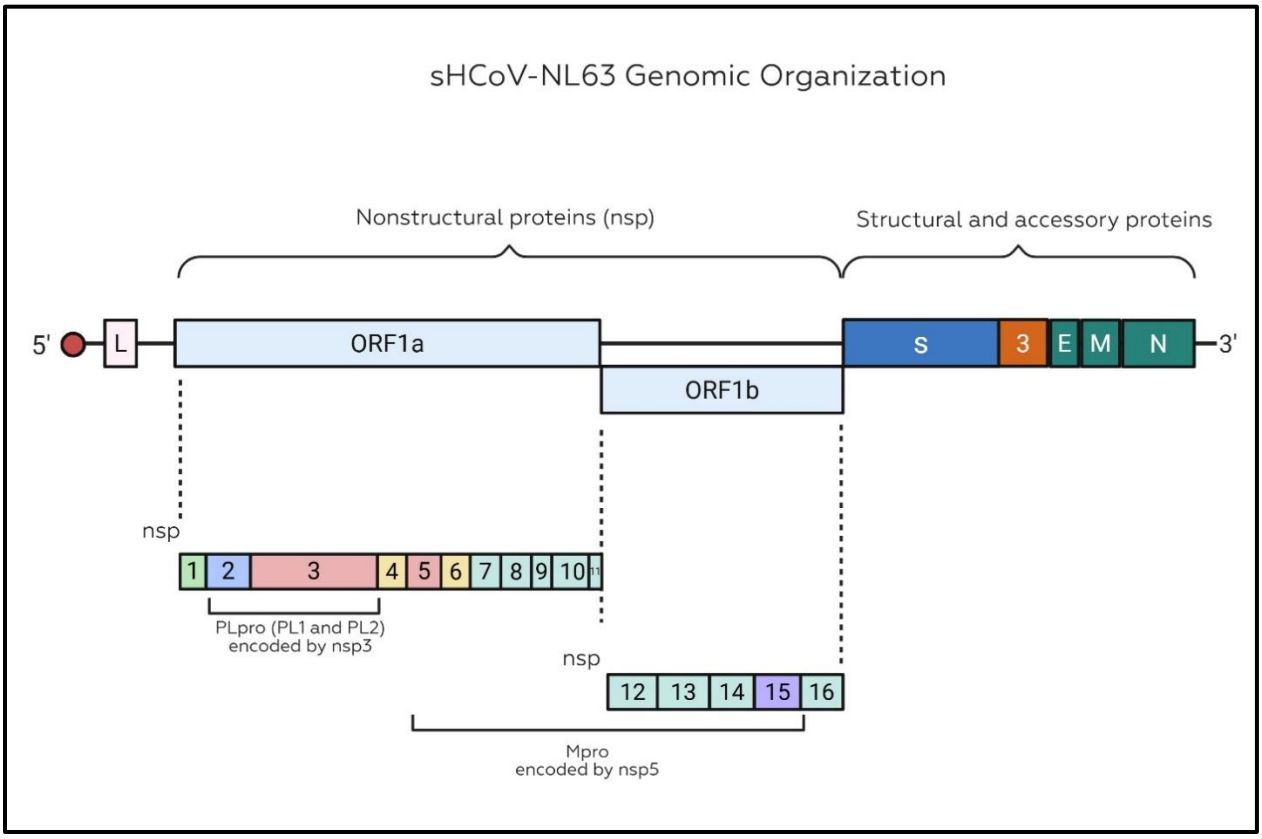

Figure 4. Genomic organization of seasonal human coronavirus NL63 (sHCoV-NL63). Schematic representation of the sHCoV-NL63 genome (27.5 kb), showing the genomic arrangement 5'-cap-ORF1a-ORF1b-S-ORF3-E-M-N-poly(A) tail-3'. The ORF1a/ORF1b region encodes 16 non-structural proteins (nsps), including the viral proteases PLpro (nsp3; PLP1/PLP2) and Mpro/3CLpro (nsp5), as well as key components of the replication-transcription complex, including RNA-dependent RNA polymerase (RdRp, nsp12) and helicase (nsp13). The sequence also includes spike (S), protein 3 (3), membrane (M), envelope (E), and nucleocapsid (N) proteins. Adapted from NCBI (n.d.), Chazal et al. (2021), and Pyrc (2005).

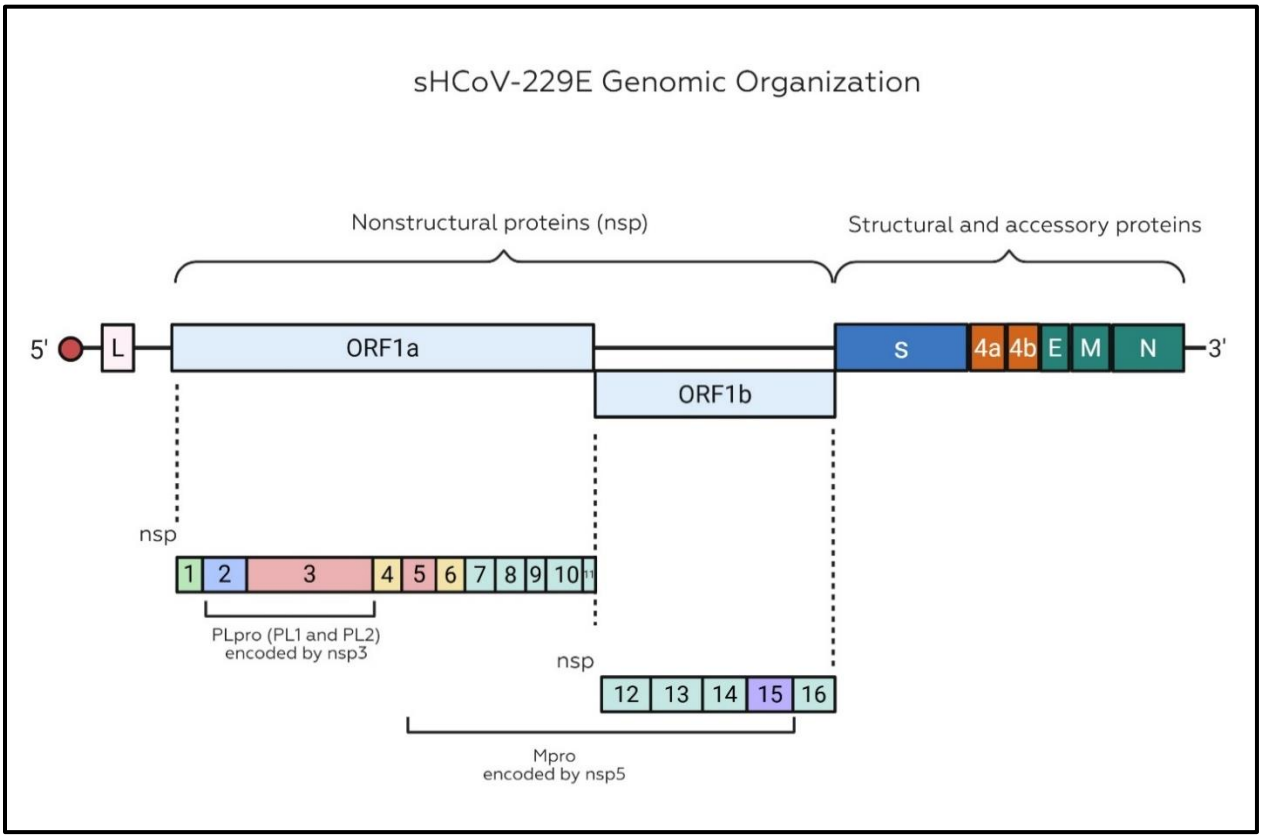

Figure 5. Genomic organization of seasonal human coronavirus 229E (sHCoV-229E). Schematic representation of the sHCoV-229E genome (27.3 kb), showing the genomic arrangement 5'-cap-ORF1a-ORF1b-S-ORF4-E-M-N-poly(A) tail-3'. Similar to sHCoV-NL63, the ORF1a/ORF1b region encodes 16 non-structural proteins (nsps), including the viral proteases PLpro (nsp3; PLP1/PLP2) and Mpro/3CLpro (nsp5), together with replication-associated proteins such as RdRp (nsp12) and helicase (nsp13). The sequence also includes spike (S), protein 4A (4a), protein 4B (4b), membrane (M), envelope (E), and nucleocapsid (N) proteins. Adapted from NCBI (n.d.) and ViralZone (n.d.).

Structural Proteins

The spike (S) glycoprotein is the viral surface protein responsible for mediating host cell attachment and membrane fusion. It is a large type I transmembrane glycoprotein that forms a homotrimer and is organized as a single-pass integral membrane protein, consisting of an extracellular N-terminal domain, a single transmembrane segment, and a cytoplasmic C-terminal domain. Following N-linked glycosylation, the S protein has an approximate molecular

weight of 150 kDa (Tsai et al., 2025; Zhang et al., 2020; Li, 2016). During viral entry, the S protein requires proteolytic activation by host proteases, including endosomal cathepsins, which cleave the protein at specific sites such as the S1/S2 junction (Neerukonda et al., 2024). The N-terminal S1 subunit contains the receptor-binding domain (RBD), which undergoes structural changes between closed and open (nonactivated and activated) conformations to facilitate interaction with host receptors (Song et al., 2021). The S2 subunit contains the conserved fusion machinery required for membrane fusion. Following proteolytic activation, conformational rearrangements within S2 expose the fusion peptide, allowing its insertion into the host membrane. Subsequent refolding of the heptad repeat regions HR1 and HR2 brings viral and cellular membranes into close proximity, promoting membrane fusion and viral entry (Walls et al., 2016; Zhang et al., 2020).

The membrane (M) protein represents the most abundant structural component of the coronavirus envelope and is essential for virion assembly by interacting with other structural proteins such as S, N, and E and morphogenesis. Additionally, it may contribute to virus–host interactions, including attachment processes involving molecules such as heparan sulfate proteoglycans (HSPGs). This approximately 27 kDa protein forms homodimers and contains a short N-terminal ectodomain that undergoes N-linked glycosylation, a modification important for protein stability and function (de Haan CAM et al., 2000; Naskalska A et al., 2019; Arndt ALLarson BJ et al., 2010; Castillo G et al., 2023).

The Nucleocapsid (N) protein is a multifunctional protein that plays essential roles throughout the coronavirus replication cycle. With an approximate molecular weight of 43 kDa, the N protein consists of two major domains: the N-terminal domain primarily interacts with viral RNA, while the C-terminal domain promotes N–N interactions required for oligomer formation (Tang et al., 2005; Szelazek et al., 2017). The N protein forms dimers that bind and encapsulate the viral genome, assembling into a helical ribonucleoprotein complex that provides structural

protection and helps shield the viral genome from host-mediated degradation (Xiao et al., 2025).

The Envelope (E) protein is the smallest structural protein, with a molecular weight of approximately 10 kDa. It consists of a short N-terminal region, a hydrophobic transmembrane domain (TMD), and a longer C-terminal domain (Sučec et al., 2024). The E protein functions as a viroporin. Through modulation of ion homeostasis and calcium signalling, it contributes to membrane remodelling, efficient virion assembly, and viral particle release (Schoeman & Fielding, 2019; Ye & Hogue, 2007).

Accessory Proteins

The sHCoV-NL63 protein 3 (P3), encoded by ORF3, has a predicted molecular weight of approximately 26 kDa. P3 is characterized as a transmembrane protein containing three predicted membrane-spanning domains, meaning that the protein is predicted to cross the lipid bilayer three times (Müller et al., 2010). In silico analyses have suggested a potential role for P3 in viral infectivity and pathogenesis. Additionally, experimental studies have indicated that P3 may contribute to viral assembly, showing its importance during the coronavirus replication cycle (Abdul-Rasool & Fielding, 2010; Fielding, B. C., & Suliman, T.,2009).

The sHCoV-229E accessory protein 4, encoded by ORF4, is often found split into two distinct open reading frames, ORF4a and ORF4b, having molecular weights of about 16 kDa and 11kDa, respectively. Their functions are not well established. However, one study proposed that these proteins exhibit ion channel activity, allowing the passage of monovalent cations and potentially contributing to viral production (Zhang et al., 2013; Dijkman et al., 2006).

Non-Structural Proteins (Open Reading Frame / Polyproteins)

The genomes of sHCoV-NL63 and sHCoV-229E consist of positive-sense, single-stranded RNA, containing a 5' cap structure and a 3' poly(A) tail. The 5' proximal region, representing approximately two-thirds of the genome, contains two large open reading frames, ORF1a and ORF1b, which are translated into the replicase polyproteins pp1a and pp1ab through a -1 ribosomal frameshift mechanism. These polyproteins are subsequently processed by viral proteases into approximately 16 individual non-structural proteins. Nsp3 encodes two papain-like protease (PLpro) domains, designated PL1 and PL2, whereas Nsp5 encodes the 3C-like cysteine protease/ Main protease (3CLpro/ Mpro). These nsps subsequently assemble into the replication–transcription complex that is responsible for viral genome replication and the synthesis of subgenomic mRNAs (Ziebuhr, 2005; Lai et al., 2007).

Although the specific functions of all nsps have not been fully characterized in sHCoV-NL63 and sHCoV-229E, studies across the Coronaviridae family have identified several conserved roles for these proteins. Nsp1 is involved in the inhibition of host gene expression, while nsp2 remains less well characterized. Nsp4 and nsp6 are transmembrane proteins involved in the organization of membrane structures associated with viral replication (DMV's formation). Nsp7 and nsp8 support viral RNA synthesis, while nsp9 has RNA-binding activity and nsp10 acts as a cofactor for other viral enzymes. Nsp12 functions as the RNA-dependent RNA polymerase (RdRp), and nsp13 provides helicase activity. Nsp14 contributes to RNA proofreading and RNA cap formation, while nsp15 functions as an endoribonuclease, promoting evasion of dsRNA sensors. Finally, nsp16 provides 2'-O-methyltransferase activity involved in viral RNA cap modification (Fehr & Perlman, 2015; Chen Y et al., 2020).

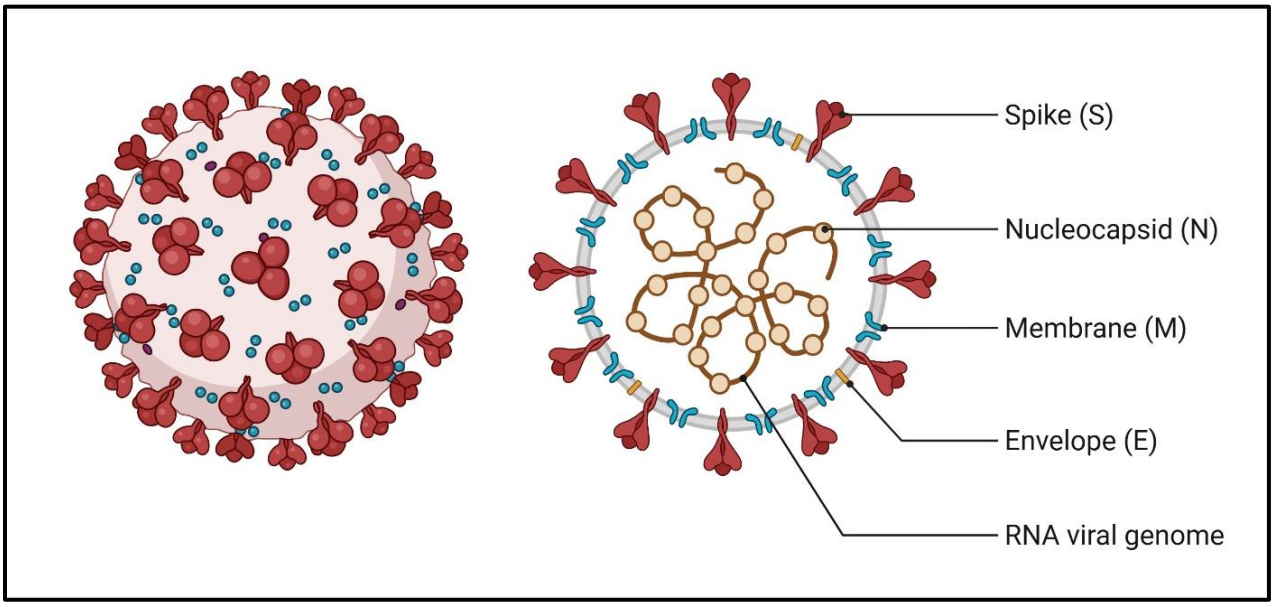

Figure 6. Structure of human coronaviruses. Schematic representation of a coronavirus virion, illustrating the lipid envelope containing the spike (S), membrane (M), and envelope (E) structural proteins, and the viral positive-sense single-stranded RNA (+ssRNA) genome is encapsulated by the nucleocapsid (N) protein. (ViralZone, n.d.).

Viral Replication

The virus initially attaches to the cell surface by interaction between the respective cell receptor and the S protein (S1 region). In some coronaviruses, for instance, the sHCoV-NL63 membrane protein can interact with the heparan sulfate proteoglycans (HSPGs) on the cell surface, acting as a cofactor that stabilizes attachment and facilitates infection. For example, SARS-CoV-2 also interacts with the HSPGs but uses the spike protein rather than the membrane protein, acting as a co-receptor for SARS-CoV-2 infection (Naskalska et al., 2019; De Pasquale et al., 2021). Following attachment, host proteases cleave and activate the S protein, which facilitates viral entry into the cell. The virus is then internalized through clathrin-mediated endocytosis or caveolae-mediated endocytosis. Once inside the cell, the virus goes through uncoating, releasing the viral genome. The positive-sense single-stranded RNA acts as messenger RNA (mRNA) and is translated from the open reading frames (ORF1a and ORF1b)

by the ribosome, producing polyproteins (pp1a and pp1ab). These polyproteins are subsequently cleaved by the viral proteases into nonstructural proteins (nsps), including the RNA-dependent RNA polymerase (RdRp), which assemble into the replicase-transcriptase complex (RTC). At the same time, the nsps remodel endoplasmic reticulum membranes to generate viral replication organelles composed mainly of double-membrane vesicles (DMVs). These membrane structures, which are derived from the endoplasmic reticulum (ER), provide a protected environment where the RTC first synthesizes full-length negative-sense RNA intermediates, followed by subgenomic negative-sense RNAs through discontinuous transcription, which serve as templates for the production of positive-sense genomic RNA and subgenomic mRNAs. These subgenomic mRNAs are translated into structural proteins, Spike (S), Envelope (E), Membrane (M), and Nucleocapsid (N), as well as several accessory proteins. The genomic RNA associates with the N protein to form the nucleocapsid, which is incorporated into the endoplasmic reticulum-Golgi intermediate compartment (ERGIC) containing the S, E, and M proteins, where virion assembly occurs. Mature virions are subsequently transported in secretory vesicles and released from the cell by exocytosis (Bergmann & Silverman, 2020; Fehr & Perlman, 2015; Milewska et al., 2014; Milewska et al., 2018; Castillo et al., 2023).

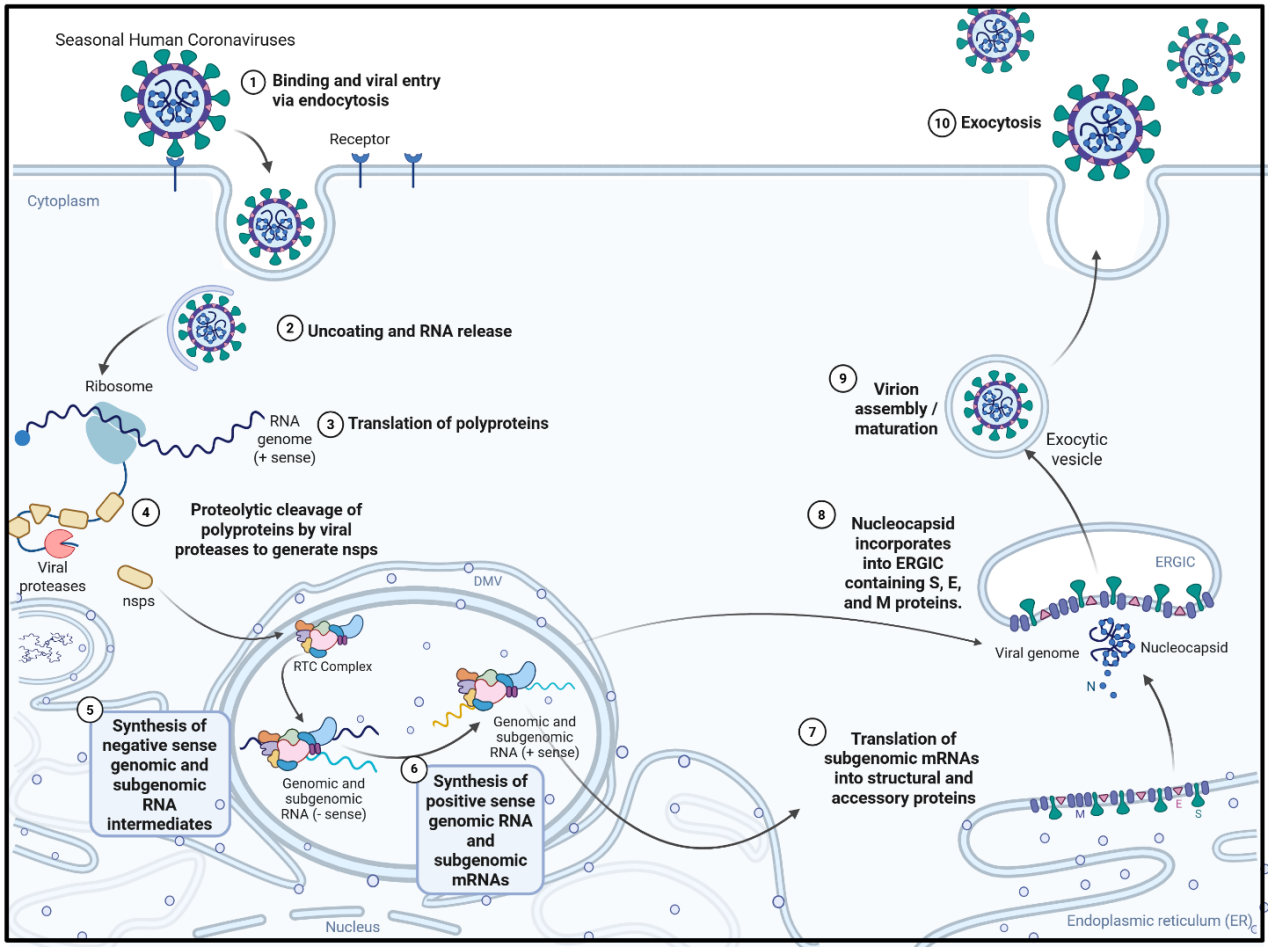

Figure 7. Coronavirus replication cycle. The viral spike (S) protein mediates attachment to host cell receptors, followed by proteolytic activation and viral entry. The viral genome is released into the cytoplasm and translated into viral proteins, including components of the replicase–transcriptase complex. Synthesized structural proteins are incorporated into the ERGIC membrane, where nucleocapsid assembly and virion budding occur. Mature virions are transported through the secretory pathway and released by exocytosis from the host cell. (Author's illustration – inspired by Misbah S et al., 2020; Mingaleeva, R.N et al., 2022; da Silva Torres MK et al., 2022).

Viral Immune Response

During the early phase of infection, the innate immune system recognizes the virus through pattern recognition receptors (PRRs). Following viral entry, the RTC synthesizes negative-sense RNA. The positive-sense RNA is transcribed and replicated to form the viral genome. This

process leads to the formation of single-stranded RNA (ssRNA) and double-stranded RNA (dsRNA) that are recognized as pathogen-associated molecular patterns (PAMPs). The PRRs sense viral RNA in different cellular compartments. In the cytoplasm, RIG-I-like receptors (RLRs), such as retinoic acid-inducible gene I (RIG-I), are involved in the detection of short RNA, and melanoma differentiation-associated protein 5 (MDA5) in the detection of longer RNA. Activated RIG-I and MDA5 interact with Mitochondrial Antiviral Signalling Protein (MAVS), which recruits tumor necrosis factor receptor-associated factors (TRAF) that activate threonine-protein kinase (TBK1) and inhibitor of nuclear factor kappa-B kinase (IKKε), which phosphorylate and activate interferon regulatory factor 3 (IRF3) and nuclear factor kappa-B (NF-KB), promoting the production of pro-inflammatory cytokines and type I and III interferons (IFN-β, IFN-α and IFN-λ). At the same time, in the endosome, Toll-like receptors (TLRs), especially TLR3 for detection of dsRNA and TLR7 for detection of ssRNA, contribute to viral sensing. These receptors recruit signalling adaptor proteins such as TIR-domain-containing adapter-inducing IFN-β (TRIF) for TLR3 and myeloid differentiation primary response gene 88 (MYD88) for TLR7, activating TBK1, IKKε or IKKα, IKKβ, and IKKγ, respectively, forming signalling complexes. These complexes activate intracellular signalling cascades involving IRF3 and IRF7 or NF-κB, which are essential for controlling viral replication in the initial stages (Ohto U, Shimizu T., 2016; Yan et al., 2021; Zhuang et al., 2020; Duan T et al., 2022; Khatun, Kaur & Tripathi, 2025; Zhu, Chiang & Gack, 2023; Tanneti, Stillwell & Weiss, 2025; Zhao X et al,. 2022). IFN-I (IFN-α and IFN-β) binds to the interferon-α/β receptor (IFNAR), whereas IFN-III (IFN-λ) binds to Interferon Lambda Receptor (IFNLR), activating the JAK–STAT signalling pathway, including Janus kinase 1 (JAK1), Tyrosine Kinase 2 (TYK2), and signal transducer and activator of transcription 1 and 2 (STAT1 and STAT2). STAT1 and STAT2 form a complex with IRF9, known as Interferon-Stimulated Gene Factor 3 (ISGF3), which drives the transcription of Interferon-Stimulated Genes (ISGs). These genes encode antiviral proteins that

inhibit multiple steps of the viral life cycle (Kim & Shin, 2021; Zhuang et al., 2020; Islamuddin M et al., 2022).

Some examples of ISGs that possibly play a role in sHCoVs are Protein Kinase R (PKR), which is induced by interferon, acts as a PRR recognizing dsRNA, and leads to its autophosphorylation and subsequent phosphorylation of eukaryotic translation initiation factor (eIF2α), which interferes with protein synthesis. Another interesting ISG that plays a role in viral replication is Oligoadenylate Synthetase (OAS), which detects dsRNA and induces the production of 2'-5'-oligoadenylate synthetase (2-5A), activating Ribonuclease L (RNase L), promoting both host and viral RNA degradation (Fausto A et al., 2026; Tanneti NS et al., 2025).

Cyclic GMP–AMP synthase (cGAS) is a DNA sensor that detects foreign dsDNA. RNA viruses can indirectly activate the cGAS–STING pathway through mitochondrial DNA release or cellular stress, influencing antiviral and inflammatory responses during infection. Recognition of DNA activates the enzymatic activity of cGAS, resulting in cGAMP synthesis. cGAMP subsequently binds STING and initiates downstream signalling involving TBK1 and IRF3, ultimately promoting a type I IFN response (Hopfner, KP et al., 2020).

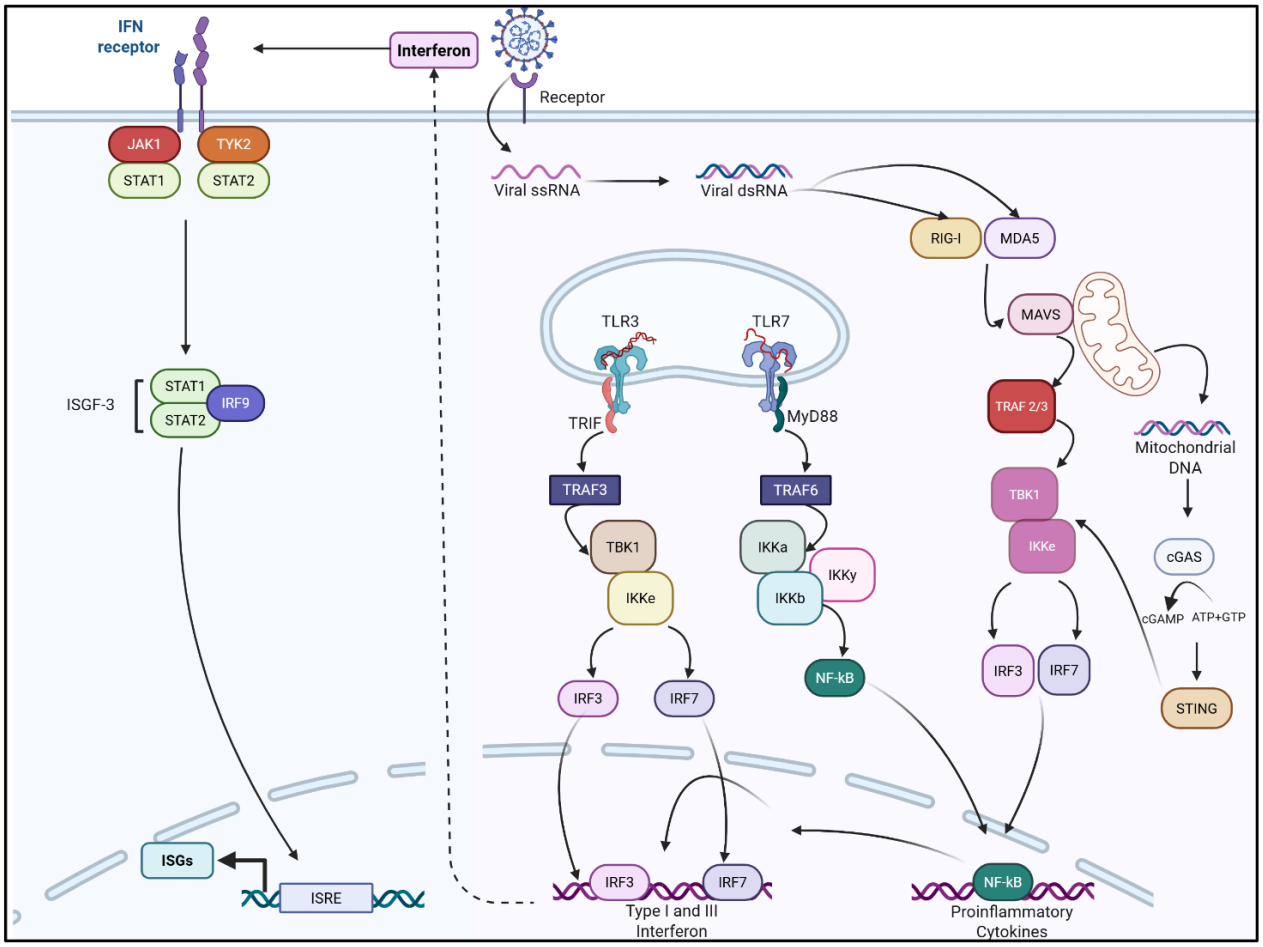

Figure 8. Innate immune recognition of seasonal human coronaviruses and activation of the interferon response. Viral ssRNA and dsRNA replication intermediates are recognized by cytoplasmic RIG-I-like receptors (RIG-I and MDA5) and endosomal Toll-like receptors (TLR3 and TLR7), activating signalling pathways that lead to the activation of IRF3, IRF7, and NF-κB. These transcription factors induce the production of type I (IFN-α/β) and type III (IFN-λ) interferons, as well as pro-inflammatory cytokines. Interferons bind to their respective receptors, activating the JAK–STAT pathway and the ISGF3 complex (STAT1–STAT2–IRF9), which promotes the expression of interferon-stimulated genes (ISGs) attempting to establish an antiviral state. (Author's illustration – inspired by Zhao X et al., 2022; Islamuddin M et al., 2022).

Coronavirus Innate Immune Evasion Mechanism

Coronaviruses have evolved multiple mechanisms to evade the host innate immune response. Although the efficiency of these strategies differs among coronavirus species and contributes to differences in pathogenicity, several immune evasion mechanisms are conserved across them. One of the most common and conserved mechanisms among coronaviruses is the formation of DMVs. As discussed in the viral replication section, these membrane structures protect viral RNA from PRRs, reducing the activation of innate antiviral signalling. In addition to this, coronaviruses modify their RNA by adding a 5’ cap and 2’-O methylation, making viral transcripts more similar to host mRNA. These modifications reduce recognition by RIG-I and IFIT proteins, limiting the induction of innate immune responses. Beyond these conserved mechanisms, coronaviruses encode several viral proteins that antagonize innate immune signalling. These mechanisms have been characterized in SARS-CoV-2, as illustrated in Figure 9. SARS-CoV-2 proteins and proteases interfere with multiple stages of the innate immune response, including viral sensing, interferon production, and interferon signalling (Minkoff, J.M et al., 2023; Fan, H et al., 2024; Liu, Y et al., 2025; Hatixhe Latifi-Pupovci, 2022; Kasuga et al., 2021).

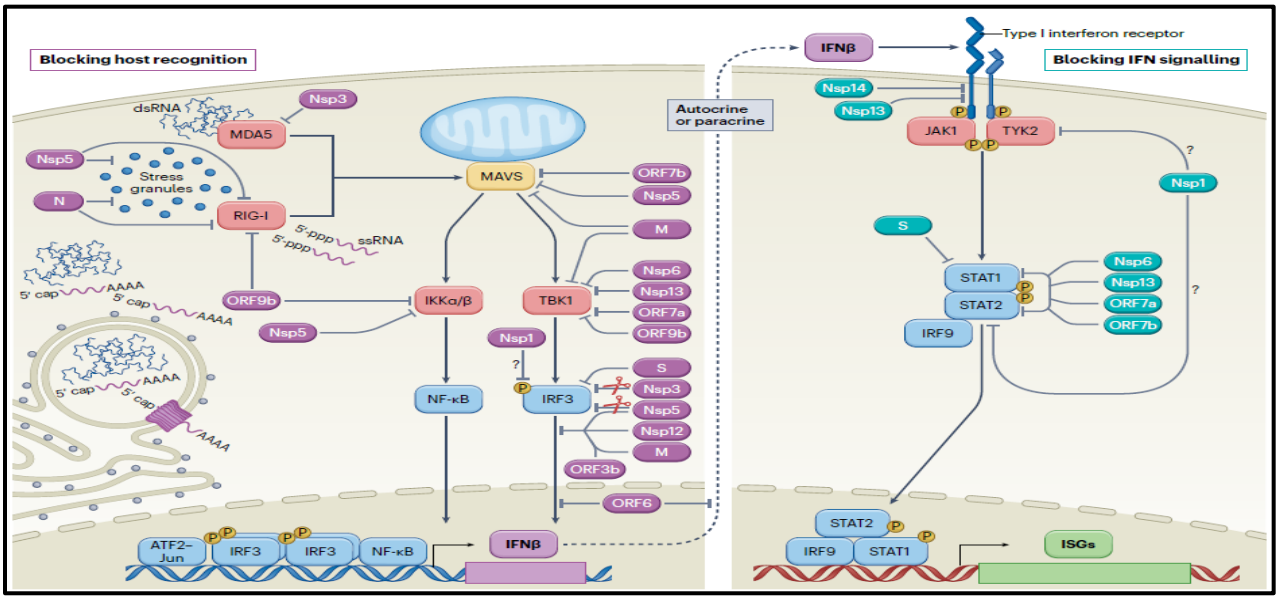

Figure 9. SARS-CoV-2-mediated interference with innate immune signalling. Viral proteins antagonize multiple steps of the host antiviral response, including innate immune sensing, type I interferon production, and interferon signalling. Reproduced from Minkoff and tenOever (2023).

Even though immune evasion mechanisms have been more studied in SARS-CoV-2, the literature indicates that seasonal human coronaviruses employ similar strategies, although these remain less explored.

Apart from these conserved mechanisms, sHCoV-NL63 has evolved strategies to suppress interferon responses. The papain-like protease 2 (PLP2), for example, possesses enzymatic activities capable of reversing ubiquitination and ISGylation, thereby modifying post-translational regulatory mechanisms involved in antiviral signalling, including RIG-I, STING, TBK1, and IRF3. Consequently, PLP2 disrupts the assembly of the STING–MAVS–TBK1/IKKε signalling complex and suppresses IRF3 and NF-κB activation, reducing type I interferon production (Clementz et al., 2010; Sun et al., 2012; Chen et al., 2014; Chiang, Liu & Gack, 2021).

Another mechanism attributed to sHCoV-NL63 PLP2 involves regulation of the p53 pathway. p53 is a cellular tumor suppressor protein that can also act as a sensor of virus-induced cellular

stress and contribute to antiviral responses. Its cellular levels are regulated in part by murine double minute 2 (MDM2), an E3 ubiquitin ligase that adds ubiquitin to p53, targeting it for degradation by the proteasome. sHCoV-NL63 PLP2 interferes with this regulatory mechanism through its deubiquitinating activity. By removing ubiquitin from MDM2, PLP2 increases MDM2 stability, allowing MDM2 to promote the ubiquitination and subsequent proteasomal degradation of p53. Reduced p53 levels also decrease the transcriptional activation of IRF7, a transcription factor involved in the induction of type I interferon. Therefore, through the stabilization of MDM2 and consequent degradation of p53, NL63 PLP2 can weaken the host antiviral response by suppressing p53-mediated antiviral signalling (Yuan et al., 2015; Lei et al., 2018).

In addition, both sHCoV-NL63 and sHCoV-229E encode nsp1, which inhibits host protein synthesis, suppressing the expression of antiviral proteins and contributing to interferon antagonism (Yuan et al., 2015; Enjuanes et al., 2016; de Breyne et al., 2020; Wang et al., 2010).

Overall, sHCoVs share some immune evasion strategies with highly pathogenic coronaviruses, including the protection of viral RNA from host sensors, suppression of interferon induction and signalling.

Regulation of ACE2 Receptor Expression During Viral Infection

Introduction to the ACE2 receptor

Angiotensin-converting enzyme 2 (ACE2) is a type I transmembrane glycoprotein that is part of the renin–angiotensin–aldosterone system (RAAS) and plays a fundamental role in maintaining cardiovascular, renal, and pulmonary homeostasis. While angiotensin-converting enzyme (ACE) generates the vasoconstrictor angiotensin II, ACE2 converts this peptide into angiotensin-(1-7). This ACE2 activity limits excessive RAAS activation, protecting against

inflammation and tissue damage, particularly in the lungs (Imai et al., 2005; Kuba et al., 2005; Silhol F et al., 2020).

ACE2 receptor is normally expressed in many tissues throughout the body, some of which are the respiratory tract, gastrointestinal epithelium, kidneys, and heart. Within the lungs, ACE2 receptor expression is particularly enriched in nasal epithelial cells, ciliated airway epithelial cells, and alveolar type II pneumocytes (Williams, Strachan, Macrae et al., 2021; Lubbe, Cozier, Oosthuizen, Acharya, & Sturrock, 2020). Structurally, ACE2 consists of an extracellular N-terminal peptidase domain containing glycosylation sites and the conserved HEMGH motif required for zinc-dependent catalytic activity. Its C-terminal region contains a transmembrane domain that anchors the protein to the membrane and contributes to its interaction with amino acid transporters (Lubbe, Cozier, Oosthuizen, Acharya, & Sturrock, 2020; Saponaro et al., 2020; Pouremamali, Babaei, Malekshahi et al., 2022).

In addition to its receptor form as described, ACE2 receptor can be cleaved by the metalloprotease ADAM17, releasing a soluble form (sACE2) that retains enzymatic activity. While receptor ACE2 serves as the primary receptor for some coronaviruses, sACE2 can bind viral spike proteins and potentially limit viral entry (Jia et al., 2009; Lambert et al., 2005; Chan et al., 2020).

The discovery that ACE2 serves as the entry receptor for SARS-CoV represented an advance in understanding coronavirus pathogenesis. This finding was later extended to sHCoV-NL63, which was shown to utilize the ACE2 receptor despite belonging to a different coronavirus genus. More recently, SARS-CoV-2 was also found to use the same receptor with considerably higher binding affinity. Structural analyses have revealed that, although these three coronaviruses target overlapping sites within the extracellular region of ACE2, they interact with the receptor through distinct molecular contacts, influencing binding strength (Hofmann et al., 2005; Hoffmann et al., 2020).

Coronavirus infection using the ACE2 receptor

Coronavirus entry begins with the interaction between the spike glycoprotein and the ACE2 receptor, followed by proteolytic activation of spike by host proteases. However, the specific proteases involved in this process differ among coronavirus species, as discussed in the viral entry receptor section. SARS-CoV and SARS-CoV-2 utilize the cell surface serine protease TMPRSS2, allowing membrane fusion and viral entry. In contrast, sHCoV-NL63 relies mostly on cathepsin activity after receptor-mediated endocytosis. These differences influence viral tropism, entry kinetics, and sensitivity to antiviral inhibitors (Milewska et al., 2018; Simmons et al., 2005; Shulla et al., 2011; Hoffmann et al., 2020; Kawase M et al., 2026).

In addition to functioning as a viral entry receptor, ACE2 expression is regulated by physiological and pathological factors. At the transcriptional level, its expression is modulated by inflammatory cytokines, oxidative stress, hypoxia, hormonal signals, and epigenetic mechanisms. Post-transcriptional regulation by microRNAs has also been described. At the protein level, membrane receptor ACE2 undergoes internalization, degradation, and shedding mediated by ADAM17. The amount of ACE2 present at the cell surface reflects the dynamics between receptor synthesis, trafficking, recycling, shedding, and degradation (Lambert et al., 2005; Haga et al., 2008; Gheblawi et al., 2020).

ACE2 exists as two main isoforms: the full-length isoform (flACE2), functioning as both the physiological enzyme of RAAS and the viral receptor, and the interferon-inducible truncated isoform (dACE2), which lacks the spike-binding domains. Although interferon stimulation can increase dACE2 levels, dACE2 is unable to interact with coronavirus spike proteins, and its induction is not expected to increase cellular susceptibility to viral infection (Onabajo et al., 2020; Ng et al., 2020; Xiao et al., 2021).

During SARS-CoV-2 infection, ACE2 surface expression is generally reduced through receptor internalization after spike binding and increased shedding. Although transcriptomic studies have reported variable changes in ACE2 mRNA, presenting both upregulation and downregulation, these changes may not accurately reflect changes in the functional membrane receptor responsible for viral entry. In general, studies suggest that downregulation of ACE2 receptor is directly related to the severity of lung injury (Kuba et al., 2005; Zhuang M-W et al., 2020; Nor Rashid, N et al., 2025).

Less is known about ACE2 receptor regulation during sHCoV-NL63 infection. A kinetic study showed an increase in ACE2 surface expression during the early stages of infection, followed by a marked downregulation as viral replication progressed (Dijkman et al., 2012). In contrast, another paper demonstrated a significant upregulation of the ACE2 receptor over sHCoV-NL63 infection and a modest reduction in ACE2 surface expression over sHCoV-229E infection (Siragam V et al., 2024).

Virus	*Cellular receptor*	*Entry protease*	*ACE2 modulation mRNA*	*ACE2 modulation Receptor Protein*	*Evidence*
SARS-CoV	ACE2	TMPRSS2/Cathepsin L	Downregulation	Strong downregulation through internalization and shedding.	Kuba et al., 2005; Glowacka et al., 2010
SARS-CoV-2	ACE2	TMPRSS2/Cathepsin L	Downregulation/ Upregulation reported by sACE2 production	Strong downregulation through internalization and shedding.	Hoffmann et al., 2020; Nejat et al., 2023; Vieira et al., 2021; Ramos et al., 2021; Yalcin et al., 2021; Zhuang et al., 2020.
sHCoV-NL63	ACE2	Mainly Cathepsins	Initial upregulation followed by downregulation	Early upregulation followed by replication-dependent downregulation	Glowacka et al., 2010; Dijkman et al., 2012
sHCoV-229E	CD13 (APN)	Cathepsins		Indirect downregulation reported	Siragam et al., 2024;

Table 1. Modulation of host entry receptors during infection with human coronaviruses. The table summarizes the impact of SARS-CoV, SARS-CoV-2, sHCoV-NL63, and sHCoV-229E infection on ACE2 expression at the mRNA and protein levels.

Rationale

This project has been built upon findings from previous studies conducted in our laboratory, highlighting both the infection kinetics and cytopathic effects of sHCoVs and their impact on host receptor expression, especially regarding ACE2 receptor upregulation.

It was shown that sHCoV-229E, sHCoV-OC43, and sHCoV-NL63 were capable of exhibiting CPE in their respective cell lines. Notably, only sHCoV-NL63 and sHCoV-OC43 led to an upregulation of the angiotensin-converting enzyme 2 receptor (ACE2). These findings highlighted the differential effects of sHCoVs on receptor modulation and their potential implications for viral entry and co-infection (Figure 1 – Appendices) (Siragam et al., 2023).

Understanding the molecular mechanisms underlying ACE2 receptor upregulation raises important clinical and epidemiological considerations. Increased ACE2 surface expression during sHCoV-NL63 infection could potentially enhance host susceptibility to co-infection or subsequent infection with other ACE2-utilizing viruses, including SARS-CoV-2. This could potentially influence disease severity and increase opportunities for viral interactions, including recombination events that may contribute to the emergence of new variants. These findings provided the rationale for the present study, which aimed to identify whether sHCoV-NL63 viral proteins are involved in ACE2 receptor modulation.

Hypothesis

The project hypothesizes that specific viral proteins from sHCoV-NL63 lead to ACE2 receptor upregulation, which may facilitate co-infections with other viruses that use ACE2 for entry, such as SARS-CoV-2.

Aims

This thesis was structured around two aims:

Aim #1

To identify which viral proteins from NL63 is/are responsible for ACE2 receptor upregulation.

Approach: The isolated viral protein genes will be cloned into expression vectors containing a fluorescent reporter and transfected into cell lines. The analysis to confirm the transfection efficiency and receptor expression will be performed by flow cytometry and western blot techniques.

Aim #2

To validate ACE2 upregulation mechanisms in a more relevant context, the same techniques will be performed in primary human cells.

Approach: Primary human cells will be transfected and analyzed using flow cytometry and western blot techniques

Methods

Vector Design

Polycistronic pcDNA3.1 vectors containing the isolated viral protein sequences from sHCoV-NL63 and sHCoV-229E were designed based on sequences obtained from the National Center for Biotechnology Information (NCBI) database using SnapGene software and subsequently synthesized by GenScript for transfection experiments (Liu, Liang, & Fung, 2021; National Center for Biotechnology Information [NCBI], n.d.; ViralZone, n.d.).

For sHCoV-NL63, the genes of interest included Spike protein (S), Envelope protein (E), Membrane protein (M), Nucleocapsid protein (N), Protein 3 (P3), and Open Reading Frame 1ab (ORF1ab – both ORF1a and ORF1b regions were cloned) (Figure 10).

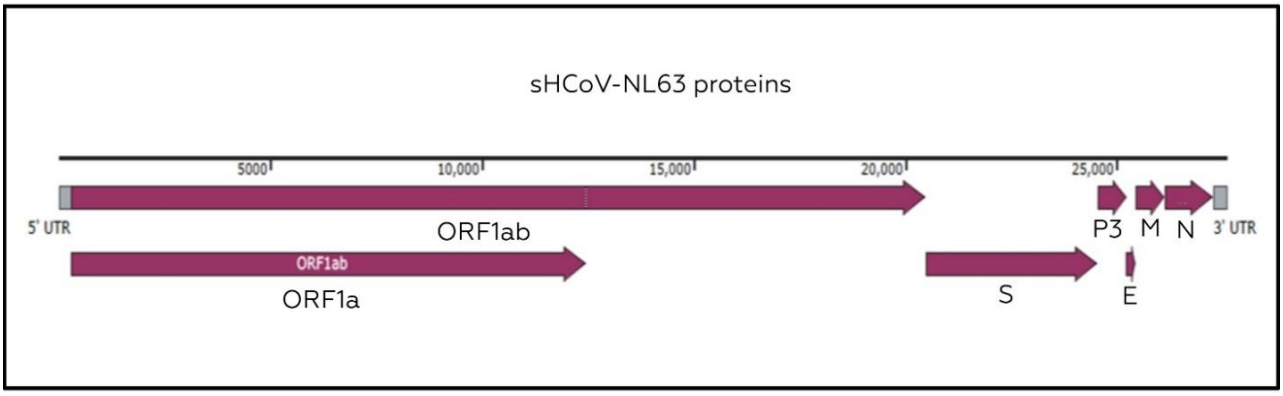

Figure 10. Analysis of Proteins of sHCoV-NL63 for isolation. (Adapted image from Snap Gene; NCBI Reference Sequence NC_005831.2)

For sHCoV-229E, which was used as a physiological control, the genes of interest included the Spike protein (S), Envelope protein (E), Membrane protein (M), Nucleocapsid protein (N), Protein 4A (4A), and Protein 4B (4B) (Figure 11).

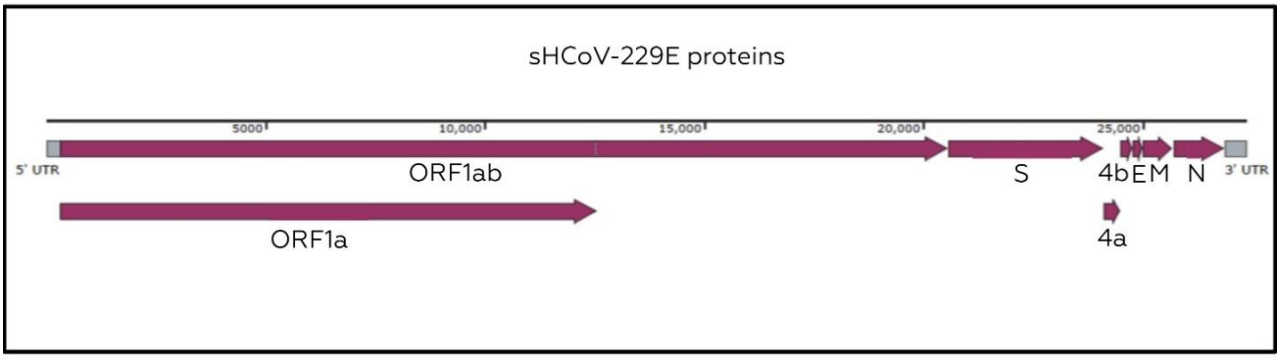

Figure 11. Analysis of Proteins of sHCoV-229E for isolation. (Adapted image from Snap Gene; NCBI Reference Sequence NC_002645)

The vectors were designed with CMV as a promoter, FLAG-DYKDDDDK as a tag in frame with the gene of interest to enable protein detection, an Internal Ribosome Entry Site (IRES) to allow cap-independent translation of the downstream GFP from the same bicistronic transcript, GFP as a reporter gene to confirm transfection efficiency, and antibiotic resistance genes: Neomycin/Kanamycin for cell selection and Ampicillin for bacterial selection (Figure 12).

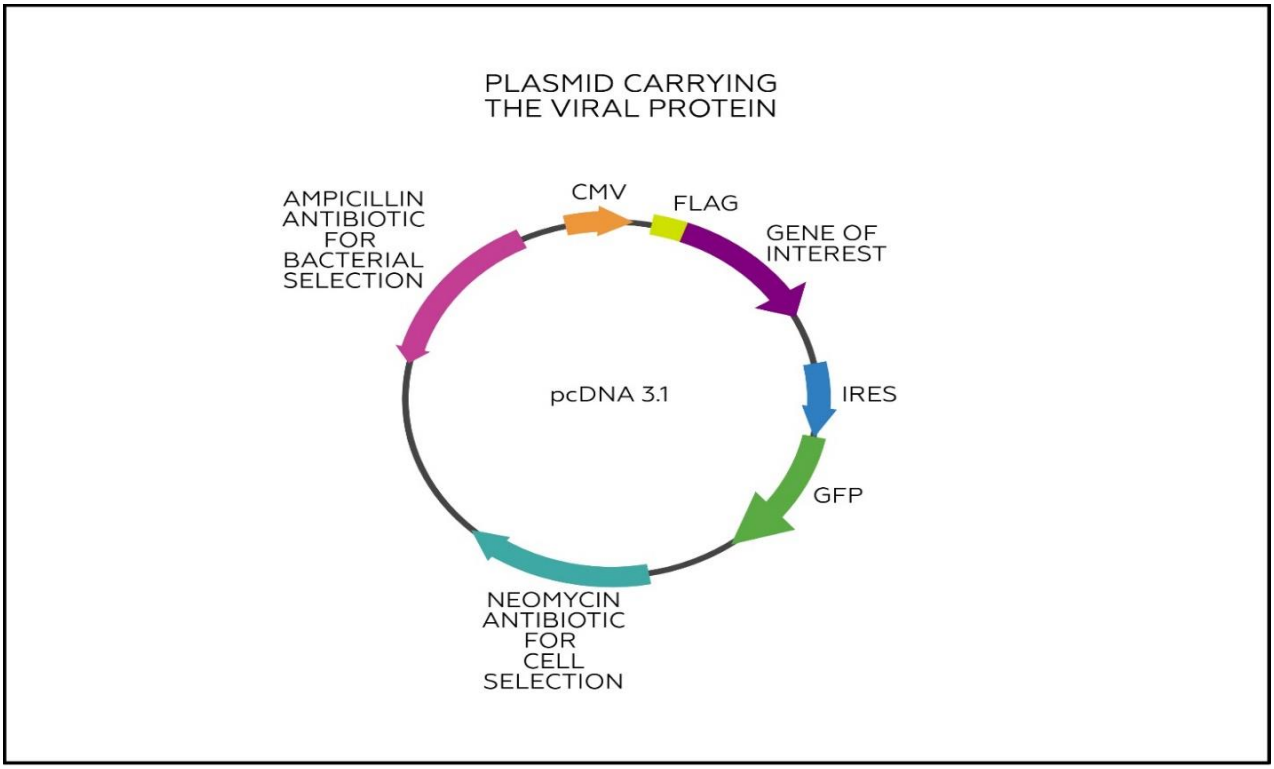

Figure 12. General organization of the polycistronic expression vectors. Each construct contains the CMV promoter, an N-terminal FLAG epitope in-frame to the viral gene, an Internal Ribosome Entry Site (IRES), enhanced Green Fluorescent Protein (eGFP), a Neomycin resistance cassette for cell selection, and Ampicillin resistance for bacterial selection.

In addition, a double reporter control vector was designed following the same specifications, with the gene of interest replaced by mCherry. Later, monocistronic pcDNA3.1 vectors expressing either FLAG control (FLAG-A2 or FLAG-APOBEC2 and FLAG-A3G or FLAG-APOBEC3G) or GFP control (GFP-A2 or GFP-APOBEC2 and GFP-A3G or GFP-APOBEC3G) obtained from our laboratory control stock, were included as technical positive controls during flow cytometry optimization (Figure 13). FLAG-A2 was used to establish the positive population for FLAG detection in the Alexa Fluor 647 channel, whereas GFP-A2 was used to define the GFP-positive population in the FITC channel. These constructs therefore provided independent controls for each fluorescent marker and supported the establishment of consistent gating parameters before the analysis of the viral protein

constructs. Their inclusion was intended specifically for optimization of the flow cytometry gating strategy and not as biological controls for changes in ACE2 expression.

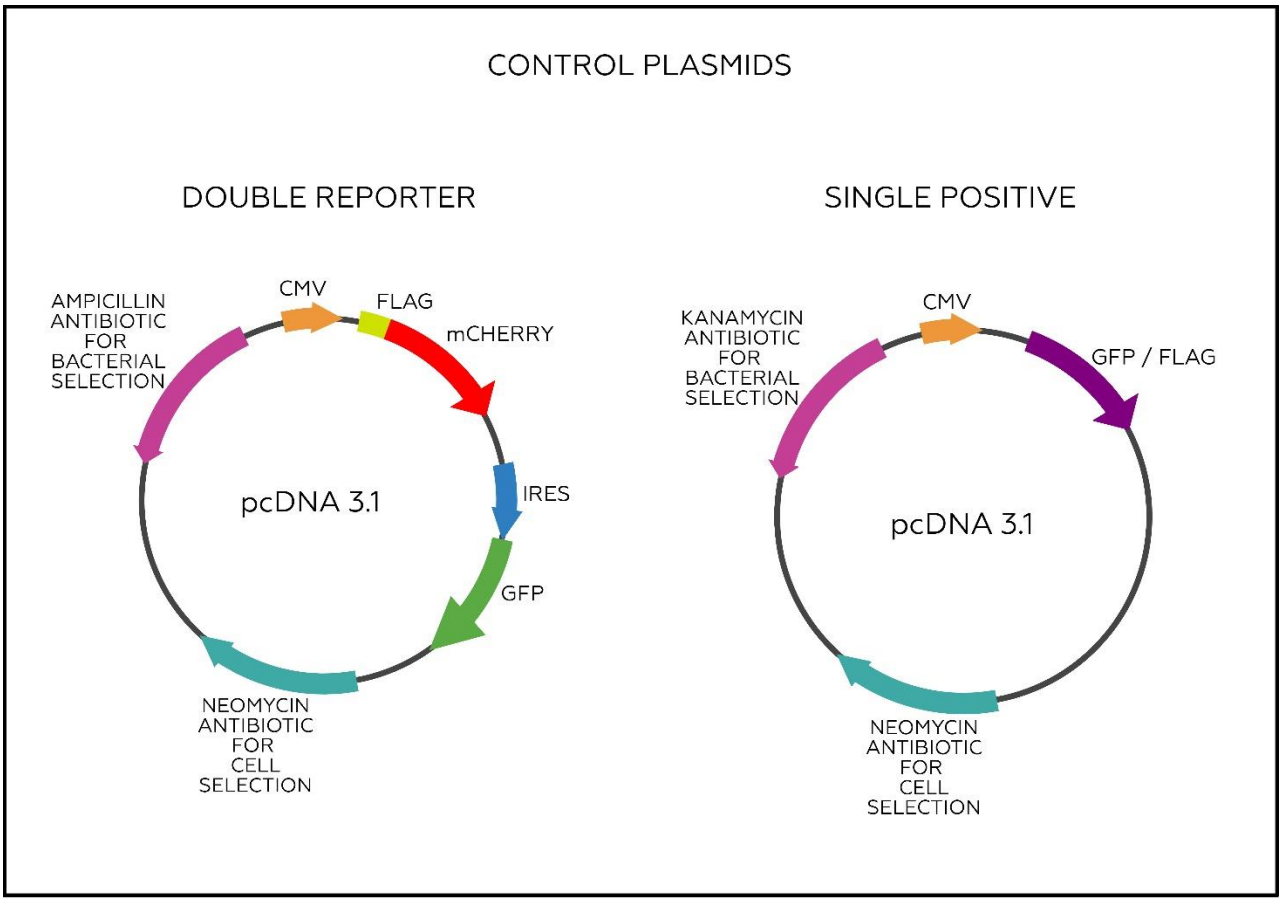

Figure 13. Control plasmids. Schematic representation of the control plasmids. Positive controls included a dual fluorescent FLAG in frame with mCherry and GFP vector and monocistronic FLAG-A2 and GFP-A2 expression vectors used for optimization of flow cytometry gating, antibody staining and western blot detection.

Due to lack of detectable Spike protein expression, monocistronic pcDNA3.1 vectors were also designed to express the Spike protein, with the FLAG tag switched from the N-terminus to the C-terminus, to address potential protein stability issues (Figure 14).

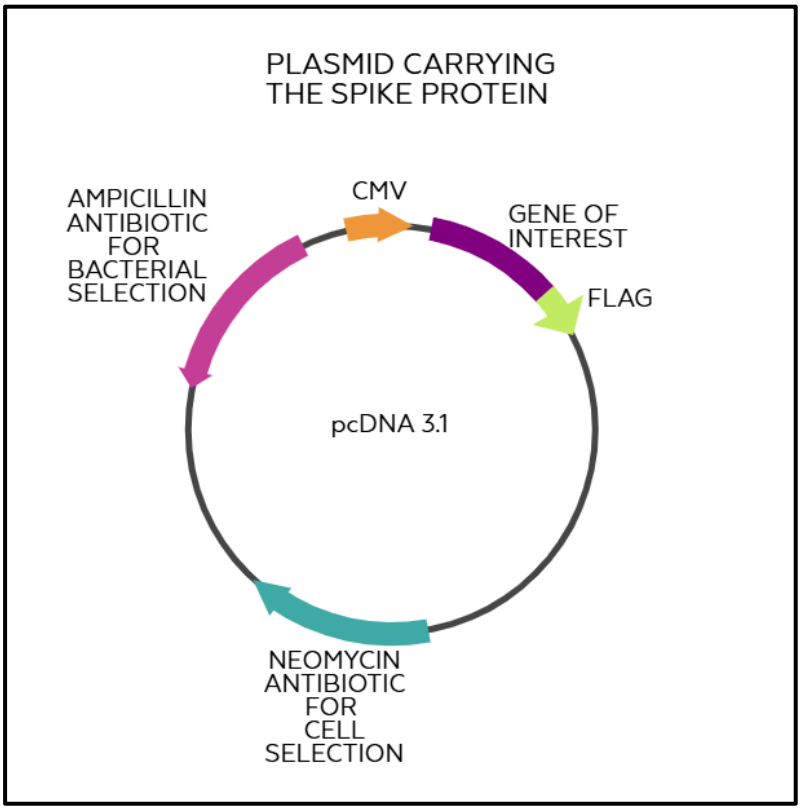

Figure 14. Monocistronic Spike protein construct. Design of the monocistronic pcDNA3.1 construct expressing the sHCoV-NL63 Spike protein. To improve protein stability and expression, the FLAG epitope was repositioned from the N-terminus to the C-terminus of the Spike coding sequence.

Centrifugation

For microcentrifuges tubes ranging from 1.5 to 2mL, centrifugation was performed using a Thermo Fisher Scientific Legend Micro 21 microcentrifuge equipped with a 24 × 1.5/2 mL rotor (#75003424). For flow cytometry tubes, 15 mL tubes, and 50 mL tubes, centrifugation was performed using a Thermo Fisher Scientific Legend XTR centrifuge equipped with a rotor with a maximum speed of 3,500 rpm (#75003667).

Plasmid Propagation

After receiving the designed plasmids from GeneScript, the lyophilized plasmids were resuspended in RNase-free sterile water at a concentration of 100 ng/µL. The plasmids were then propagated, and screening was performed to confirm the extraction of the correct plasmid with the expected sequence.

Competent Escherichia coli DH5α cells were used for transformation with the plasmid of interest using a heat-shock protocol. Competent cells were thawed on ice for approximately 7 - 10 min. For each transformation, 1 - 5 µL of plasmid at 100 ng/µL was added to a sterile 1.7 mL microcentrifuge tube, followed by 80 µL of competent cells. The DNA and cells were gently mixed by pipetting and incubated on ice for 30 min. The cell–plasmid mixture was subsequently subjected to heat shock at 42°C for 90 seconds in a water bath incubator. Immediately following heat shock, the cells were placed on ice without agitation and incubated for an additional 2 min.

Following ice incubation, 800 µL of 2xYT medium with 1 M glucose was added to each transformation reaction, and the suspension was gently mixed by inversion. The cells were recovered at 33°C with shaking at 210 rpm for 1 h and 30 minutes. During the recovery period, LB agar plates containing the appropriate antibiotic (Ampicillin) at a final concentration of 150 µg/mL were pre-incubated at 33°C. After recovery, the cultures were gently mixed, and 200 µL of each transformation culture was spread onto the antibiotic-containing LB agar plates using a sterile L-shaped cell spreader. For plasmids exhibiting low transformation efficiency, such as NL63-ORF1a and NL63-ORF1b, the entire recovery culture was centrifuged at 3,000 rpm for 3 min, the resulting pellet was resuspended in 200 µL of the supernatant, and the concentrated suspension was plated. Plates were incubated in an inverted position overnight (16–18 h) at 33°C.

Following incubation, bacterial colonies were examined for the expected colony morphology, including size and appearance (large, white and rounded colonies with no satellite colonies around

them). Individual colonies were collected and used for plasmid extraction using QIAprep Spin Miniprep Kit (#27106) following all the steps described in the manufacturer's protocol.

To maintain quality and clone specificity, glycerol stocks were prepared. Following overnight growth at 33°C, as mentioned above, 500 µL of the bacterial culture was transferred to a sterile 1.7 mL tube and mixed with 500 µL of 50% sterile glycerol, resulting in a final glycerol concentration of 25%. The suspension was mixed by inversion, appropriately labelled with the bacterial strain, plasmid, and date, and stored at −80°C.

Plasmid Restriction Enzymes Digestion

Restriction enzymes recognize specific sequences and cleave the phosphodiester backbone at defined sites, generating fragments of predictable sizes that can be used to confirm the expected plasmid construct.

Restriction enzyme digestion was performed for plasmid screening to confirm the expected plasmid size. We planned to use restriction enzymes corresponding to the beginning and end of the gene of interest. However, we did not have suitable single-cutter candidates in this region. As the restriction enzymes were used only for screening, we decided to proceed with other available enzymes and send the plasmids for sequencing later. The plasmids were digested using restriction endonucleases from New England Biolabs (NEB), including MluI-HF (#R3198S), HindIII-HF (#R3104S), XmaI (#R0180S), SacI-HF (#R3156S), AgeI-HF (#R3552S), and EcoRV-HF (#R3195S).

As illustrated in Figures 3 and 4 in the Appendices, MluI-HF and HindIII-HF were used for the digestion of the majority of the sHCoV-NL63 and sHCoV-229E structural and accessory protein plasmids. MluI-HF was used in combination with XmaI for the NL63-ORF1b plasmid and 229E Nucleocapsid, whereas SacI-HF and XmaI were used for the 229E-Envelope construct. The NL63-ORF1a plasmid was digested using AgeI-HF and EcoRV-HF. The expected fragment sizes described in the figure were calculated based on the restriction sites and total plasmid size.

Restriction digestion reactions were prepared on ice in a final volume of 25 µL, containing 500 ng of plasmid, 2.5 µL of 10× rCutSmart, 0.5 µL of each restriction enzyme, and nuclease-free water to a final volume of 25 µL. For double digestions, both restriction enzymes were included in the same reaction, with enzyme compatibility always checked using the restriction enzyme tool on the NEB website. Enzymes were added last, and the reactions were gently mixed by tapping the tube. The reactions were incubated at 37°C for 1 h using an Eppendorf ThermoMixer F.

Following digestion, samples were mixed with DNA loading dye (NEB #B7024S) and analyzed by 1x agarose gel electrophoresis alongside a DNA molecular weight ladder (DM3100 – SMOBIO). The resulting bands were compared with the predicted fragment sizes to confirm the expected plasmid architecture.

Sequencing

Furthermore, the same plasmids previously described were sent for sequencing, which was performed by Plasmidsaurus, confirming that the obtained sequences matched the designed plasmid maps provided by GenScript. A summary of the alignment report, generated using the SnapGene application, is provided in Figure 5 in the Appendices. Because of the size of the sequences, the complete alignments were not included in this thesis. However, the electrophoresis gel provided with the sequencing results was also included in Figure 6 in the Appendices.

Cell culture

Two cell lines were selected for the study: LLC-MK2 (rhesus monkey kidney cells; CCL-7, ATCC) and HEK293T+ACE2 (human embryonic kidney epithelial cells stably expressing angiotensin-converting enzyme 2; BEI Resources, NR-52511). HEK293T (human embryonic kidney epithelial cells; CRL-3216, ATCC) cells were additionally used during the initial optimization of transfection conditions and flow cytometry gating.

LLC-MK2, HEK293T and HEK293T+ACE2 cells were maintained in DMEM medium (Wisent Bioproducts #319-005-CL) supplemented with 10% Fetal Bovine Serum or FBS (Avantor #97068-085) and 1% Penicillin/ Streptomycin or P/S (Cytiva #SV30010). All cell lines were cultured and maintained at 37°C in a humidified incubator with 5% CO_2. To ensure the absence of mycoplasma contamination and maintain experimental quality, all cell lines were routinely tested using the LookOut Mycoplasma PCR Detection Kit (# MP0035).

Transfection

The chemical transfection conditions for HEK293T+ACE2 (293T+ACE2) and LLC-MK2 cells were optimized using plasmids encoding viral proteins and control plasmids (peGFP-C3, peGFP-A2, peGFP-A3G, peFLAG-A2, peFLAG-A3G and Double reporter). Transfection efficiency was evaluated by measuring GFP expression using flow cytometry and confirmed by fluorescence microscopy. Two commercially available transfection reagents, jetPRIME Transfection Reagent (Polyplus, CAT#101000027) and Lipofectamine 2000 Transfection Reagent (Thermo Fisher Scientific, CAT#11668027), were used during the optimization process (Chong, Yeap, & Ho, 2021; Polyplus, n.d.).

For HEK293T+ACE2 cells, jetPRIME provided efficient transfection and was selected for all subsequent experiments. Cells were seeded at 3×10^5 cells per well in 6-well plates one day before transfection in complete medium (DMEM supplemented with 10% FBS and 1% penicillin-streptomycin). Transfection was performed using 3 µL of jetPRIME reagent per 1 µg of plasmid DNA diluted in 200 µL of jetPRIME buffer. The transfection mixture was added directly to the cells and incubated for 6 hours at 37°C in a humidified incubator containing 5% CO_2. After the incubation, the transfection medium was replaced with fresh complete medium. Cells were further incubated for 48 hours before being analyzed by fluorescence microscopy, harvested for flow cytometry, and collected for western blot analysis.

For LLC-MK2 cells, several transfection trials were initially performed using jetPRIME. However, due to the low transfection efficiency observed in this monkey kidney cell line, the protocol was optimized using Lipofectamine 2000, which resulted in improved expression efficiency. Cells were seeded at 1.7×10^5 cells per well in 6-well plates one day before transfection in complete medium (DMEM supplemented with 10% FBS, 1% penicillin-streptomycin, and 1% glutamine). Thirty minutes before transfection, the culture medium was replaced with MEM (GIBCO #11095-080) containing 3% FBS. Transfection was performed using 7 µL of Lipofectamine 2000 and 1.2 µg of plasmid DNA diluted in 200 µL of serum-free and antibiotic-free MEM. The transfection mixture was incubated with the cells for 4 hours at 37°C and 5% CO_2, after which the medium was replaced with fresh complete medium. Cells were incubated for an additional 48 hours before analysis by fluorescence microscopy and flow cytometry. A portion of the harvested cells were also collected for subsequent western blot analysis.

Detection by Fluorescence Microscopy

The fluorescence microscopy acquisition was primarily performed using a Zeiss confocal inverted microscope at 48 h post-transfection to detect the expression of the reporter gene, green fluorescent protein (GFP). Some images were also captured using the ZOE microscope available at the university for common use.

Using the designed polycistronic vector system, it was expected that all cells exhibiting GFP fluorescence would also express the gene of interest, allowing them to be considered double-positive cells. The images were acquired using a 10x objective and a GFP filter. GFP fluorescence was detected by excitation with blue light, which is absorbed by the fluorophore and subsequently emitted as green fluorescence. The camera exposure settings were manually optimized and maintained constant across all experiments to allow accurate comparison between conditions.

CPE was assessed by examining the transfected cells under brightfield and comparing them with MOCK untransfected cells exposed to the transfection reagent. Positive CPE was considered to be present when morphological changes, cell aggregation, cytoplasmic vacuoles, and/or cell death were observed (Figures 7, 9, and 11 in the Appendices). CPE was not scored (+/++/+++/++++), instead, this analysis was used as a qualitative assessment based on the presence or absence of CPE.

Detection by Flow Cytometry

Flow cytometry was used to quantitatively measure fluorescence signals in individual cells. It was applied to evaluate exogenous GFP expression, cell surface ACE2 receptor expression, and intracellular FLAG-tagged protein expression.

Surface ACE2 protein expression was assessed by staining with a primary polyclonal goat IgG anti-human ACE2 antibody, followed by a PE-conjugated donkey anti-goat IgG secondary antibody.

FLAG expression, corresponding to the gene of interest in the designed polycistronic vector, was evaluated by intracellular staining using a rat IgG2a monoclonal anti-FLAG antibody conjugated to Alexa Fluor 647.

Antibody titration was also performed for both the Alexa Fluor 647-conjugated anti-FLAG antibody, which demonstrated the best efficiency at a 1:2000 dilution (Figure 20), and the PE-conjugated secondary antibody for ACE2 detection, which showed better efficiency at a 1:250 dilution (Figure 21). The primary ACE2 antibody had already been optimized in the laboratory and was used at a 3:100 dilution.

Untransfected cells (MOCK) were used to establish baseline FSC, SSC, and fluorescence detector voltages. Isotype controls were included for each antibody staining condition to assess nonspecific antibody binding and background fluorescence. A plasmid expressing both GFP and FLAG-tagged

mCherry was used as a positive control for dual fluorescence detection, while individual GFP and FLAG controls were included to further optimize the gating strategy.

For cell preparation, HEK293T+ACE2 cells were harvested using 1× PBS supplemented with 5 mM EDTA, whereas LLC-MK2 cells were detached using StemPro™ Accutase™ Cell Dissociation Reagent (#A1110501) and placed in a flow tube. Cells were centrifuged at 300 × g for 5 minutes and washed with 1× PBS containing 0.2% BSA. For surface ACE2 staining, cells were incubated with the primary anti-hACE2 antibody for 1 hour at 4°C, followed by two washes with 1x PBS containing 0.2% BSA. Cells were then incubated with the PE-conjugated secondary antibody for 40 minutes at 4°C and washed twice with 1x PBS containing 0.2% BSA. Subsequently, cells were fixed and permeabilized using the BD Cytofix/Cytoperm™ Fixation/Permeabilization Kit (#554714) for intracellular FLAG staining. Following permeabilization, cells were stained with the Alexa Fluor 647-conjugated anti-FLAG antibody according to the BD kit protocol and resuspended in 1× PBS containing 0.2% BSA for flow cytometry analysis.

Detection by Western Blot

Western blotting was used for the detection and confirmation of specific proteins, complementing the flow cytometry findings by evaluating protein production, relative abundance, and molecular weight.

For protein extraction, HEK293T+ACE2 cells were lysed using Triton lysis buffer (1.25% Triton X-100, 0.1% NP-40, 50 mM Tris-HCl, pH 7.5, and 150 mM NaCl) supplemented with 2× protease inhibitor cocktail (Thermo Scientific #87786) and incubated on ice for 20 minutes, with the tubes mixed every 5 minutes. LLC-MK2 cells were lysed using NP-40 lysis buffer (1% NP-40, 50 mM Tris-HCl, pH 7.4, 150 mM NaCl, and 5 mM EDTA) supplemented with 2× protease inhibitor cocktail and incubated for 30 minutes under constant agitation at 4°C. Following lysis, samples were centrifuged at 12,000 rpm for 20 minutes, and the supernatants were transferred to 1.7 mL tubes.

The protein lysates were mixed with SDS-free loading buffer (62.5 mM Tris-HCl, pH 6.8, 25% glycerol, and 1% bromophenol blue) to minimize SDS-related aggregation, and the samples were not heat-denatured to prevent thermal aggregation of the target proteins.

Proteins were separated by SDS-PAGE using 12% polyacrylamide gels, except for Spike protein detection, for which 7.5% gels were used to improve resolution of the higher molecular weight protein. The amount of sample loaded depended on the comb size; for all the trials, the maximum volume per well was used. Protein concentration would normally be measured using a BSA protein quantification assay to load the same amount of protein per well. However, because of the aggregation presented by most of the viral proteins and limited expression, the maximum possible sample volume was loaded to increase the likelihood of detecting the proteins. The running and transfer buffers were prepared according to the general Bio-Rad protocol. The running buffer contained 25 mM Tris, 190 mM glycine, and 0.1% SDS, while the transfer buffer contained 25 mM Tris, 190 mM glycine, and 20% methanol, which was added before transfer. Electrophoresis was performed for 5 minutes at 50 V, followed by 30 minutes at 100 V and 40 minutes at 120 V.

Before transferring, gels were equilibrated in transfer buffer containing 20% methanol for 10 minutes. Proteins were then transferred onto methanol-activated PVDF membranes using a sandwich transfer system (negative polarity side, sponge, 3 filter papers, gel, activated PVDF membrane, 3 filter papers, sponge, positive polarity side). The PVDF membrane was activated by submerging it in pure methanol for 1 minute and then washing it once with transfer buffer before incorporation into the transfer sandwich. After transfer, the membranes were blocked in 1× TBST (20 mM Tris, pH 7.5, 150 mM NaCl, and 0.1% Tween 20) supplemented with 5% BSA for 1 hour at room temperature and subsequently incubated with the specific antibody diluted in 1× TBST supplemented with 3% BSA for 1 hour at room temperature or overnight at 4°C. Membranes were washed with 1× TBST and visualized using a Bio-Rad ChemiDoc imaging system with an enhanced chemiluminescence (ECL) detection substrate.

β-Tubulin was used as the loading control and detected using a rabbit polyclonal HRP-conjugated anti-β-tubulin antibody (#ab21058). FLAG was detected primarily using a monoclonal mouse anti-FLAG M2 HRP-conjugated antibody (#A8592) but was also tested using a monoclonal mouse anti-FLAG (DYKDDDDK) HRP-conjugated antibody, with no differences observed between the two antibody detections. GFP was detected using a polyclonal goat HRP-conjugated anti-GFP antibody (#ab6663). hACE2 was detected using a primary polyclonal goat anti-human ACE2 antibody followed by an HRP-conjugated rat anti-goat IgG secondary antibody (#A9037, Sigma).

Representative images illustrating the troubleshooting are shown in Figure 2 in the Appendices.

Detection by Dot Blot

Protein dot blot is an immunoblotting assay used for the qualitative detection and semi-quantitative analysis of target proteins. Similar to western blotting, this technique is based on the specific interaction between a target protein and its corresponding antibody. However, unlike western blotting, dot blotting does not provide information regarding protein molecular weight, as proteins are directly immobilized onto the membrane without prior separation by electrophoresis.

For the assay, a 10 µL aliquot of sample was applied directly to a nitrocellulose membrane and allowed to dry before blocking with 1× TBST containing 5% BSA for 1 hour at room temperature. Membranes were subsequently incubated with specific primary antibodies diluted in 1× TBST containing 3% BSA for 1 hour at room temperature. Following antibody incubation, membranes were washed four times with TBST (0.1% Tween-20) and visualized using a Bio-Rad ChemiDoc imaging system with an enhanced chemiluminescence (ECL) substrate.

sHCoV-NL63 Infection Assay

The cells were seeded one day before infection at 2.5×10^5 cells per well in 6-well plates using complete medium (DMEM supplemented with 10% FBS, 1% P/S, and 1% glutamine). On the day of infection, the medium was replaced with adsorption medium (DMEM supplemented with 1% P/S

and 1% glutamine), and the MOIs used were 0.007, 0.01, and 0.1. After 1 hour of incubation for virus adsorption at 35°C, the medium was replaced with DMEM supplemented with 3% FBS, 1% P/S, and 1% glutamine, and the cells were maintained at 35°C in 5% CO_2. Samples were collected on days 1, 2, 3, and 4 and analyzed by flow cytometry and western blotting.

The same collection procedure described above was used for this experiment, with the addition of a fixation step for flow cytometry. After cell staining, the cells were fixed with 4% PFA for 30 min and resuspended in 1× PBS containing 0.2% BSA.

Statistical Analysis

Statistical analyses were performed using GraphPad Prism. The results were considered statistically significant at $p < 0.05$.

Statistical significance of ACE2 modulation was evaluated using the geometric mean fluorescence intensity (gMFI) obtained from flow cytometry data. The geometric mean fluorescence was assessed to analyze the intensity of ACE2 in ACE2-expressing cells. One-way analysis of variance (ANOVA) is a common statistical analysis used to evaluate the overall differences among groups, calculating the p-value based on the value between group variation with within group variation.

To identify specific differences between groups, Tukey's multiple comparisons test was performed; the p-value was calculated by specifically comparing the protein of interest against the mock group and the physiological control.

Results

Characterization of ACE2 Receptor Modulation During sHCoV-NL63 Infection in Permissive LLC-MK2 cells

Previous preliminary observations from our laboratory suggested that sHCoV-NL63 infection could influence ACE2 receptor expression in LLC-MK2 cells. These preliminary observations provided the basis for the central question investigated in this study: whether the modulation of ACE2 observed during infection could be reproduced by the isolated expression of individual sHCoV-NL63 proteins. However, before evaluating ACE2 modulation using transient expression systems, it was important to further characterize the infection-associated phenotype itself. Therefore, infection kinetics experiments were performed in LLC-MK2 cells to determine how ACE2 surface expression changed throughout the progression of sHCoV-NL63 infection.

LLC-MK2 cells were infected with sHCoV-NL63 at different multiplicities of infection (MOI 0.007, 0.01, and 0.1), and ACE2 surface receptor expression was evaluated at multiple time points post-infection (1–4 days post-infection, DPI) by flow cytometry and western blot.

The analysis included cell surface staining for ACE2 detection using an isotype control to define background fluorescence and assess changes in ACE2 receptor expression in cell populations following infection. In parallel, samples were collected for western blot analysis to further evaluate ACE2 protein expression and determine whether changes observed at the cellular surface corresponded to alterations in total protein levels.

As shown in Figure 15, ACE2 surface expression was detected in both mock and sHCoV-NL63 infected LLC-MK2 cells.

In mock cells, the percentage of receptor ACE2-positive cells exhibited modest fluctuations over time (58.0–67.2%), a phenomenon that has also been reported in the literature and may reflect

variations associated with cell confluence or culture conditions. Therefore, each infected condition was compared with its corresponding mock control collected at the same time point.

Comparison between infected and mock cultures revealed a possible time- and/or MOI-dependent modulation of ACE2 surface expression following sHCoV-NL63 infection. At an MOI of 0.007, the proportion of ACE2 receptor expression increased by 3% at 1 DPI compared with the corresponding mock control (63.7% - 60.7%), followed by a progressive reduction at subsequent time points. Similarly, infection at an MOI of 0.01 resulted in a 5% increase in ACE2 receptor expression at 1 DPI (65.7% vs 60.7%) and a smaller increase of 2.9% at 2 DPI (60.9% vs 58.0%), followed by a gradual decline at later time points. The highest inoculum, at an MOI of 0.1, also exhibited a slight increase of 1.2% in ACE2 receptor expression at 1 DPI (61.9% vs 60.7%), after which ACE2 expression progressively decreased at 2, 3, and 4 DPI.

To determine whether changes in ACE2 surface expression reflected in total ACE2 protein levels, western blot analysis was performed (Figure 15). Panel B was used to generate Panel C, which shows the fold change in ACE2 protein expression relative to mock controls. To obtain these results, the total band intensity of ACE2 was divided by the total band intensity of beta-tubulin, thereby normalizing ACE2 protein levels for analysis.

Comparison of the results obtained from panels A and C revealed distinct patterns of ACE2 expression. While cell-surface ACE2 progressively decreased during infection, total cellular ACE2 protein remained stable or increased at later time points. A complete characterization of ACE2 regulation including mRNA quantification and soluble ACE2 detection was not performed in this thesis. However, the difference between surface and total ACE2 could potentially involve changes in receptor internalization, trafficking, shedding or degradation. These processes could reduce the amount of ACE2 present at the cell surface without necessarily resulting in a similar reduction in total cellular ACE2, particularly if accompanied by the synthesis of additional ACE2 protein. In this context, the contribution of different ACE2 isoforms, including the interferon-inducible truncated

isoform dACE2, could also potentially contribute to the stable or increased detection of total ACE2 at later time points. However, these mechanisms and the relative contribution of different ACE2 isoforms were not experimentally distinguished in this study.

At 48 hours post-infection, as illustrated in panel C, ACE2 protein levels increased in all infected samples compared with their corresponding mock controls. This effect became more evident at later time points and with increasing viral inoculum.

Overall, these findings suggest that sHCoV-NL63 infection induces an increase in the ACE2 receptor during the early stage of infection, followed by a progressive decline in ACE2 surface expression as infection proceeds.

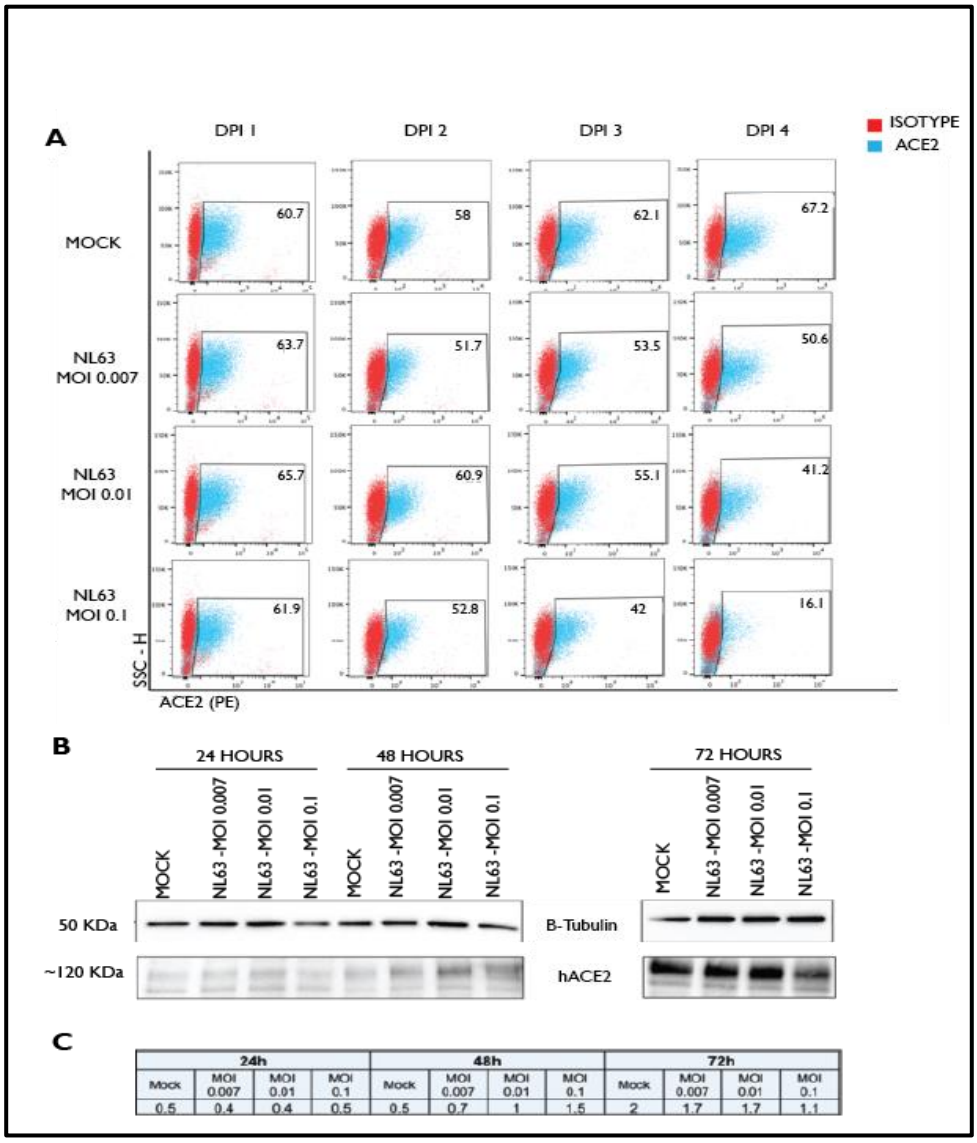

Figure 15. sHCoV-NL63 infection in permissive LLC-MK2 cells at different time points. LLC-MK2 cells were infected with sHCoV-NL63 at multiplicities of infection (MOI) of 0.007, 0.01, or 0.1 and analyzed at 1, 2, 3, and 4 days post-infection (DPI). (A) Representative flow cytometry dot plots showing ACE2 surface expression (PE) in mock and sHCoV-NL63-infected cells. The isotype control (red) was used to establish background fluorescence, while ACE2-positive cells are shown in blue. (B) Representative western blot analysis of total ACE2 protein expression in mock and sHCoV-NL63 infected LLC-MK2 cells collected at the indicated time points. β-Tubulin was used as the loading control. (C) ACE2 band intensity was normalized to β-tubulin, and values are shown as fold change relative to the corresponding mock control. Data are from a single experiment performed by the author in collaboration with Research Associate Negar Joharinia.

Another infection kinetics experiment was performed to further characterize receptor modulation throughout viral infection progression. This experiment was performed following the protocol described by Dijkman et al. (2012). In their study, the authors reported a pattern similar to that observed in our experiments: an early upregulation of ACE2 surface expression followed by a marked downregulation as the infection progressed. Figure 16 presents the results obtained from this kinetics experiment, while Figure 17 compares our findings with those reported by Dijkman et al., demonstrating a similar temporal pattern of ACE2 modulation.

The infection assay presented in Figure 16 was successfully performed. The cells started presenting CPE at day 2 post-infection (DPI) and showed considerable cell death at DPI 5. The non-infected cells, referred to as MOCK, presented variation in ACE2 expression over the days (20.3%-25%), a behavior that has also been reported in the literature. In this experiment, we observed an increase in ACE2 surface expression at days 2 and 3 post-infection, achieving a peak of 8.5% upregulation and then a significant decrease at DPI 4 and 5.

The correlation between ACE2 reduction and increased CPE suggests that receptor modulation occurs alongside viral infection progression. Importantly, the early increase in ACE2 surface expression was observed before substantial CPE or cell loss became evident, making it less likely that this initial modulation resulted from changes in cell viability or population loss. The mechanism responsible for this early increase, however, remains unresolved. The results obtained in this study did not identify any of the successfully evaluated individual viral proteins as sufficient to induce the ACE2 receptor modulation. Nevertheless, several components of the infection process were not captured by the transient-expression approach, including the activity of non-structural proteins, protease-mediated processing, interactions among simultaneously expressed viral proteins, viral replication-associated processes, and host antiviral responses. Therefore, the absence of modulation following isolated protein expression does not exclude the possibility that one or more of these infection-associated processes contribute to the early modulation of ACE2.

In contrast, interpretation of the later decrease in surface ACE2 is more complex because it coincided temporally with increasing CPE and cell loss. However, preliminary data from our laboratory suggest that the observed reduction in ACE2 is not attributable to the loss of infected cells. In this preliminary experiment, sHCoV-NL63-infected cells were stained for the viral N protein together with a live/dead viability marker. ACE2 surface expression was analyzed using both N protein-positive live cells and N protein-positive single cells as gating strategies. In both analyses, infected cells showed markedly reduced ACE2 surface expression compared with mock non-infected cells, supporting the possibility that the decrease reflects an active reduction of surface ACE2 receptor rather than simply the loss of infected cells (Figure 14 – in the Appendices). Processes such as altered receptor trafficking, internalization, shedding, or degradation could potentially contribute to the decrease in surface ACE2. However, these mechanisms were not directly investigated in the present study.

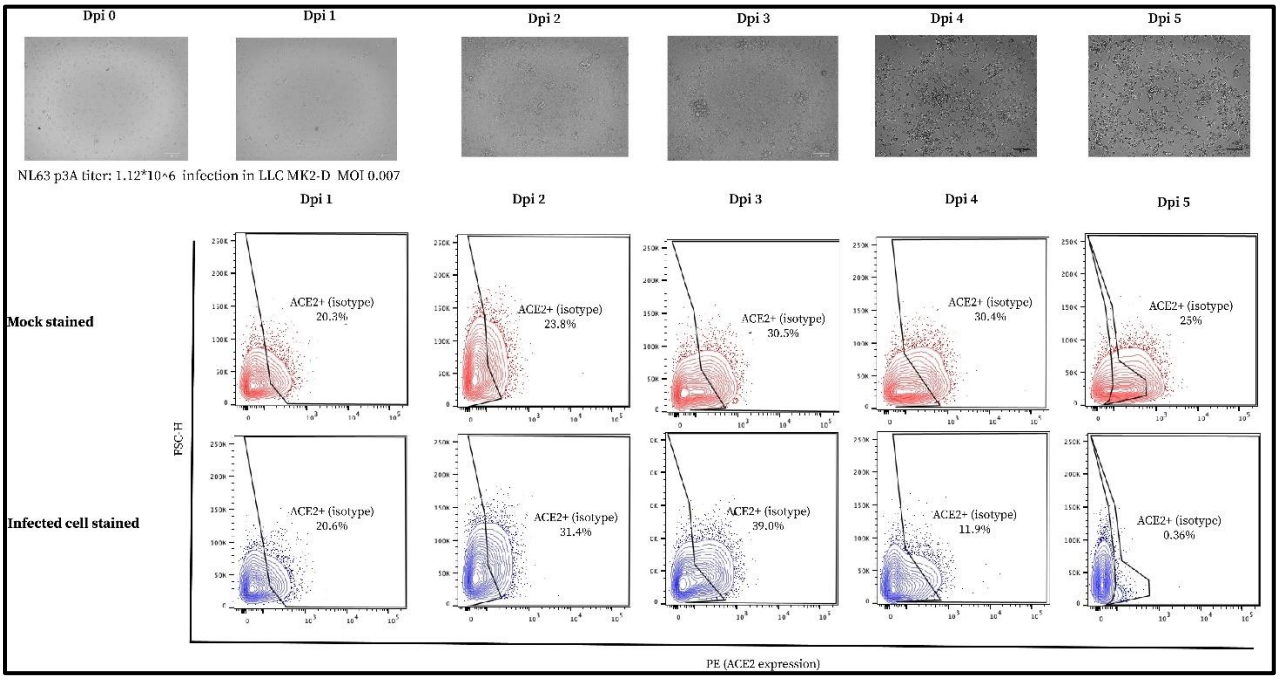

Figure 16. Kinetics analysis for infected LLC-MK2 cells using sHCoV-NL63 at MOI 0.007. LLC-MK2 cells were infected with sHCoV-NL63 at a multiplicity of infection (MOI) of 0.007 and analyzed at 1, 2, 3, 4 and 5 days post-infection (DPI). Cytopathic effects (CPE) in the upper row were qualitatively assessed by brightfield microscopy using a ZOE imaging system. Representative flow cytometry dot plots showing ACE2 surface expression (PE) in mock (red) and sHCoV-NL63-infected cells (blue). Data are from a single experiment.

Following the characterization of ACE2 receptor modulation during sHCoV-NL63 infection in LLC-MK2 cells (Figures 15 and 16), the observed infection-associated modulation was compared with previously published findings (Figure 17) to determine whether receptor modulation was consistent with independent observations.

Dijkman et al. (2012) described a dynamic regulation of ACE2 during sHCoV-NL63 infection, characterized by an early increase in ACE2 expression followed by progressive downregulation as infection progressed.

Despite differences in the methodology used to quantify ACE2 expression, both studies demonstrate a similar pattern of receptor modulation during sHCoV-NL63 infection. In our

experiments, ACE2 surface expression increased during the early stages of infection, reaching its highest level at 2–3 DPI before declining markedly at later time points. Likewise, Dijkman et al. (2012) reported an increase in ACE2 protein expression up to 3 DPI, followed by significant downregulation as viral replication progressed.

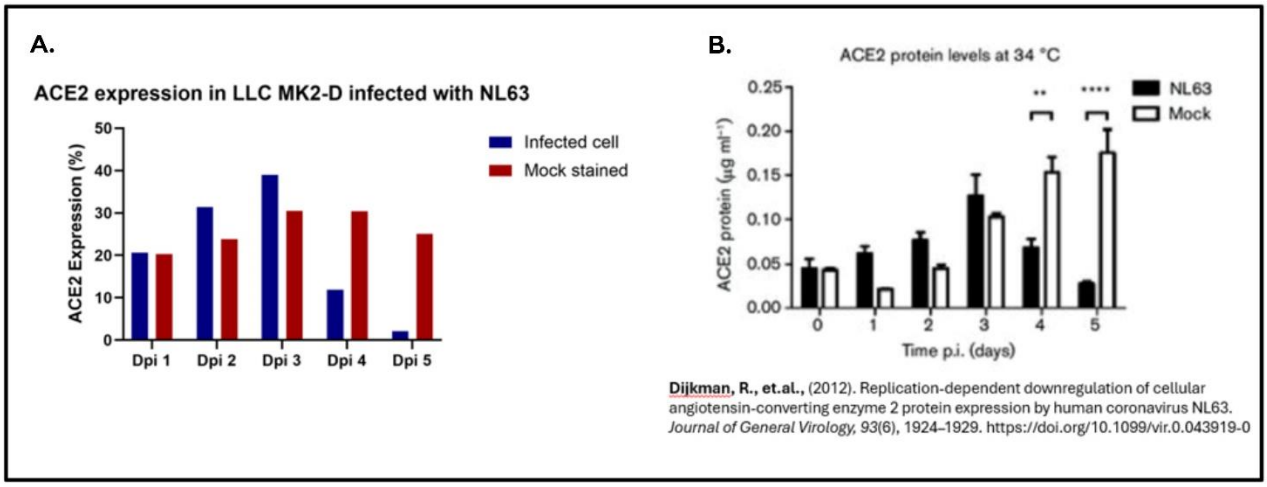

Figure 17. Comparison of ACE2 modulation during sHCoV-NL63 infection with previously published findings. (A) Flow cytometry analysis of ACE2 surface expression in LLC-MK2 cells infected with sHCoV-NL63 over a 5 DPI. Infected cells (blue) show an initial increase in ACE2 expression, peaking at dpi 3, followed by a marked decline at later time points, whereas mock-stained cells (red) show variation in ACE2 levels across time points. (B) Quantification of ACE2 protein levels following NL63 infection compared to mock-treated cells (adapted from Dijkman et al., 2012). ACE2 levels increase at early time points but are significantly reduced at later stages of infection.

Overall, despite differences in the magnitude of ACE2 modulation, the infection kinetics experiments supported the preliminary observations from our laboratory and further characterized ACE2 receptor modulation during productive sHCoV-NL63 infection. The results demonstrated a dynamic pattern in which ACE2 surface expression increased during the early stages of infection and subsequently declined as infection progressed. This characterization established an infection-associated phenotype that could then be used as a reference to address the central question of this study: whether the expression of individual sHCoV-NL63 proteins would be sufficient to induce significant ACE2 modulation. To investigate this question independently of the complete viral

infection context, a transient-expression approach was developed using plasmids encoding individual viral proteins. However, before assessing their effects on ACE2 surface receptor expression, it was necessary to establish and optimize the experimental conditions required for efficient transfection, reliable detection of plasmid and viral protein expression, and accurate measurement of surface ACE2 receptor. Therefore, the following experiments focused on the optimization and validation of the transient-expression system before its application to the individual sHCoV-NL63 viral constructs.

Optimization

Flow Cytometry of single fluorophore detection in transfected HEK293T

Prior to evaluating the effects of the individual viral proteins on ACE2 surface receptor expression and abundance, the experimental system was validated to establish reliable conditions for plasmid delivery and detection of the GFP and FLAG markers used throughout the study.

GFP-expressing control plasmids (peGFP-C3, peGFP-A2 or GFP-APOBEC2, and peGFP-A3G or GFP-APOBEC3) and FLAG-expressing control plasmids (pFLAG-A2 or FLAG-APOBEC2 and pFLAG-A3G or FLAG-APOBEC3) were initially transfected into HEK293T cells. These experiments were used to establish fluorescence detection parameters and to confirm that GFP-positive populations could be clearly distinguished from the background fluorescence observed in the mock and FLAG controls, ensuring the appropriate voltage adjustment, detection accuracy, and gating quality, and not as biological controls for changes in ACE2 expression.

Flow cytometry analysis demonstrated detectable FITC fluorescence in cells transfected with each GFP-expressing control plasmid, whereas mock cells and cells receiving FLAG constructs remained within the GFP-negative population, while the PE channel was used for additional gating (Figure 18). These results established that the selected FITC-channel settings were capable of distinguishing GFP-positive from GFP-negative cells and provided the gating framework

subsequently used to estimate GFP expression. GFP detection was interpreted as evidence of successful delivery and expression of the protein by the plasmid during transfection.

An additional figure showing the images of both brightfield and fluorescence from fluorescence microscopy was provided in Figure 7 in the Appendices. The images were captured using a ZOE microscope and a Zeiss microscope.

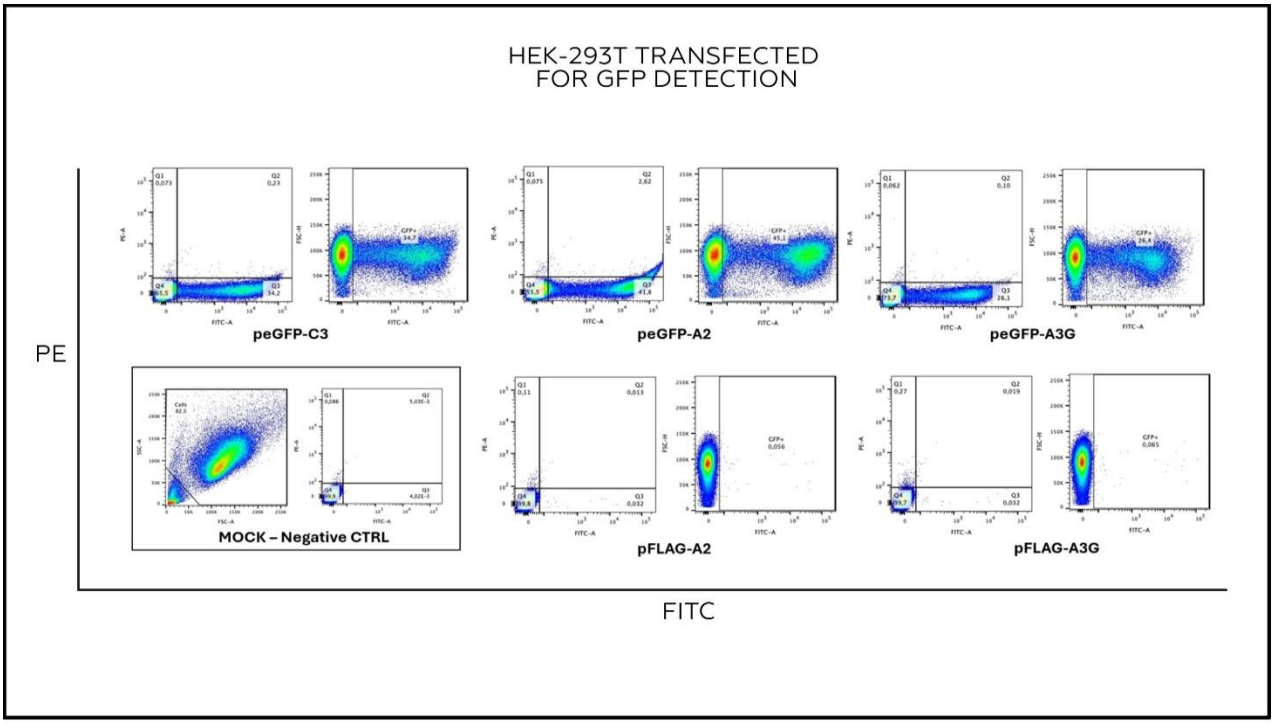

Figure 18. Validation of transfection efficiency and flow cytometry gating strategy using GFP-expressing control plasmids in HEK293T cells. The HEK293T cells were transfected with GFP-expressing control plasmids (peGFP-C3, peGFP-A2 or GFP-APOBEC2, and peGFP-A3G or GFP-APOBEC3) or FLAG-expressing plasmids (pFLAG-A2 or FLAG-APOBEC2 and pFLAG-A3G or FLAG-APOBEC3) as negative controls for transfected cells, to evaluate transfection efficiency and establish flow cytometry gating parameters. GFP expression was detected by FITC fluorescence, while the PE channel was used for additional gating.

Given the successful transfection results obtained by flow cytometry, we proceeded with the validation of those results by characterizing protein expression using western blot analysis (Figure 19).

GFP was detected in lysates from cells transfected with the GFP constructs, while FLAG was detected in the corresponding FLAG controls. β-tubulin was used as a loading control. These results confirmed the expression of GFP and FLAG in the respective transfected cells and demonstrated that the antibodies and detection conditions were suitable for the subsequent analysis of the viral constructs.

Western Blot of single-positive plasmid transfected in HEK293T

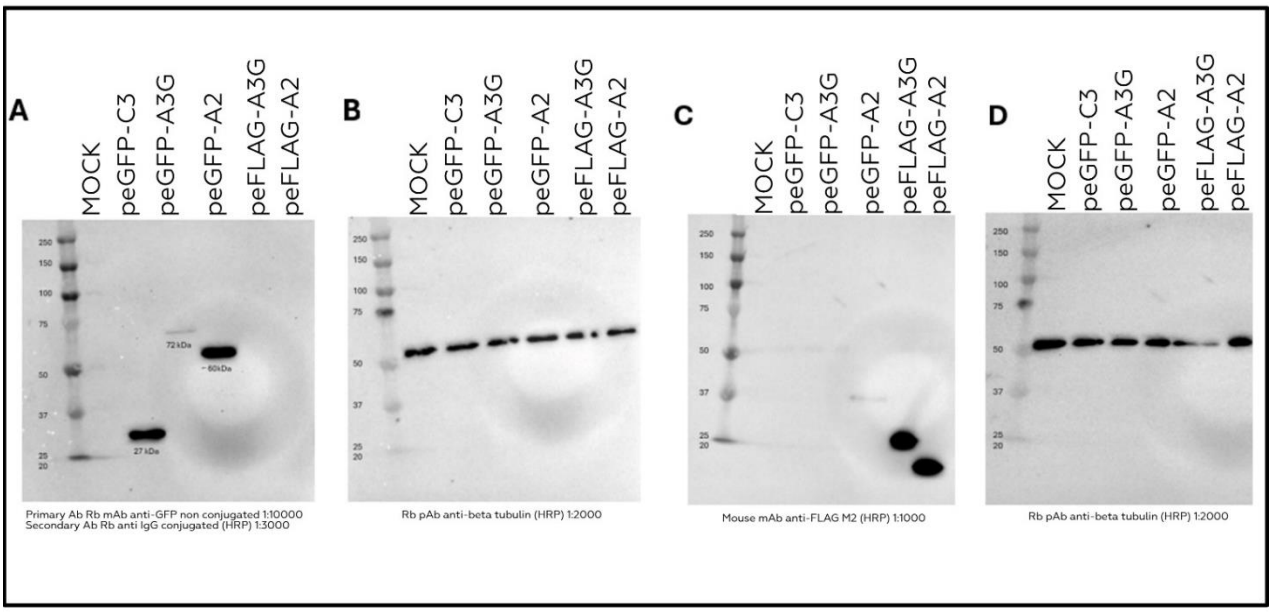

Figure 19. Validation of control plasmid expression by western blot in HEK293T cells. The HEK293T cells were transfected with GFP and FLAG expressing control plasmids (peGFP-C3, peGFP-A3G, peGFP-A2, peFLAG-A3G, and peFLAG-A2) to validate protein expression and optimize western blot detection conditions before analysis of viral protein constructs. Protein samples were separated by 10% SDS-PAGE. Panel (A) shows GFP detection using an anti-GFP primary antibody and secondary HRP-conjugated antibody; Panel (B) demonstrates β-tubulin detection corresponding to Panel (A), confirming equivalent protein loading. Panel (C) shows FLAG detection using the HRP-conjugated anti-FLAG M2 antibody. Panel (D) represents β-tubulin detection corresponding to Panel (C).

Flow Cytometry of double fluorophore detection in transfected HEK293T

Because the experimental strategy required simultaneous measurement of GFP and intracellular FLAG by flow cytometry, intracellular staining conditions were next evaluated using GFP, FLAG, double-reporter and isotype controls. As shown in Figure 20, the single-positive controls occupied the expected fluorescence populations, whereas the double-reporter construct generated a population positive for both GFP and FLAG. The threshold was set based on the isotype control, which was considered the negative region. These controls established that GFP fluorescence and

intracellular FLAG staining could be distinguished and provided the technical basis for subsequent simultaneous assessment of GFP, FLAG-tagged viral proteins and cell-surface ACE2.

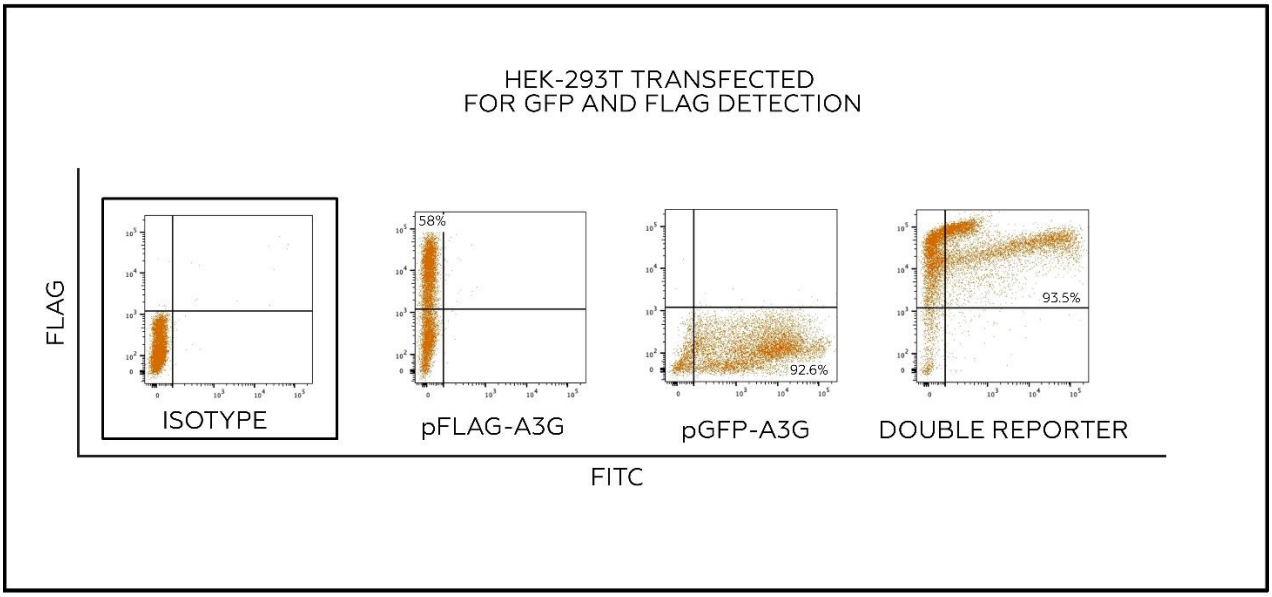

Figure 20. Validation of intracellular staining efficiency and flow cytometry detection of GFP and FLAG expression in HEK293T cells. The HEK293T cells were transfected with control plasmid constructs expressing FLAG (peFLAG-A3G) as a positive single fluorophore, GFP (pGFP-A3G) as a negative control, and a double-reporter plasmid. Cells were analyzed by flow cytometry to evaluate GFP expression (FITC channel) and FLAG detection by intracellular staining (Alexa Fluor 647 channel). The isotype control was used to establish background fluorescence and gating parameters.

Importantly, these optimization experiments validated the analytical detection system but did not establish that every subsequent viral construct would necessarily be expressed with equivalent efficiency. This distinction became important in later experiments, in which GFP and FLAG signals differed substantially among individual viral constructs.

Transfection Optimization in HEK293T+ACE2 cells

To ensure the best transfection efficiency, the amount of JetPRIME transfection reagent was optimized while maintaining 1 µg of plasmid DNA. Four JetPRIME amounts were evaluated using peGFP-A2 and a double-reporter control: 4.0, 3.5, 3.2 and 2.8 µL (Figure 21).

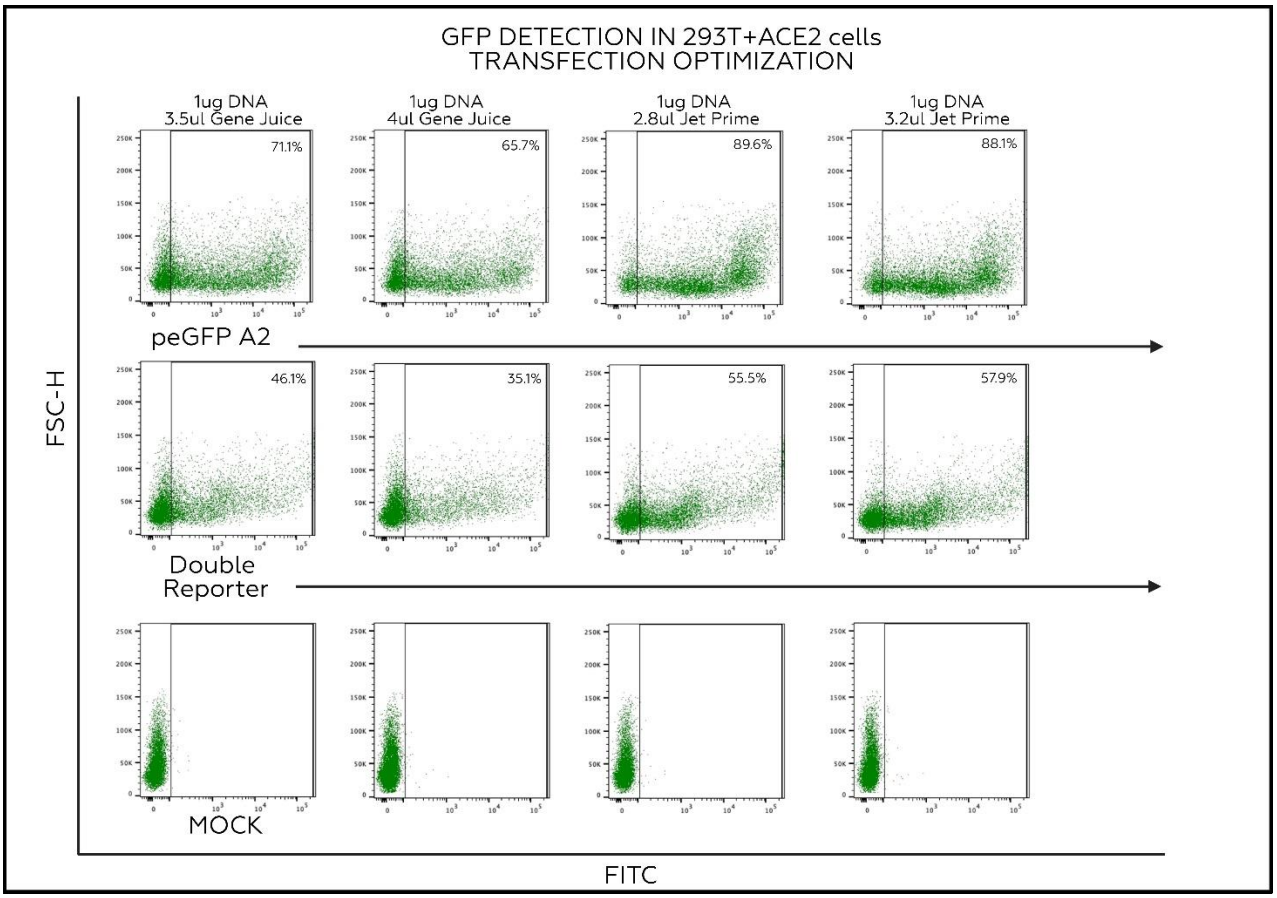

Figure 21. 293T+ACE2 optimization with control plasmids. Optimization of chemical transfection conditions in HEK293T+ACE2 cells using Jet Prime in different concentrations (4 µL, 3.5 µL, 3.2 µL, and 2.8 µL) with control plasmids (peGFP-A2 and double-reporter). GFP fluorescence was used to evaluate transfection efficiency, and cell morphology was monitored under the microscope using the brightfield to assess reagent-associated cytotoxicity.

Analysis of transfection efficiency showed that all tested reagent amounts resulted in successful transfection, indicating that an amount between 2.8 µL and 3.2 µL was the best

option to proceed. Based on these results, an additional trial was performed using the double-reporter control used previously, for which we already had a transfection efficiency reference, together with the viral plasmid vectors. For this working condition, we transfected HEK293T+ACE2 cells using 1µg of plasmid and 3 µL of transfection reagent (Figure 22).

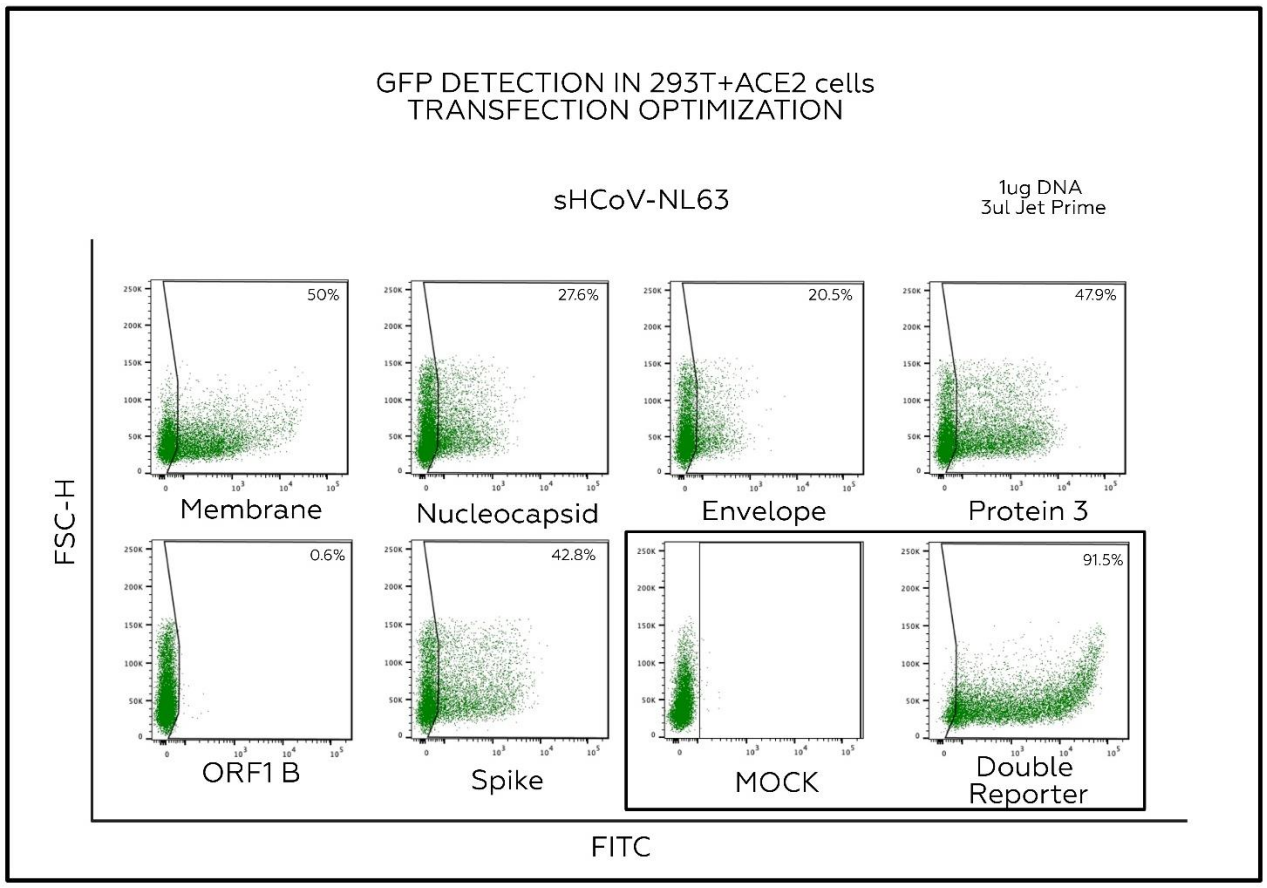

Figure 22. 293T+ACE2 transfected with viral protein plasmids. HEK293T+ACE2 cells were transfected using 3 µL of Jet Prime with 1ug of NL63 protein viral plasmids or a double-reporter control. GFP fluorescence was used to evaluate transfection efficiency in non-fixed cells.

GFP-positive populations were detectable in the FITC channel for almost all constructs, although their expression differed. This observation was important because it demonstrated that optimization of the transfection reagent alone did not eliminate construct-dependent variability.

Antibody Optimization in HEK293T+ACE2 cells

Antibody concentrations were next optimized to maximize separation between antigen-positive populations and background staining. For intracellular FLAG detection, the Alexa Fluor 647-conjugated anti-FLAG antibody was evaluated across multiple dilutions: 1:500, 1:1000, 1:2000, and 1:2500, using a double-reporter control and the sHCoV-NL63 Membrane construct (Figure 23). The corresponding isotype controls were used to assess nonspecific fluorescence.

Among the tested conditions, the 1:2000 dilution provided the most favourable discrimination between FLAG-positive samples and background staining and was therefore selected for subsequent analyses. The ability to detect the Membrane construct under these conditions additionally indicated that intracellular FLAG staining could be successfully applied to the viral constructs.

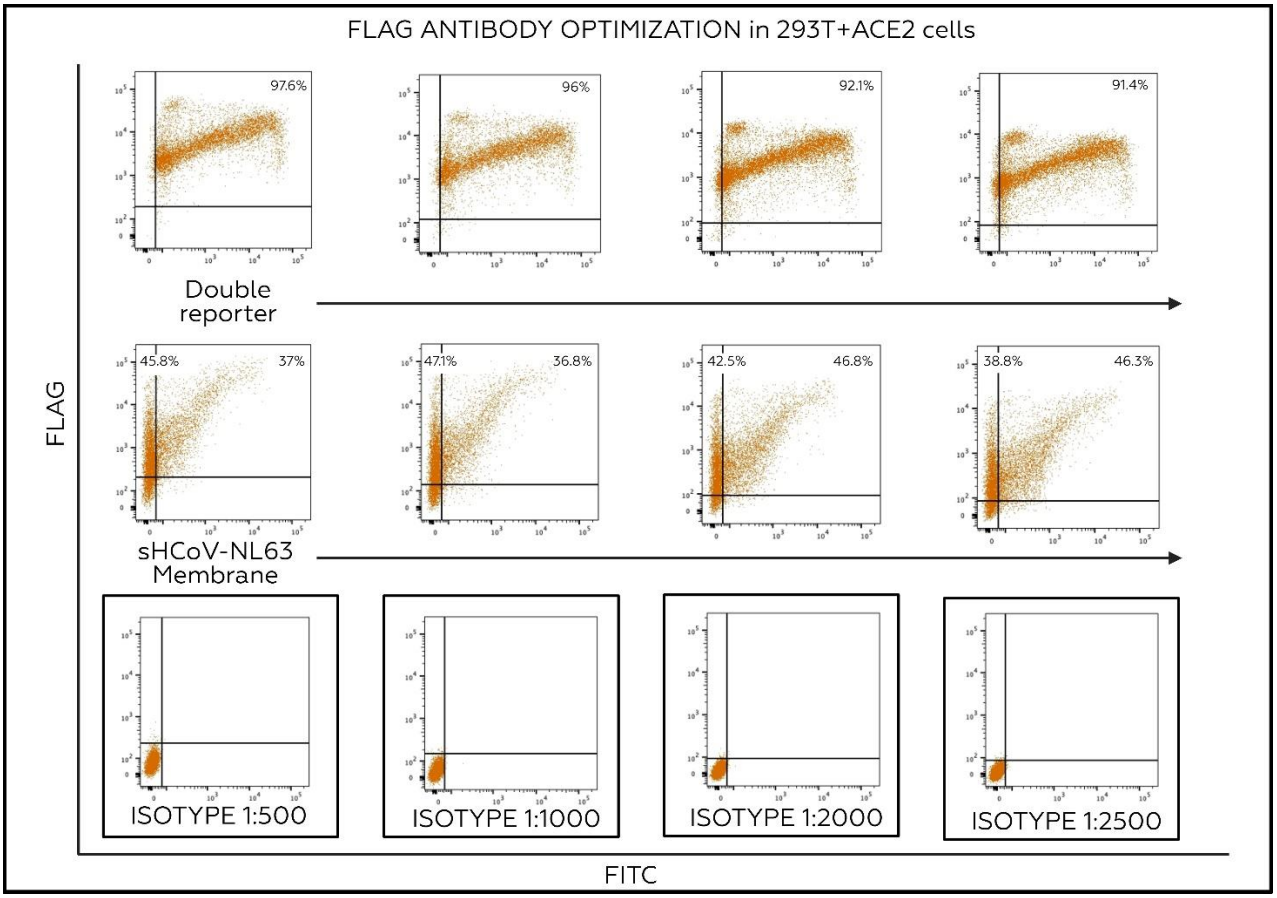

Figure 23. FLAG antibody titration. Optimization of FLAG antibody using an intracellular staining for flow cytometry. Different antibody concentrations (1:500, 1:1000, 1:2000 and 1:2500) were tested to determine the optimal signal-to-background ratio for subsequent analyses. The specific isotype antibody was used to exclude background and nonspecific binding.

ACE2 detection was similarly optimized by titrating the PE-conjugated secondary antibody at 1:100, 1:250, 1:500, and 1:700 dilutions, while maintaining the concentration of 3:100 for the primary anti-ACE2 antibody previously established by the laboratory. The 1:250 secondary-antibody dilution provided the most appropriate separation between ACE2-stained and isotype-control populations and higher efficiency and was therefore selected for subsequent experiments (Figure 24).

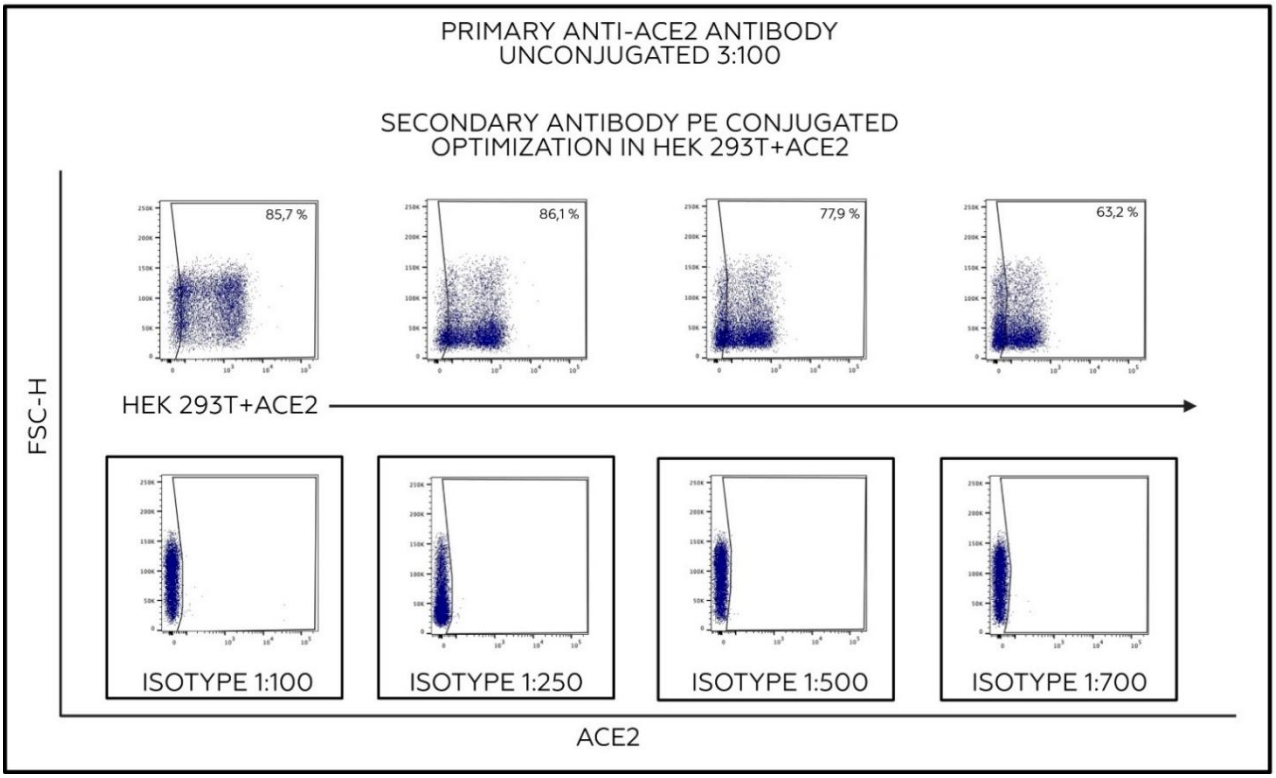

Figure 24. hACE2 Antibody titration and detection. Optimization of the secondary antibody concentration for ACE2 detection by flow cytometry. Different antibody concentrations (1:100, 1:250, 1:500 and 1:700) were tested to determine the optimal signal-to-background ratio for subsequent analyses. The primary antibody has already been titrated in previous experiments from the lab. The specific isotype antibody was used to exclude background and nonspecific binding.

These optimization experiments were particularly important because the central endpoint of this study depended on detecting potential differences in cell surface ACE2 expression.

Transfection Optimization in LLC-MK2 cells

In addition, transfection optimization using Lipofectamine reagent in LLC-MK2 cells was also performed. The optimization was performed using peGFP-A2 and sHCoV-NL63 Membrane protein plasmid under four transfection conditions: 2 µg plasmid + 5 µL of Lipofectamine reagent; 1.2 µg

plasmid + 7 µL of Lipofectamine reagent; 1.5 µg plasmid + 7 µL of Lipofectamine reagent; and 1.8 µg plasmid + 7 µL of Lipofectamine reagent (Figure 25).

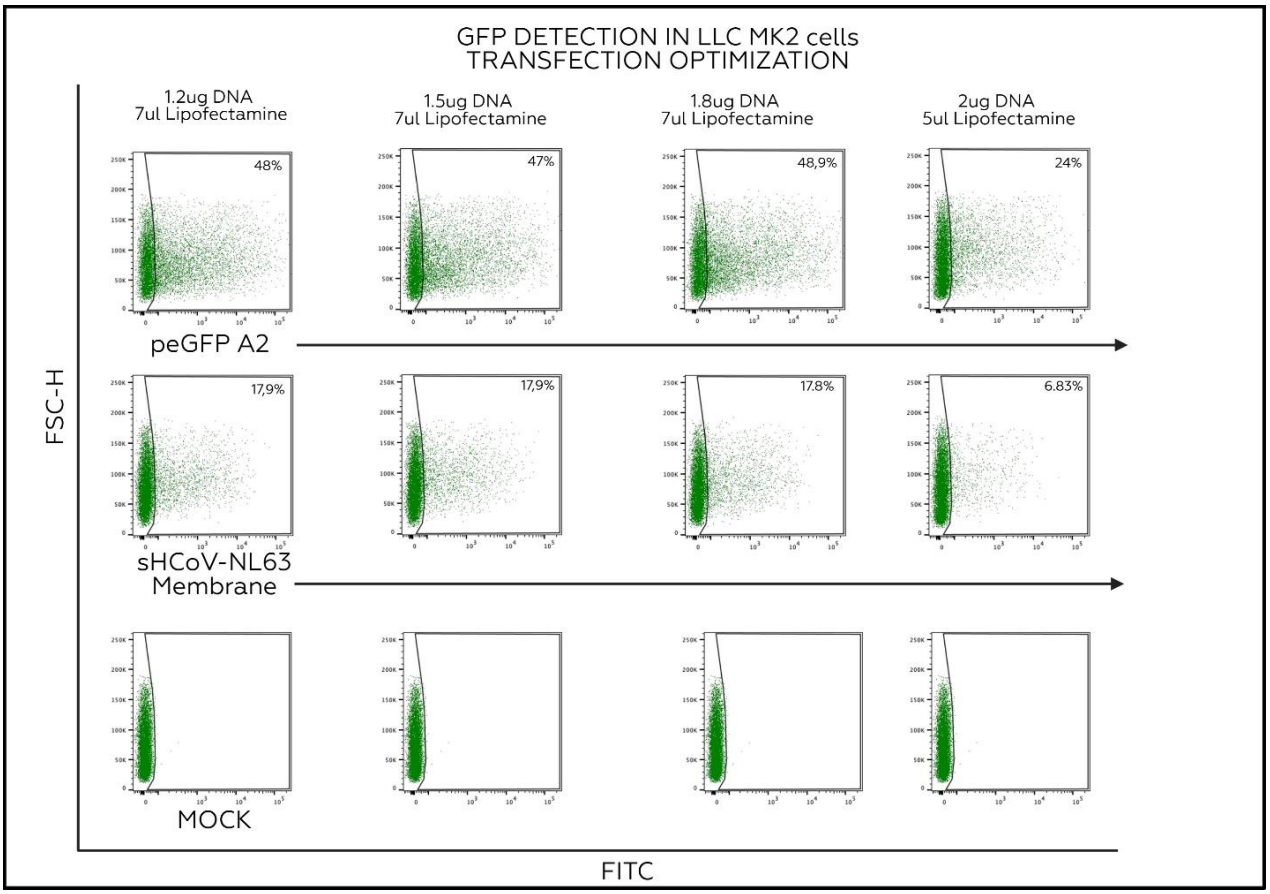

Figure 25. LLC-MK2 transfection optimization. Optimization of chemical transfection in LLC-MK2 cells using Lipofectamine 2000 in different concentrations and DNA ratios for NL63-Membrane protein plasmid and peGFP-A2 plasmid control (2ug plasmid + 5 µL of Lipofectamine reagent, 1.2ug plasmid + 7 µL of Lipofectamine reagent, 1.5ug plasmid + 7 µL of Lipofectamine reagent and 1.8ug plasmid + 7 µL of Lipofectamine reagent). GFP fluorescence was used to determine transfection efficiency following protocol optimization in non-fixed cells.

Among the evaluated conditions, 1.2 µg DNA combined with 7 µL of Lipofectamine 2000 produced the highest GFP-positive population and was therefore selected for subsequent experiments. Nevertheless, the optimization data also indicated that transfection in LLC-MK2 cells remained less efficient than in HEK293T+ACE2 cells.

Since we had already optimized both the transfection reagents and antibodies for transfection in both cell lines, we were ready to start the analysis and characterization of viral protein expression and receptor surface expression.

Expression and Characterization of Viral Proteins in HEK293T+ACE2 cells

Fluorescence microscopy analysis

To determine whether individual sHCoV-NL63 viral proteins can modulate ACE2 surface expression, we established a transfection-based system in HEK293T+ACE2 cells using plasmids expressing the individual proteins of sHCoV-NL63 to be evaluated and individual sHCoV-229E proteins as a physiological control, since sHCoV-229E does not behave as sHCoV-NL63 during infection, as illustrated in Figure 1 (Appendices).

HEK293T+ACE2 cells are permissive to sHCoV-NL63 infection (Milewska et al., 2014). Due to their high transfection efficiency, they can provide a more efficient transfection rate for analysis. These cells were transfected with a polycistronic plasmid encoding individual viral proteins and a GFP reporter gene in the same bicistronic mRNA. At 48 hours post-transfection, the GFP reporter, FLAG-tagged viral protein, and ACE2 receptor expression were assessed using fluorescence microscopy, flow cytometry, and western blot.

As illustrated in Figure 26, we started by evaluating transfection efficiency by detecting GFP reporter expression using fluorescence microscopy. As expected, in panel A, mock cells showed no detectable fluorescence, while the double-reporter control produced strong fluorescence, confirming the efficiency of the transfection.

Most constructs showed detectable GFP signal for both sHCoV-NL63 and sHCoV-229E constructs, confirming successful plasmid delivery, transcription, and translation. However, fluorescence intensity was not uniform among constructs. Among the sHCoV-NL63 constructs illustrated in panel

B, Membrane, Spike, and Protein 3 produced the strongest GFP signal, whereas Nucleocapsid and Envelope exhibited lower fluorescence. No detectable GFP signal was observed following transfection with the ORF1A and ORF1B constructs, suggesting unsuccessful transfection. Considering the large size of the ORF1a and ORF1b plasmids, around 14 and 18 Kb, this may have affected the transfection efficiency. Alternative approaches, including calcium chloride- and lipid-based transfection methods, were also evaluated but were unsuccessful.

Similarly, in panel C, all evaluated sHCoV-229E constructs generated variable GFP expression levels among the individual constructs. Membrane, Spike and Protein 4A produced the strongest GFP signal, while Nucleocapsid, Envelope and Protein 4B exhibited lower fluorescence.

Because the plasmids were of relatively similar sizes, the observed differences may instead reflect construct-specific factors affecting gene expression and protein homeostasis, including transcription efficiency, mRNA stability, translation efficiency, protein folding, trafficking, and degradation. However, GFP fluorescence in this system was used as an indicator of successful expression of the bicistronic transcript and its downstream reporter rather than as a direct quantitative measurement of the corresponding viral protein. Viral protein abundance was therefore independently assessed using the FLAG epitope in flow cytometry analysis.

Cytopathic effects (CPE) were also evaluated using brightfield imaging with the ZOE and Zeiss inverted microscopes, with no signs of toxicity observed (Figure 9 – Appendices).

As an exception, the results for ORF1a and ORF1b presented strong CPE, including a considerable number of cell deaths. Unfortunately, the images from these samples were unfortunately not successfully saved and therefore could not be included in this thesis.

Overall, the majority of the constructs were successfully expressed and presented a healthy morphology under the microscope following transient transfection, supporting their reliability for subsequent characterization by flow cytometry and western blot analyses.

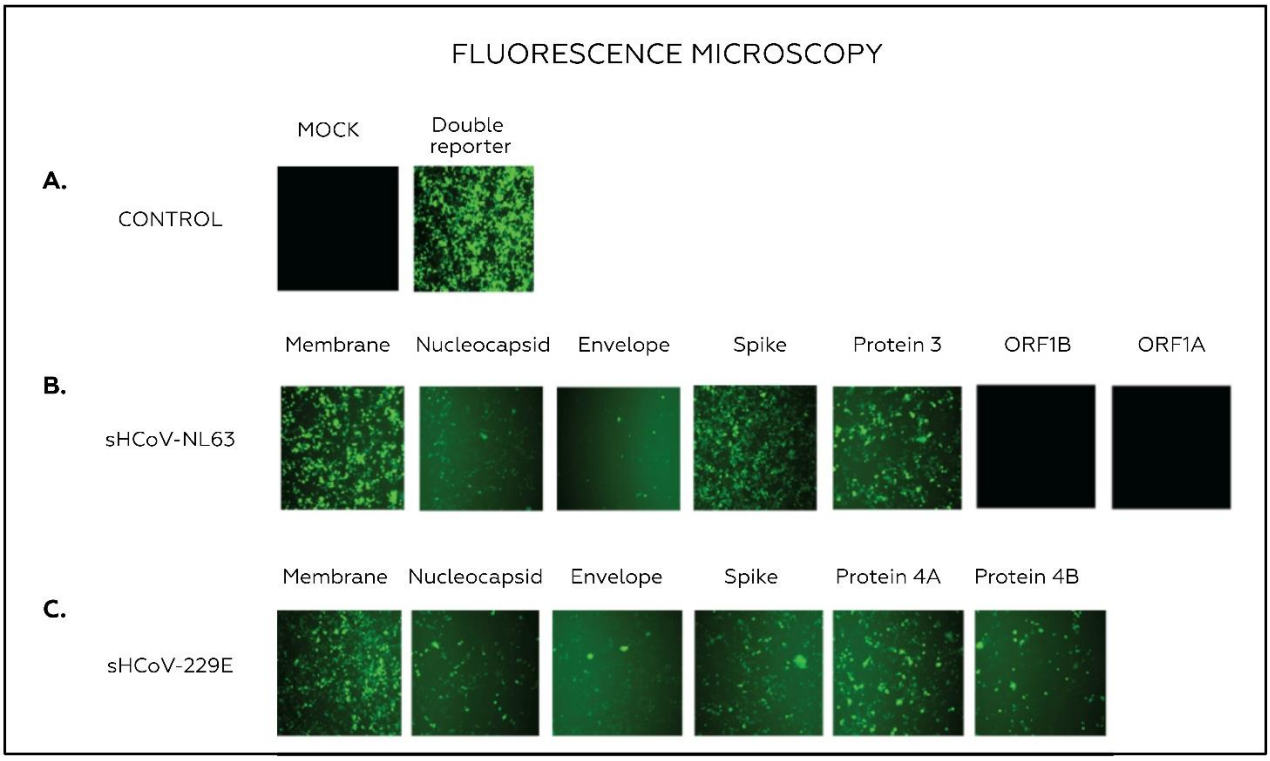

Figure 26. Fluorescence microscopy images of HEK293T+ACE2 cells transfected with individual sHCoV-NL63 and sHCoV-229E protein constructs. (A) Control conditions showing mock cells (negative control) and double-reporter cells (positive control). (B) Expression of the GFP reporter gene in a plasmid carrying individual viral proteins from sHCoV-NL63, including Membrane, Nucleocapsid, Envelope, Spike, Protein 3, ORF1B and ORF1A. (C) Expression of the GFP reporter gene in a plasmid carrying individual viral proteins from sHCoV-229E, including Membrane, Nucleocapsid, Envelope, Spike, Protein 4A and Protein 4B. Fluorescence intensity reflects the transfection efficiency. Images were acquired under identical microscopy settings for GFP detection. The experiment was independently performed three times.

Flow Cytometry analysis

Flow cytometry was performed to quantify three experimental parameters at the single-cell level: GFP detection using the FITC channel, intracellular viral protein expression through FLAG detection using the Alexa 647 channel, and receptor surface ACE2 levels using the PE channel. The analyses were performed at 48 hours post-transfection. Cells were stained for surface ACE2 before fixation and permeabilization, followed by intracellular FLAG staining. GFP fluorescence was measured by exogenous expression in the FITC channel.

Figure 27 illustrates the mean flow cytometry values from three experiments, with one replicate per experiment. The flow cytometry data confirmed the efficient transfection of the plasmid control. We observed variation in the efficiency of FLAG and GFP expression, with most constructs exhibiting a higher percentage of FLAG than GFP. This distinction was particularly evident for the sHCoV-NL63 Membrane, Nucleocapsid, Envelope and Protein 3 and sHCoV-229E Membrane, Nucleocapsid, and Protein 4A constructs.

This difference is likely attributable to the vector design. Following plasmid delivery into the cell, transcription is driven by the CMV promoter, forming a single bicistronic mRNA containing both the FLAG-tagged viral protein and the GFP reporter coding sequences. The FLAG-tagged viral protein is synthesized through the cap-dependent site, in which ribosomes are recruited to the 5’ cap of the mRNA and efficiently initiate translation. In contrast, GFP translation depends on the internal ribosome entry site (IRES), which allows ribosomes to initiate translation independently of the 5’ cap. Because IRES-mediated translation is generally less efficient than cap-dependent translation, a lower percentage of GFP expression compared to FLAG expression is consistent with the intrinsic design of the bicistronic expression vector (Mizuguchi et al., 2000; Shen et al., 2021; Gao & Wu, 2025)

On the other hand, a few constructs displayed the opposite trend, with these constructs exhibiting a higher percentage of GFP than FLAG, as observed for sHCoV-NL63 Spike and sHCoV-229E Envelope, Spike and Protein 4B. This suggests that construct-specific differences may interfere at multiple levels of gene expression and protein homeostasis, including mRNA stability, translational efficiency, protein folding, trafficking, and degradation, which were not investigated in this thesis.

Spike protein expression, in particular, displayed detectable GFP expression but little to no detectable FLAG signal. The presence of GFP indicates that the plasmid was successfully transfected, that transcription of the bicistronic transcript occurred, and that the IRES remained functional. Therefore, the reduced FLAG signal is unlikely to be explained by the vector design and instead suggests a construct-specific limitation affecting Spike protein expression or FLAG detection. Possible explanations include decreased protein stability, enhanced protein degradation, or reduced accessibility of the FLAG epitope due to protein folding.

Transfection of the ORF1a and ORF1b constructs was unsuccessful, as GFP expression was not detected and extensive cytopathic changes were observed by fluorescence microscopy, including cell death. Due to the toxicity, the values presented were measured from a small number of cells under unhealthy conditions, which would make our results for those plasmids less reliable. Consequently, ORF1a and ORF1b were excluded from subsequent analyses and will require alternative expression strategies in future studies.

Comparison of the fixed samples in Figure 27 with the non-fixed samples presented in the optimization section revealed a considerable reduction in GFP fluorescence following fixation and permeabilization. This observation was reproduced in an independent repeat of the experiment, in which a similar decrease in GFP signal was observed after sample processing, suggesting that the reduction was consistently associated with the fixation and permeabilization procedure. Loss of GFP fluorescence following fixation and permeabilization has been previously reported and

represents a recognized technical limitation when fluorescent proteins are analyzed after intracellular staining procedures (Fahlberg et al., 2024; Taves et al., 2019).

ACE2 receptor expression remained relatively consistent across the successfully transfected populations. Most constructs maintained ACE2 levels comparable to the mock-stained control, although a slight reduction was observed in some conditions, such as for sHCoV-NL63 Membrane, Envelope and Protein 3 and a modest increase for sHCoV-229E protein 4A. However, these differences were small relative to the overall ACE2-positive population and did not identify an individual sHCoV-NL63 protein that reproduced the ACE2 upregulation previously observed during infection.

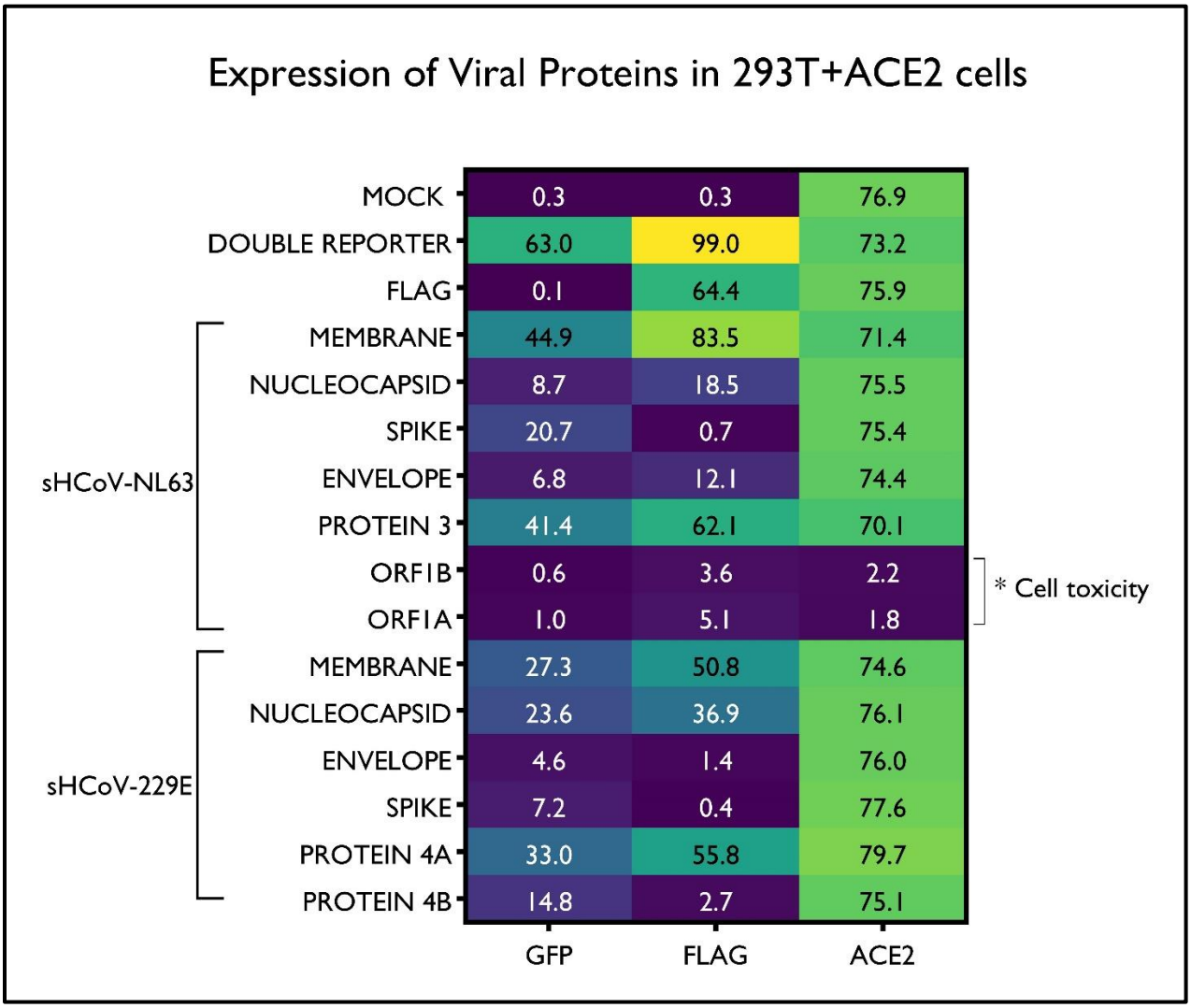

Figure 27. Percentage of cells expressing individual viral proteins in 293T+ACE2 cells. At 48 hours post-transfection, cells were harvested and stained for surface expression of the ACE2 receptor. Subsequently, the cells were fixed, permeabilized and stained for internal FLAG, which is in frame with the viral protein. Samples were then analyzed by flow cytometry: GFP expression was detected in the FITC channel and used to evaluate transfection efficiency, FLAG in the Alexa Fluor 647 channel for viral protein expression, and ACE2 in the PE channel to analyze the surface expression of the ACE2 receptor. The specific isotype antibody was used to exclude background and nonspecific binding. The experiment was independently performed three times, and the data are presented as the mean of the three independent experiments.

Quantification of ACE2 receptor expression (%) and geometric mean fluorescence intensity (gMFI)

Even though there were no substantial differences observed in the percentage of ACE2 receptor expression, the percentage of ACE2-positive cells determines how much of the analyzed population remains above the threshold established for ACE2 detection, but it does not distinguish differences in receptor abundance among cells that remain ACE2 positive. To assess this complementary measurement and increase the sensitivity of our analysis, we analyzed the geometric mean fluorescence intensity (gMFI) of ACE2. For these analyses, gMFI values were normalized to the corresponding isotype control by subtracting the isotype fluorescence from each sample value.

A modest variation in ACE2 gMFI was observed among the different viral protein expressions. Interestingly, the sHCoV-NL63 proteins and the physiological control displayed opposite trends. Cells expressing the sHCoV-229E proteins showed a modest tendency toward increased gMFI for ACE2 surface expression, whereas expression of the sHCoV-NL63 proteins was associated with a reduction in ACE2 gMFI, as shown in Figure 28.

Despite these trends, the magnitude of the observed differences was very minor and did not reach statistical significance following one-way ANOVA ($p = 0.8688$; significance threshold, $p < 0.05$). Pairwise comparisons were subsequently performed using Tukey's multiple-comparisons test to compare each viral protein with the mock-stained control and with the corresponding physiological control. The statistical analyses are summarized in Table 1 (Appendices).

Overall, none of the isolated viral proteins significantly modulated ACE2 surface expression or ACE2 fluorescence intensity under the tested experimental conditions.

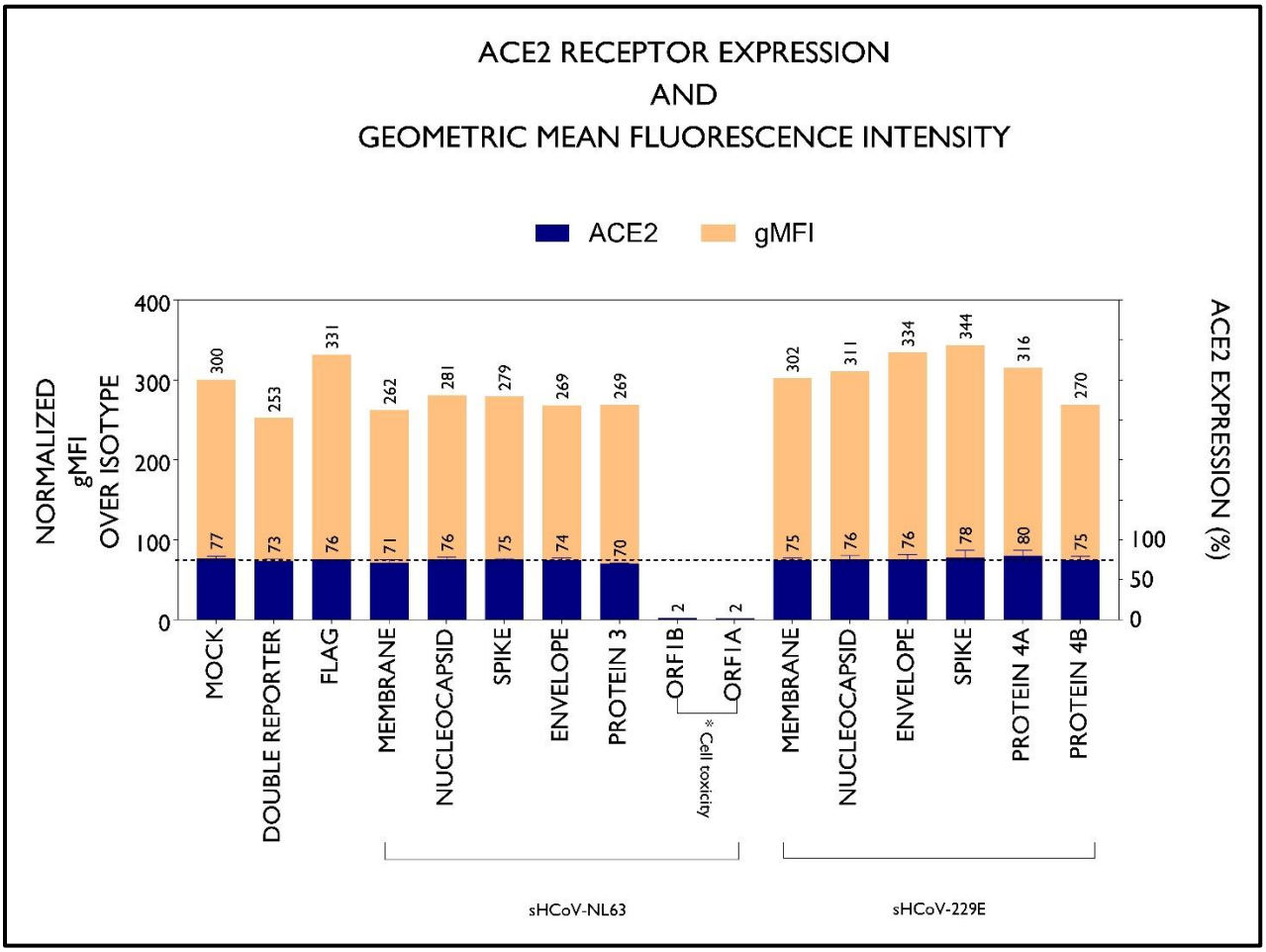

Figure 28. Quantification of ACE2 receptor expression (%) and geometric mean fluorescence intensity (gMFI) in transfected HEK293T+ACE2 cells. ACE2 represents the percentage of ACE2 receptors and gMFI the geometric mean fluorescence of the positive ACE2 cells. Values of gMFI were normalized against the corresponding isotype control. Statistical analysis was performed using one-way ANOVA followed by Tukey's multiple comparisons test, as represented in Table 1. Data represent the mean ± SD from three independent experiments.

Although flow cytometry confirmed the presence of FLAG-tagged viral proteins in transfected HEK293T+ACE2 cells, this approach does not provide protein characterization. Therefore, western blot analysis was performed to validate viral protein expression by confirming protein size and detection specificity, thereby complementing and strengthening the flow cytometry findings.

Western Blot analysis

Following the same pattern, the transfected HEK293T+ACE2 cells were collected and lysed at 48 hours post-transfection.

In Figure 29, western blot analysis of lysates from transfected HEK293T+ACE2 cells is presented across five panels. Panel A shows beta-tubulin detection, confirming comparable protein loading across all samples. Panels B and C demonstrate ACE2 and GFP expression, respectively; both were consistent with the flow cytometry results. Panel D shows the detection of FLAG and GFP controls, confirming successful expression, extraction, and detection of the transfected constructs.

Detection of FLAG-tagged viral proteins in Panel E required extensive optimization. Initial analyses performed using conventional SDS-containing loading buffer and heat denaturation resulted in a lack of FLAG detection for the viral proteins and successful detection of the control, despite successful transfection confirmed by flow cytometry and GFP detection using both methodologies. Therefore, multiple lysis buffers and protein extraction conditions were evaluated to improve protein recovery and FLAG detection (Figure 2 – Appendices). The best results were obtained using a non-SDS loading buffer with unheated samples subsequently resolved by SDS-PAGE.

Native-PAGE was also evaluated and produced a more distinct FLAG signal. However, protein migration was limited (Figure 10 – Appendices).

Under the optimized conditions, FLAG immunoblotting detected bands corresponding to the expected molecular weights for several constructs, although additional higher molecular weight bands were also detected. Based on previous reports describing detergent- and heat-induced aggregation of membrane proteins, these additional bands may represent aggregated protein species formed during sample preparation or electrophoresis (Lee et al., 2005; Sagné et al., 1996).

In Panel E, underlined bands indicate proteins migrating at the expected molecular weight, whereas boxed lanes identify samples in which no band was detected at the predicted size.

Overall, the western blot results confirmed that most viral constructs were successfully expressed, indicating that the lack of significant ACE2 modulation observed by flow cytometry could not be generally attributed to unsuccessful protein expression. These findings suggest that, under the experimental conditions tested, individual sHCoV-NL63 proteins were not sufficient to induce significant changes in ACE2 surface expression.

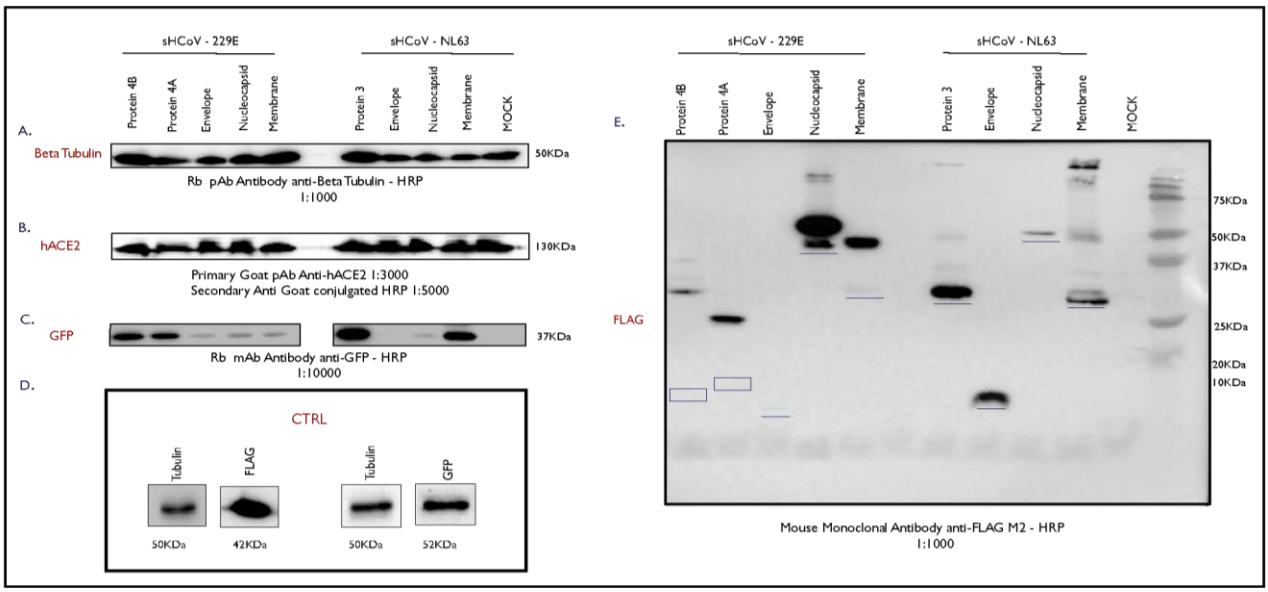

Figure 29. Western blot characterization of viral protein expression in HEK293T+ACE2 cells. (A) β-Tubulin loading control. (B) ACE2 protein detection. (C) GFP detection confirming transfection. (D) Control detection for FLAG-A2 and GFP-A2. (E) FLAG detection following optimization of protein extraction and electrophoresis conditions. Underlined bands indicate the expected molecular weight, whereas boxed lanes indicate absence of detectable protein. Non-SDS loading buffer and non-heated samples were used to minimize protein aggregation. 30 µL of each sample was loaded per lane in the gel (15 µL lysate + 15 µL loading buffer).

Fluorescence microscopy analysis for redesigned sHCoV-NL63 Spike protein construct

The initial characterization of the polycistronic viral protein constructs revealed a limitation in the detection of the sHCoV-NL63 Spike protein. Although GFP expression confirmed successful plasmid delivery and transcription of the construct, FLAG detection by both flow cytometry and western blot was almost nonexistent, suggesting that the low signal was not exclusively related to transfection efficiency. Since the Spike protein is a large and highly glycosylated membrane-associated protein that requires proper folding and processing, we hypothesized that the N-terminal positioning of the FLAG epitope may have affected protein stability, folding, or epitope accessibility.

To overcome this limitation, the sHCoV-NL63 Spike coding sequence was recloned into a monocistronic pcDNA3.1 expression vector with the FLAG tag relocated to the C-terminus. This redesigned construct was generated to minimize potential interference of the FLAG tag with protein expression and folding.

Fluorescence microscopy was initially performed to evaluate transfection efficiency. Since the redesigned Spike protein construct does not contain a GFP reporter gene, in addition to transfection with the Spike protein plasmid alone, cells were also co-transfected with the Spike protein plasmid and a GFP-expressing plasmid (GFP-A2), both cloned into the pcDNA3.1 expression vector. GFP fluorescence was used as an indicator of successful plasmid delivery, allowing the evaluation of transfection efficiency by microscopy.

Fluorescence microscopy in Figure 30 was performed at 48 hours post-transfection. Robust GFP fluorescence confirmed transfection efficiency in the co-transfected cells. As expected, the cells transfected with only the Spike protein plasmid did not present GFP fluorescence.

The Spike-expressing cells were subsequently evaluated for morphological alterations, revealing no sign of CPE, suggesting that expression of the redesigned sHCoV-NL63 Spike construct did not

induce detectable cytotoxic effects under the experimental conditions. The cells were analyzed, but no brightfield images were recorded.

Overall, fluorescence microscopy confirmed successful transfection, allowing subsequent characterization by flow cytometry and western blot analyses.

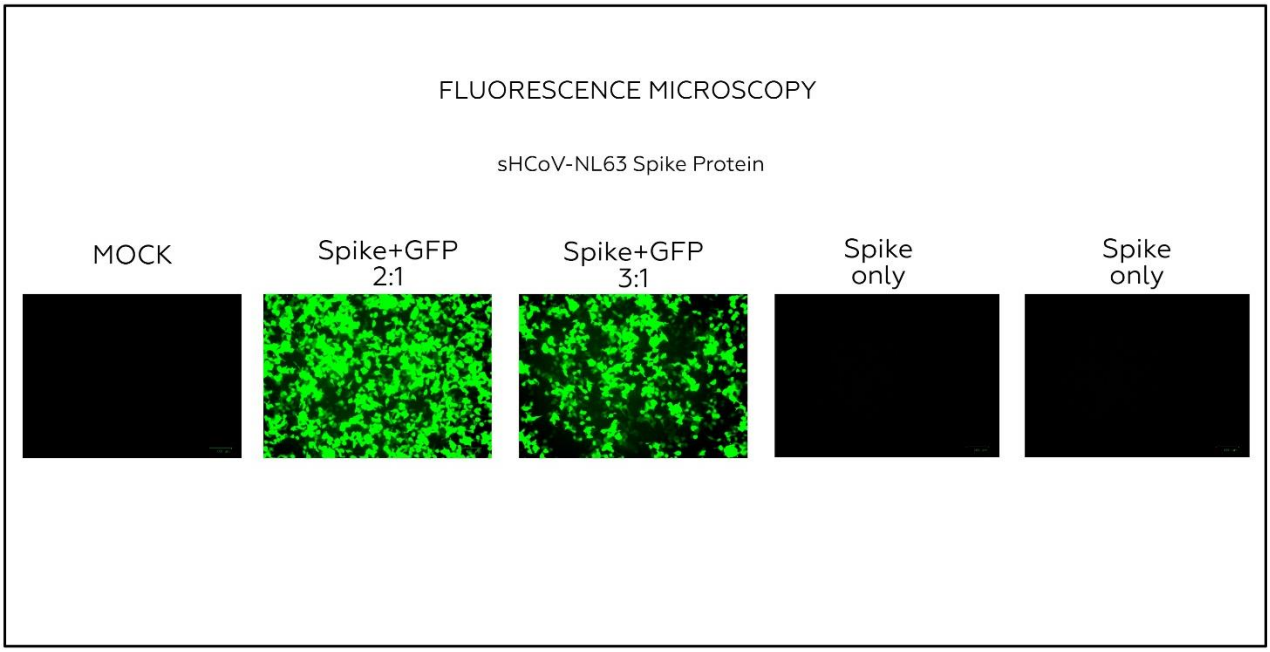

Figure 30. Fluorescence microscopy images of the redesigned monocistronic sHCoV-NL63 Spike construct containing a C-terminal FLAG tag, transfected in HEK293T+ACE2 cells alone and co-transfected with a GFP plasmid. HEK293T+ACE2 cells were transfected with the redesigned sHCoV-NL63 Spike protein plasmid alone, expecting no fluorescence, and co-transfected with the Spike protein plasmid and a GFP-expressing plasmid as a transfection control. Fluorescence microscopy was performed at 48 hours post-transfection to evaluate transfection efficiency based on GFP expression. The images were captured by the Zoe microscope. Data are from a single experiment with two replicates.

Flow Cytometry analysis of the redesigned sHCoV-NL63 Spike expression construct

Flow cytometry was performed to confirm and quantify Spike protein expression and evaluate its potential effect on ACE2 surface receptor expression. Both transfection conditions were analyzed: the Spike protein construct alone and co-transfected with a GFP-expressing construct (GFP-A2).

Transfection efficiency was measured by GFP detection in the co-transfected cells using the FITC channel; to assess intracellular FLAG-tagged viral protein expression, the Alexa 647 channel was used; and to determine receptor surface ACE2 levels, the PE channel was used. The analyses were performed at 48 hours post-transfection. The cells were stained for surface ACE2, fixed, permeabilized, and intracellularly stained for FLAG, while GFP was assessed by exogenous expression.

As shown in Figure 31, the flow cytometry results confirmed successful expression of the redesigned sHCoV-NL63 Spike protein. Spike protein expression was detected in approximately 30% of the cells transfected with the Spike construct alone, an equivalent percentage to that observed with the FLAG-A2 control construct. In the results for the co-transfected cells, we observed a small reduction in the percentage of FLAG-positive cells, reaching 23.8%, while GFP expression was detected in 47% of the cells under the experimental conditions. These results provided stronger evidence that redesigning the construct improved Spike protein detection by antibody recognition. However, the experiment performed cannot distinguish whether this resulted from improved epitope accessibility, protein stability, altered folding, increased protein abundance, or another feature of the redesigned expression system.

An increase in ACE2 surface expression was observed in Spike-expressing cells, for both the Spike-alone and co-transfected conditions. ACE2 expression increased from 43.7% in the mock to 51.4% following Spike transfection alone and 52.7% following Spike + GFP co-transfection.

Considering that the percentage of ACE2 expression relates to the number of cells expressing ACE2 receptor in a specific population, we decided to evaluate the intensity of ACE2 surface expression within the ACE2-expressing cells. Thus, the geometric mean fluorescence intensity (gMFI) was quantified among ACE2-positive cells. This analysis provides a more sensitive measurement of receptor expression levels compared with the percentage of ACE2-positive cells alone.

In addition, as will be mentioned in the description of Figure 37, where a greater discrepancy can be observed, these results should be interpreted with caution because the experiment was performed using a different antibody batch that resulted in weaker ACE2 detection, which indicates lower detection efficiency.

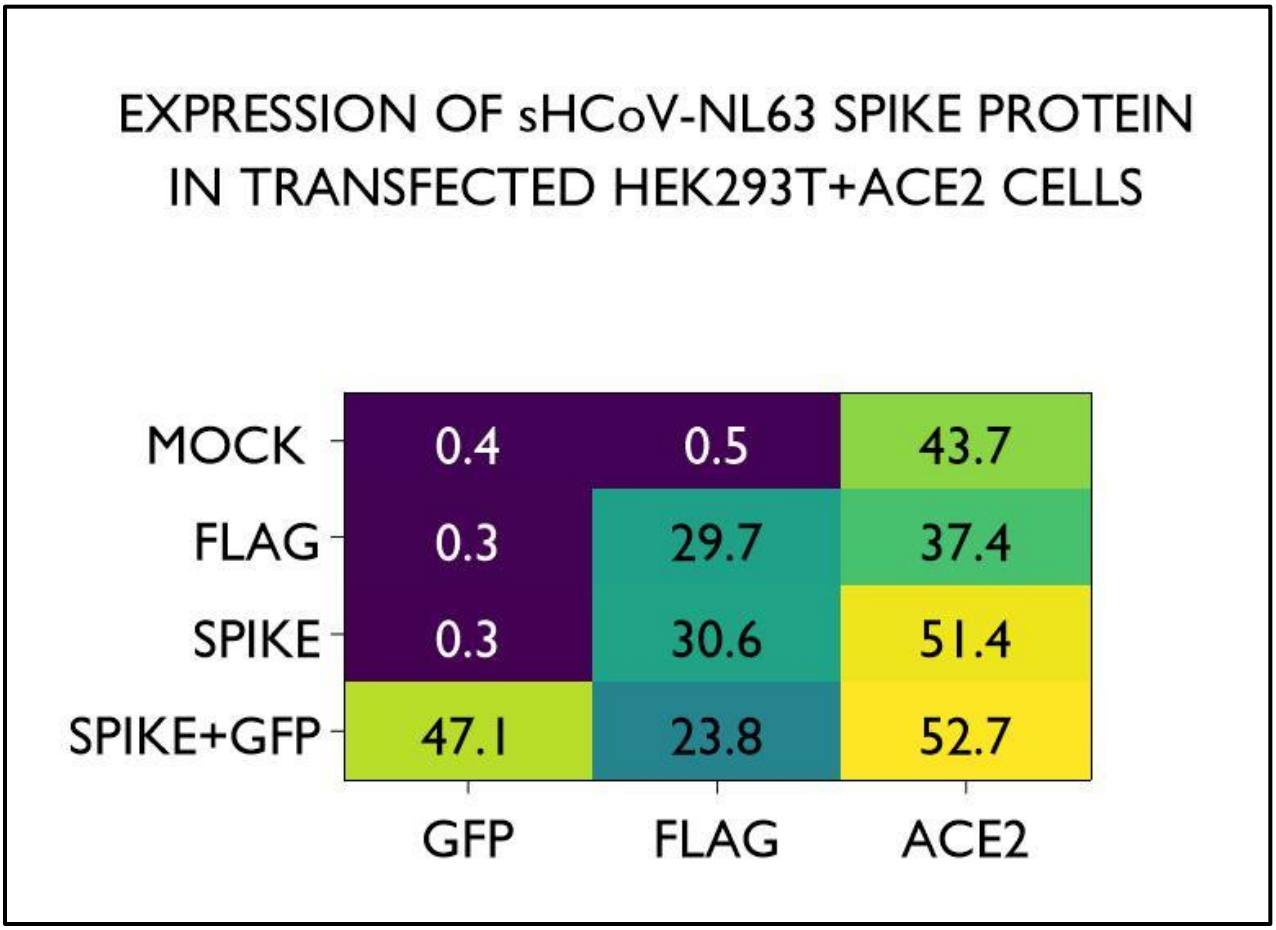

Figure 31. Flow cytometry analysis of the redesigned sHCoV-NL63 Spike construct expression in HEK293T+ACE2 cells. Cells were transfected with the C-terminal FLAG-tagged sHCoV-NL63 Spike construct alone or co-transfected with a GFP-expressing plasmid as a transfection control. At 48 hours post-transfection, cells were analyzed by flow cytometry to evaluate GFP fluorescence as an indicator of transfection efficiency by the FITC channel, FLAG expression as a measure of Spike protein expression by the Alexa Fluor 647 channel, and ACE2 surface expression to assess potential receptor modulation by the PE channel. The heatmap represents the percentage of positive cells for each analyzed marker. Data are from a single experiment with two replicates.

Quantification of ACE2 receptor expression (%) and geometric mean fluorescence intensity (gMFI) for redesigned sHCoV-NL63 Spike construct

To determine whether this modulation in ACE2 receptor expression observed by flow cytometry was significant, ACE2 geometric mean fluorescence intensity (gMFI) was quantified among ACE2-positive cells.

As represented in Figure 32, expression of the redesigned sHCoV-NL63 Spike construct resulted in very similar intensity values across the samples, with almost no increase in ACE2 gMFI compared with control cells. The difference observed did not reach statistical significance following one-way ANOVA ($p = 0.5954$; significance threshold, $p < 0.05$). Pairwise comparisons were subsequently performed using Tukey's multiple-comparisons test to compare each viral protein with the mock-stained control and with the corresponding physiological control. Consistent with the ANOVA results, none of the pairwise comparisons reached statistical significance. The statistical analyses are summarized in Table 1 (Appendices).

Overall, these findings indicate that the gMFI values for ACE2 did not support the modulation observed in the percentage of ACE2 expression, resulting in a non-significant statistical change.

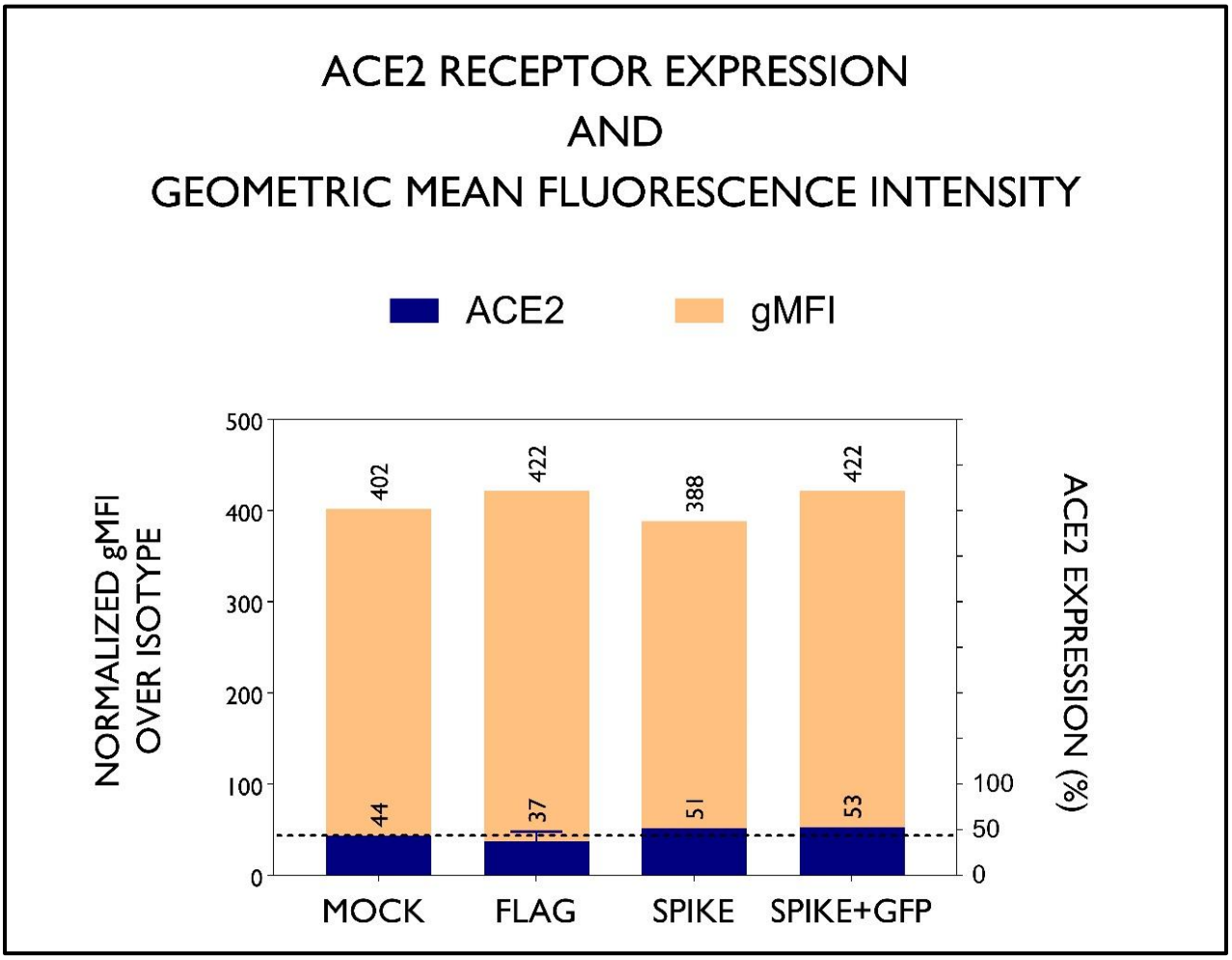

Figure 32. Quantification of ACE2 surface expression (%) and ACE2 geometric mean fluorescence intensity (gMFI) of the redesigned sHCoV-NL63 Spike construct expression in HEK293T+ACE2 cells. Quantification of ACE2 percentage and gMFI following Spike protein expression. Values were normalized against the corresponding isotype control. Statistical analysis was performed using one-way ANOVA followed by Tukey's multiple comparisons test, as represented in Table 1 (Appendices). Data are from a single experiment.

To further validate the expression of the redesigned sHCoV-NL63 Spike construct, western blot analysis was performed to assess protein expression and to determine whether the observed flow cytometry signal corresponded to detectable Spike protein levels.

Western Blot analysis of the redesigned sHCoV-NL63 Spike construct

As shown in Figure 33, beta-tubulin detection confirmed comparable protein loading across the experimental conditions. Detection of the FLAG-tagged Spike protein presented technical limitations. Despite successful transfection and the positive FLAG signal previously observed by flow cytometry, western blot analysis did not reveal a well-defined band corresponding to the expected molecular weight of the sHCoV-NL63 Spike protein. Instead, FLAG detection was characterized by diffuse smearing and poorly resolved signals. This pattern may reflect limitations including protein instability, aggregation, altered migration during electrophoresis, or glycosylation. Therefore, western blot analysis was insufficient to provide definitive evidence of Spike protein expression.

Nevertheless, when considered together with the positive FLAG staining detected by flow cytometry in Figure 31 and the dot blot analysis presented in Figure 34, these findings suggest successful expression of the Spike construct while highlighting the technical challenges associated with its detection by western blot. Further optimization of protein extraction and electrophoresis conditions will be necessary to achieve a more robust and specific validation of Spike expression.

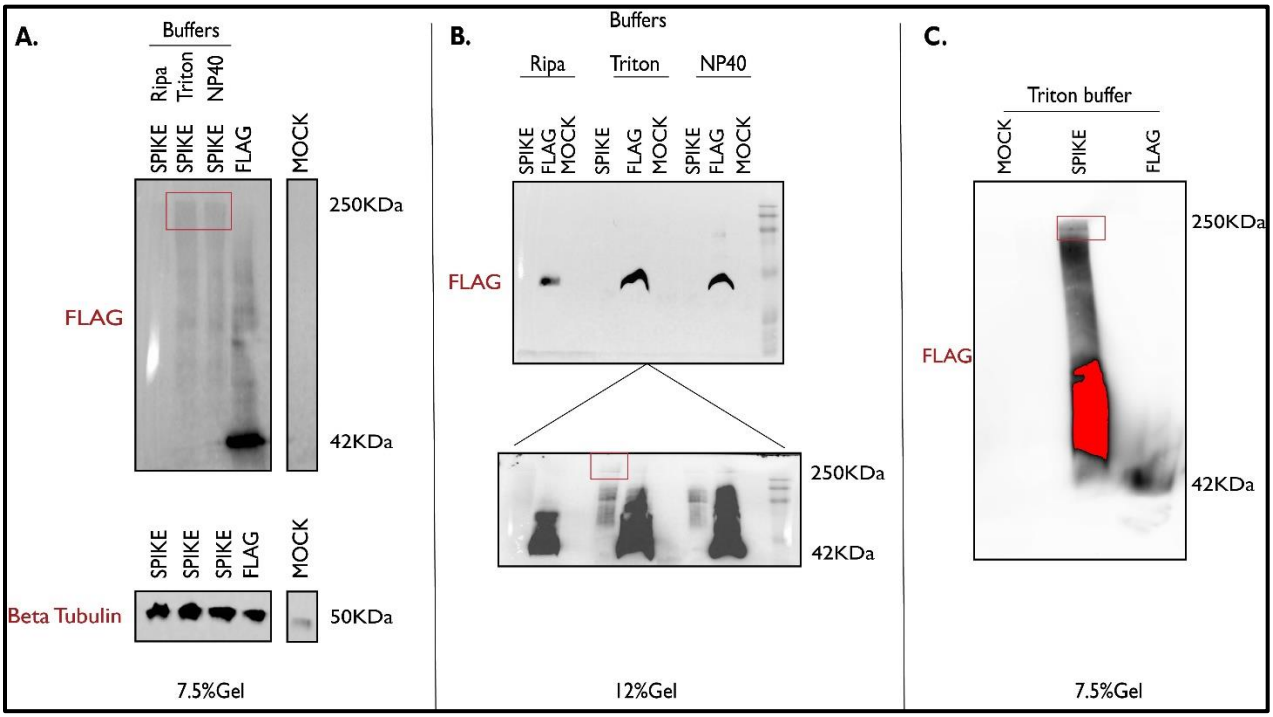

Figure 33. Western blot analysis of transfected HEK293T+ACE2 cells with the redesigned sHCoV-NL63 Spike construct using anti-FLAG antibody. Cells were transfected with the redesigned sHCoV-NL63 Spike construct or the FLAG-A2 control plasmid. Cell lysates collected in different conditions (RIPA, Triton, and NP40 Buffer) were analyzed by western blot using anti-FLAG antibody. β-Tubulin was used as a loading control to confirm comparable protein loading among samples. Although FLAG-positive signals were observed as diffuse smearing, no well-defined band corresponding to the expected molecular weight of the Spike protein (~150–220 kDa) was detected under the experimental conditions. Red boxes indicate a faint band present. These results demonstrate the technical limitations of detecting the sHCoV-NL63 Spike protein.

As a complementary validation for the expression of the FLAG-tagged sHCoV-NL63 and sHCoV-229E viral proteins, dot blot analysis was performed using lysates from transfected HEK293T+ACE2 cells on a nitrocellulose membrane.

Dot Blot analysis

The dot blot provides a complementary method to assess FLAG-tagged protein expression and allows the comparison of relative expression levels among different viral protein constructs, independently of protein migration and molecular weight resolution limitations associated with western blot analysis.

As illustrated in Figure 34, dot blot analysis confirmed the presence of FLAG-tagged viral proteins for the majority of the tested sHCoV-NL63 and sHCoV-229E constructs in transfected HEK293T+ACE2 cells. The detected signal intensity varied among the different viral proteins, suggesting differences in protein expression levels, consistent with the flow cytometry analysis. As previously observed in the flow cytometry data, the sHCoV-229E Spike construct showed no detectable signal under the tested conditions.

Overall, these findings support the successful expression of the majority of the viral protein constructs and validate their use for functional analyses evaluating their potential role in ACE2 modulation.

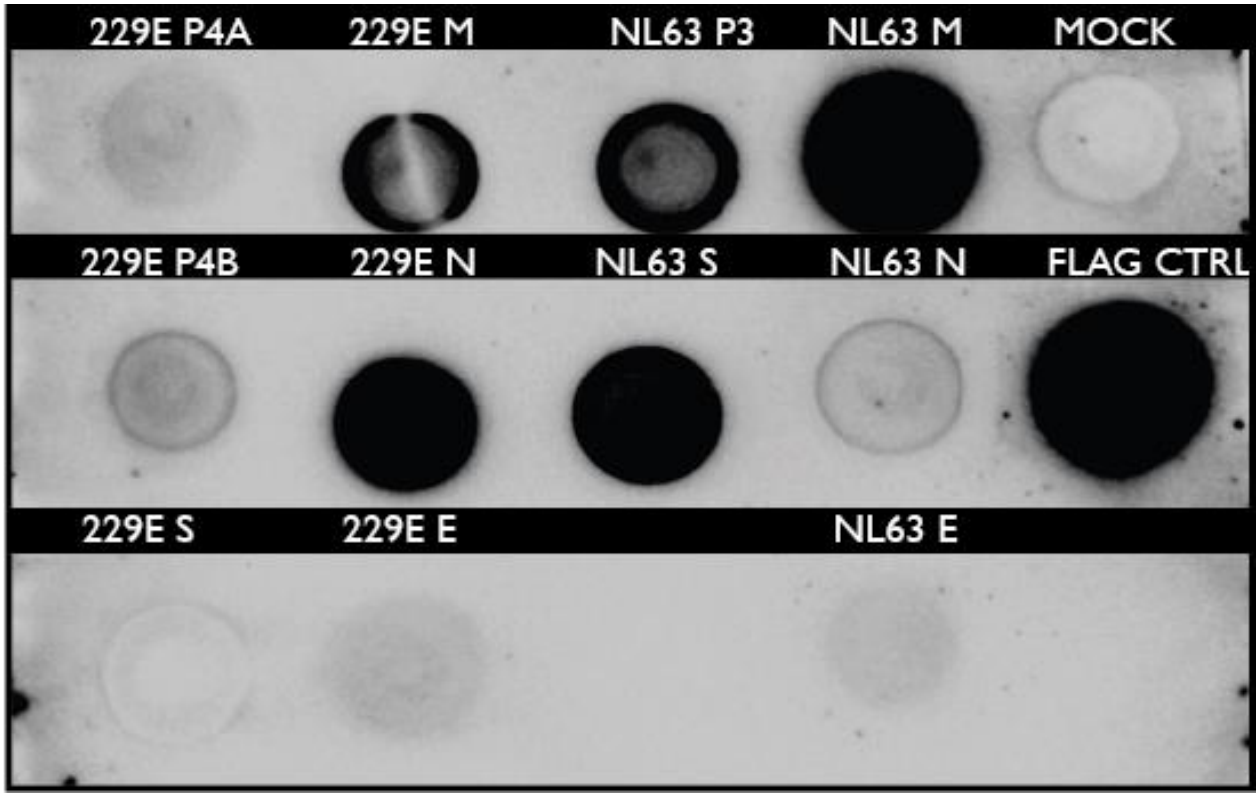

Figure 34. Dot blot analysis of FLAG-tagged viral protein expression in transfected HEK293T+ACE2 cells. Cell lysates from HEK293T+ACE2 cells transfected with individual sHCoV-NL63 and sHCoV-229E viral protein constructs were analyzed by dot blot using an anti-FLAG antibody to confirm the expression of FLAG-tagged proteins. MOCK- non transfected cells; FLAG CTRL-peFLAG-A2; NL63 M – NL63 Membrane; NL63 N – NL63 Nucleocapsid; NL63 E – NL63 Envelope; NL63 P3- NL63 Protein 3; NL63 S – redesigned NL63 Spike construct; 229E M – 229E Membrane; 229E N – 229E Nucleocapsid; 229E E – 229E Envelope; 229E P4A – 229E Protein 4A; 229E P4B – 229E Protein 4 B; 229E S – 229E Spike. Data are from a single experiment using 10 µL of lysate per sample.

Expression and Characterization of Viral Proteins in LLC-MK2 cells

Fluorescence microscopy analysis

Following the characterization of viral protein expression in HEK293T+ACE2 cells, the sHCoV-NL63 and sHCoV-229E protein constructs were further evaluated in LLC-MK2 cells. LLC-MK2 cells are one of the most commonly used cell lines for sHCoV-NL63 infection and represent the cell model used

in our laboratory's preliminary studies described in the rationale section (Figure 1. Appendices), where ACE2 modulation was initially observed during viral infection. As a cell line used for sHCoV-NL63 infection, this model was selected to determine whether the viral protein expression patterns observed in HEK293T+ACE2 cells were maintained while allowing comparison with our previous preliminary findings obtained using this cell line.

Fluorescence microscopy was initially performed to assess transfection efficiency, viral protein expression patterns, and potential cellular morphological changes associated with individual viral proteins (Figure 11– Appendices).

The fluorescence microscopy images, presented in Figure 35, were captured at 48 hours post-transfection, taking into account the relatively low transfection efficiency typically observed in LLC-MK2 cells. Despite this limitation, panel A shows the experimental controls: the double-reporter control confirmed successful transfection, showing substantial GFP expression, while, as expected, the mock cells exhibited no detectable fluorescence. In panel B, GFP reporter expression was detected following transfection with the sHCoV-NL63 constructs encoding Membrane, Nucleocapsid, Envelope, Spike, Protein 3, ORF1A, and ORF1B. The transfection efficiency varied among constructs, following the same pattern observed in HEK293T+ACE2 cells. As previously reported, no detectable fluorescence was observed for the ORF1A and ORF1B constructs.

Panel C shows GFP reporter expression in cells transfected with sHCoV-229E constructs encoding Membrane, Nucleocapsid, Envelope, Spike, Protein 4A, and Protein 4B.

Overall, the sHCoV-NL63 protein constructs exhibited higher expression levels than the corresponding sHCoV-229E constructs under the same experimental conditions. While the mechanism underlying this difference was not investigated in this study, it may reflect variation in construct-dependent or host cell-specific factors. Because LLC-MK2 cells are highly permissive to

sHCoV-NL63 infection, it is also possible that cellular factors contribute to the more efficient expression of sHCoV-NL63 proteins, although this hypothesis requires further investigation.

Given that the majority of the constructs were successfully expressed following transient transfection, they were subsequently characterized by flow cytometry and western blot analyses.

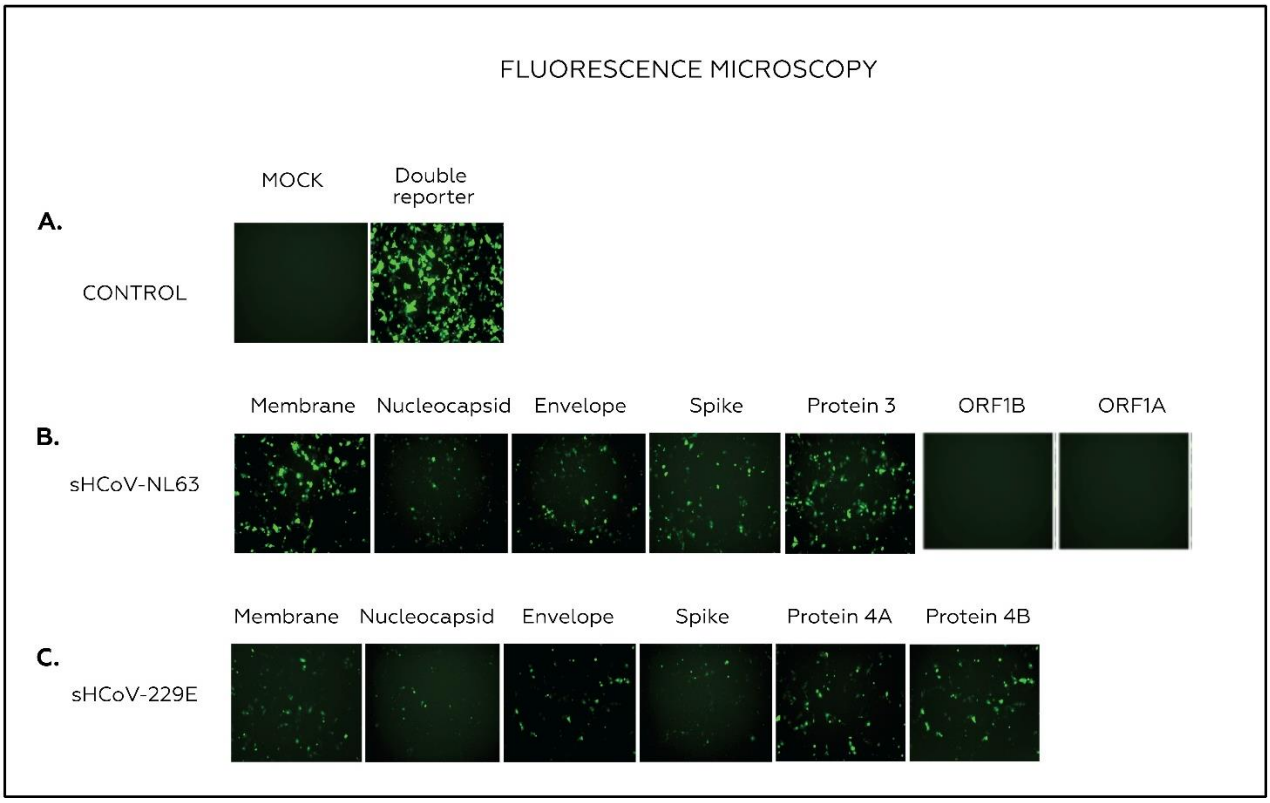

Figure 35. Fluorescence microscopy images of LLC-MK2 cells transfected with individual sHCoV-NL63 and sHCoV-229E protein constructs. (A) Control conditions showing mock cells (negative control) and double-reporter cells (positive control). (B) Expression of the GFP reporter gene in a plasmid carrying individual viral proteins from sHCoV-NL63, including Membrane, Nucleocapsid, Envelope, Spike, Protein 3, ORF1B and ORF1A. (C) Expression of the GFP reporter gene in a plasmid carrying individual viral proteins from sHCoV-229E, including Membrane, Nucleocapsid, Envelope, Spike, Protein 4A and Protein 4B. Fluorescence intensity reflects the transfection efficiency. Images were acquired under identical microscopy settings for GFP detection. The experiment was independently performed twice.

Flow Cytometry analysis

Following fluorescence microscopy evaluation, flow cytometry was performed to quantitatively assess transfection efficiency by GFP expression detected by the FITC channel, viral protein expression by the FLAG-tagged gene using the Alexa 647 channel, and ACE2 surface expression using the PE channel in transfected LLC-MK2 cells. This approach enabled the evaluation of whether specific viral proteins could influence ACE2 surface expression and comparison with the previously observed results in HEK293T+ACE2 cells.

Figure 36 illustrates the mean flow cytometry values from two independent experiments, with one replicate per experiment. Flow cytometry analysis confirmed efficient detection of the control plasmid, demonstrating successful transfection and validating the experimental conditions in LLC-MK2 cells. In contrast, cells transfected with the viral protein expression constructs exhibited lower transfection efficiencies.

Similar to the observations in HEK293T+ACE2 cells, all the polycistronic viral constructs, with the exception of the Spike protein, displayed a higher percentage of FLAG expression than GFP expression. Analysis of ACE2 surface expression revealed no major differences among the experimental groups, with cells expressing sHCoV-NL63 proteins presenting equal or lower ACE2 receptor expression, while cells expressing sHCoV-229E proteins presented lower ACE2 receptor expression.

Overall, flow cytometry analysis demonstrated that the viral protein constructs were successfully expressed in LLC-MK2 cells. Similar to the results obtained in HEK293T+ACE2 cells, no individual viral protein was identified as a clear mediator of ACE2 surface upregulation in the LLC-MK2 model. Nevertheless, the absence of a clear ACE2-upregulating phenotype across both cell models suggests that expression of the successfully evaluated individual viral proteins alone, not extending for nsps, may not be sufficient to induce the ACE2 receptor upregulation observed during sHCoV-

NL63 infection. Instead, ACE2 modulation may depend on additional viral components, host responses, or infection-associated processes that were not reproduced by isolated viral protein expression.

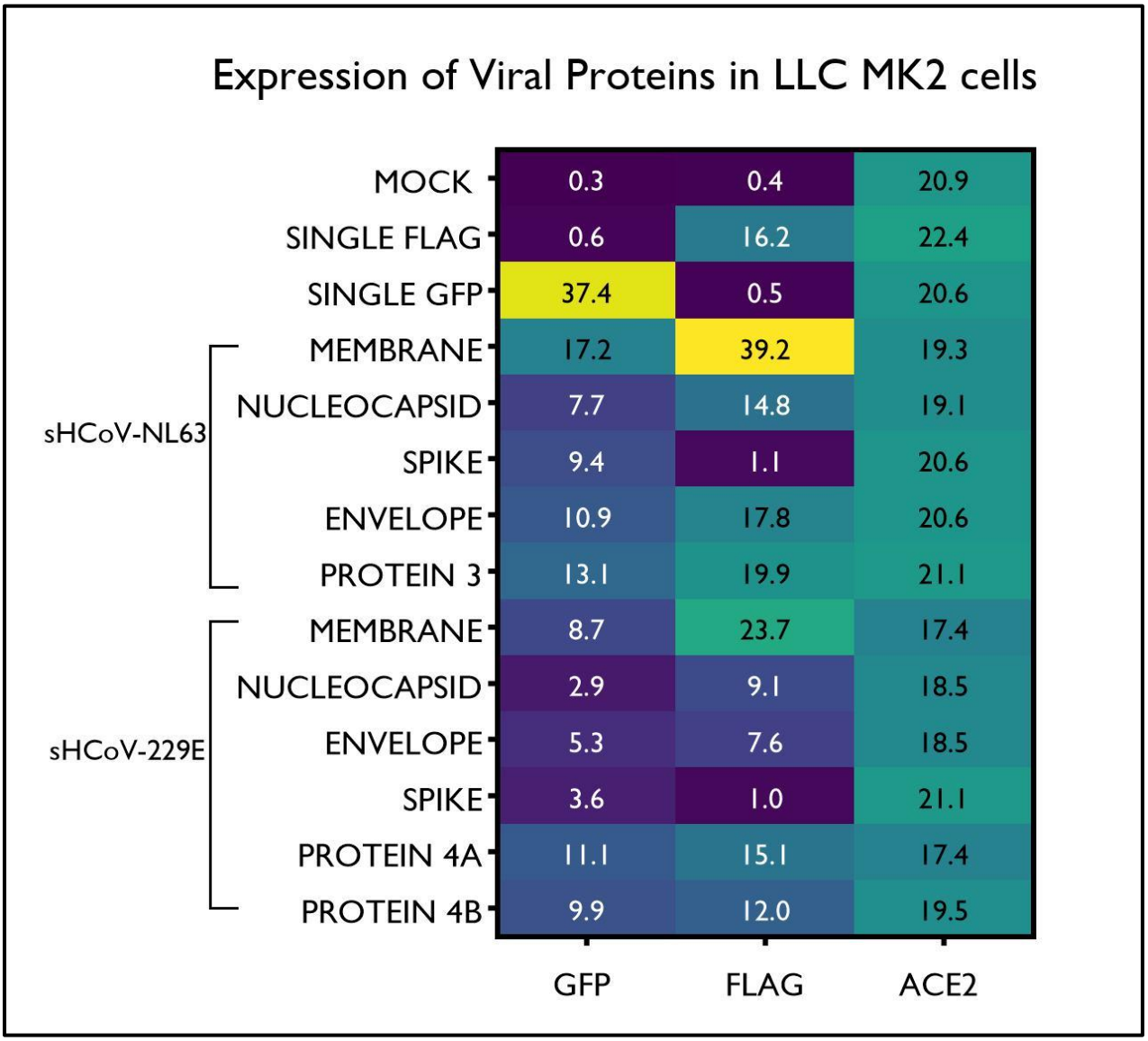

Figure 36. Percentage expression of individual viral proteins in LLC-MK2 cells. At 48 hours post-transfection, cells were harvested and stained for surface expression of the ACE2 receptor. Subsequently, the cells were fixed, permeabilized and stained for internal FLAG, which is in frame with the viral protein. Samples were then analyzed by flow cytometry: GFP expression was detected in the FITC channel and used to evaluate transfection efficiency, FLAG in the Alexa Fluor 647 channel for viral protein expression, and ACE2 in the PE channel to analyze the surface expression of the ACE2 receptor. The specific isotype antibody was used to exclude background and nonspecific binding. The controls included were GFP-A2 and FLAG-A2. The experiment was independently performed two times, and the data are presented as the mean of the two independent experiments.

Quantification of ACE2 receptor expression (%) and geometric mean fluorescence intensity (gMFI)

To further investigate the potential modulation of ACE2 surface expression intensity by individual sHCoV-NL63 and sHCoV-229E proteins, ACE2 receptor expression was quantitatively evaluated by measuring the geometric mean fluorescence intensity (gMFI) of ACE2-positive cells. Since flow cytometry analysis from Figure 36 did not reveal evident differences in the percentage of ACE2-positive cells among the experimental groups, gMFI analysis was performed to determine whether viral protein expression could alter the intensity of ACE2 surface expression on individual cells.

As shown in Figure 37, ACE2 surface expression remained relatively stable across all experimental groups. A slight reduction in ACE2 receptor expression was observed in both the physiological control and sHCoV-NL63-expressing conditions.

The geometric mean fluorescence intensity (gMFI) of ACE2-positive cells was calculated and normalized by subtracting the signal obtained from the corresponding isotype control. Analysis of the graph showed a modest reduction in ACE2 intensity for both groups: sHCoV-NL63 proteins and sHCoV-229E proteins.

Statistical analysis using one-way ANOVA showed no significant differences among the tested conditions ($p = 0.6946$; significance threshold, $p < 0.05$). Tukey's multiple-comparisons test was subsequently performed to compare each viral protein with the mock-stained control and the corresponding physiological control, as presented in Table 2 (Appendices). None of the tested isolated viral proteins induced a statistically significant modulation in ACE2 surface expression.

Although sHCoV-NL63 infection has previously been associated with ACE2 receptor modulation in LLC-MK2 cells in our preliminary observations mentioned in the rationale section (Figure 1.

Appendices), expression of individual viral proteins using the polycistronic expression system was insufficient to induce the ACE2 modulation observed during viral infection.

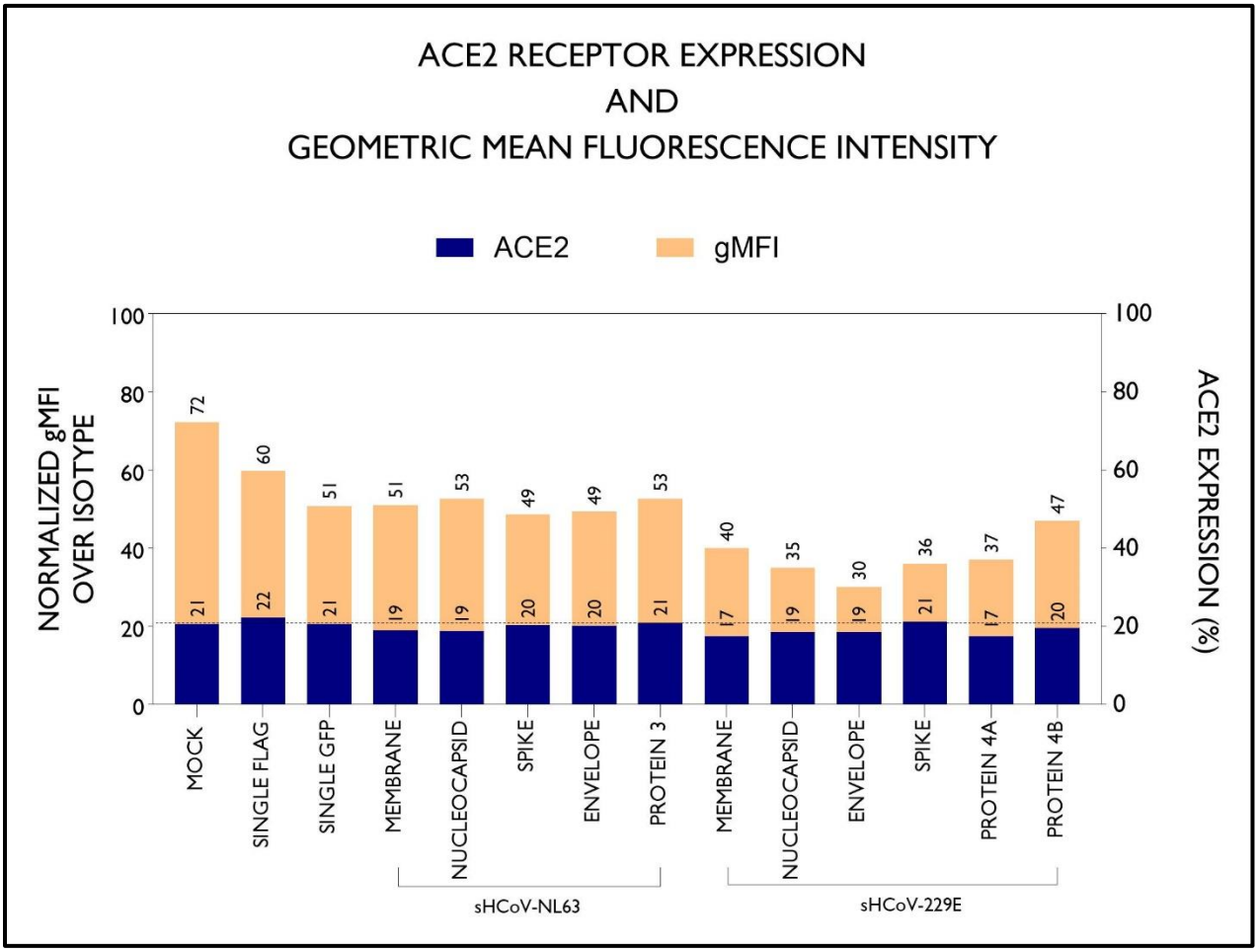

Figure 37. Quantification of ACE2 receptor expression (%) and geometric mean fluorescence intensity (gMFI) in transfected LLC-MK2 cells. Values of gMFI were normalized against the corresponding isotype control. Statistical analysis was performed using one-way ANOVA followed by Tukey's multiple comparisons test, as represented in table 2. Data represent the mean ± SD from three independent experiments.

To further validate viral protein expression detected by flow cytometry, western blot analysis was performed in transfected LLC-MK2 cells at 48 hours post-transfection to assess protein size and detection specificity, thereby complementing and strengthening the flow cytometry findings.

Western Blot analysis

In Figure 38, western blot analysis of LLC-MK2 cells transfected with the indicated constructs is shown in five panels. Panel A confirms the presence of beta-tubulin across all samples, supporting comparable protein loading. Panels B and C show ACE2 and GFP detection, respectively, both consistent with the flow cytometry results. Panel D shows co-detection of FLAG and GFP for the control plasmids, confirming successful expression and detection of the constructs.

As previously described for Figure 29, FLAG detection in Panel E presented a significant technical challenge, potentially attributable to protein aggregation upon contact with SDS in the loading buffer and during SDS-PAGE, compounded by thermal aggregation during the denaturation step (Lee et al., 2005; Sagné et al., 1996). Despite lower overall viral protein expression in LLC-MK2 cells, FLAG detection was achieved using a non-SDS loading buffer with unheated samples subsequently resolved by SDS-PAGE. For the majority of the constructs, bands corresponding to the expected molecular weights were detected alongside additional bands, which may have resulted from protein aggregation or altered migration under the experimental conditions. In Panel E, underlines indicate bands migrating at the expected molecular weight, while boxes indicate lanes where the expected band was absent.

Overall, western blot analysis confirmed the expression of most of the FLAG-tagged viral proteins in LLC-MK2 cells and supported the expression profiles observed by flow cytometry. These results confirm that the polycistronic constructs were expressed in LLC-MK2 cells.

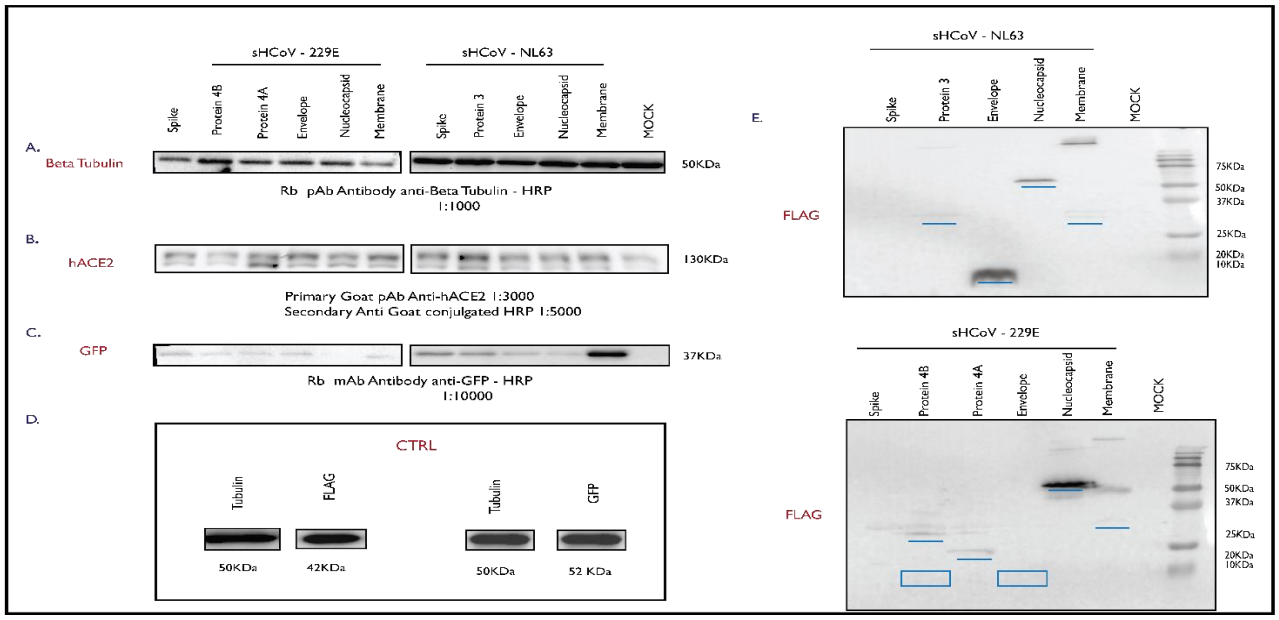

Figure 38. Western blot characterization of viral protein expression in LLC-MK2 cells. (A) β-Tubulin loading control. (B) ACE2 protein detection (C) GFP detection confirming transfection. (D) Control detection for FLAG-A2 and GFP-A2 detection. (E) FLAG detection following optimization of protein extraction and electrophoresis conditions. Underlined bands indicate the expected molecular weight, whereas boxed lanes indicate absence of detectable protein. Non-SDS loading buffer and non-heated samples were used to minimize protein aggregation. 30 µL of each sample was loaded per lane in the gel (15 µL lysate + 15 µL loading buffer).

Fluorescence microscopy analysis for redesigned sHCoV-NL63 Spike protein construct

The initial characterization of the polycistronic viral protein constructs revealed a limitation in the detection of the sHCoV-NL63 Spike protein, as also presented in the HEK293T+ACE2 analysis. GFP expression confirmed successful plasmid delivery and transcription, while FLAG detection by both flow cytometry and western blot was almost nonexistent.

To overcome this limitation, the same sHCoV-NL63 Spike construct recloned into a monocistronic pcDNA3.1 expression vector with the FLAG tag relocated to the C-terminus was also transfected into LLC-MK2 cells for analysis. This redesigned construct was previously evaluated in

HEK293T+ACE2 cells in Figures 30-33, where it presented minor changes in the percentage of ACE2-positive cells but not in ACE2 gMFI.

Fluorescence microscopy was initially performed to evaluate transfection efficiency. Since the redesigned Spike protein construct does not contain a GFP reporter gene, in addition to transfection with the Spike protein plasmid alone, cells were also co-transfected with the Spike protein plasmid and a GFP-expressing plasmid, both cloned into the pcDNA3.1 expression vector. GFP fluorescence was used as an indicator of successful plasmid delivery, allowing the evaluation of transfection efficiency by microscopy.

As shown in Figure 39, fluorescence microscopy performed at 48 hours post-transfection demonstrated considerable GFP fluorescence in co-transfected cells, indicating successful transfection under the experimental conditions. As expected, cells transfected with the Spike construct alone did not exhibit GFP fluorescence.

The Spike-expressing cells were subsequently evaluated for morphological alterations, revealing no sign of CPE, suggesting that expression of the redesigned sHCoV-NL63 Spike construct did not induce detectable cytotoxic effects under the experimental conditions. The cells were analyzed, but no brightfield images were recorded.

Overall, fluorescence microscopy demonstrated successful transfection under the tested conditions, supporting the subsequent characterization of Spike protein expression and analyses of its potential role in ACE2 receptor modulation.

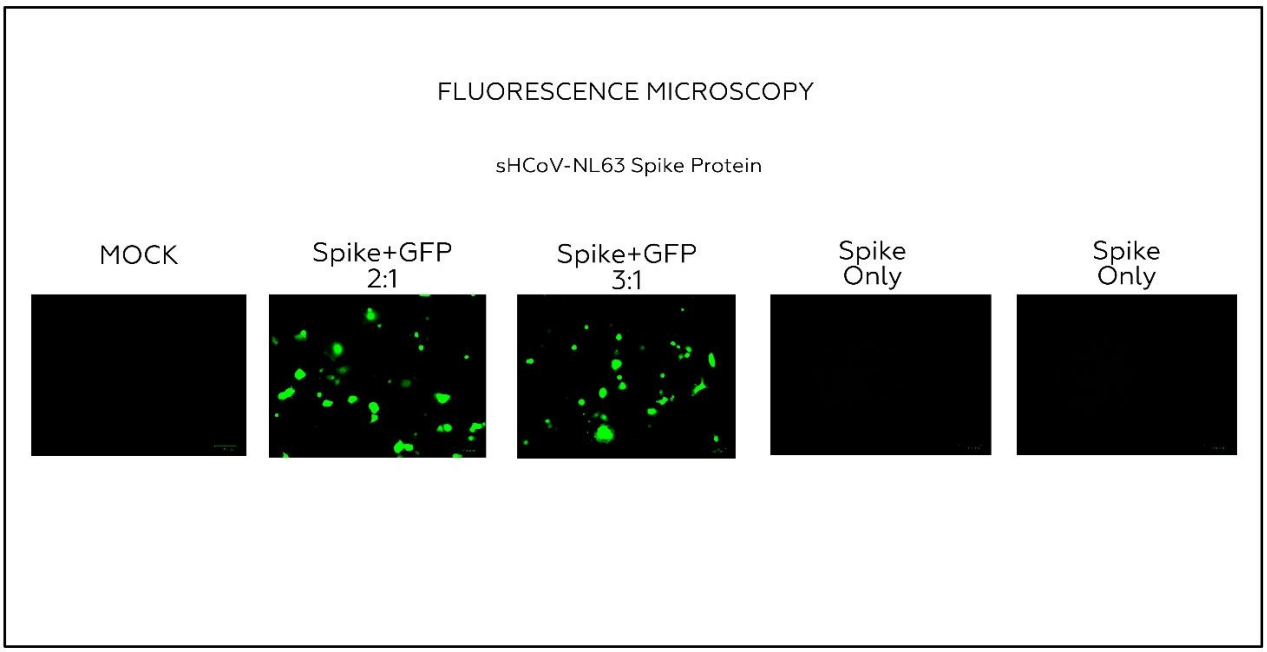

Figure 39. Fluorescence microscopy images of the redesigned monocistronic sHCoV-NL63 Spike construct containing a C-terminal FLAG tag, transfected in LLC-MK2 cells alone and co-transfected with GFP plasmid. LLC-MK2 cells were transfected with the redesigned sHCoV-NL63 Spike expression plasmid isolated, expecting no fluorescence, and co-transfected with the Spike expression plasmid and a GFP-expressing plasmid as a transfection control. Fluorescence microscopy was performed at 48 hours post-transfection to evaluate transfection efficiency based on GFP expression. The images were captured by the Zoe microscope. Data are from a single experiment with two replicates.

Following the confirmation of successful transfection under the experimental conditions and the absence of detectable cytotoxic effects associated with the redesigned monocistronic sHCoV-NL63 Spike construct shown in Figure 39, the next step was to evaluate whether Spike expression could be detected by flow cytometry.

Flow Cytometry analysis of the redesigned sHCoV-NL63 Spike expression construct

Flow cytometry was performed to confirm and quantify Spike protein expression and evaluate its potential effect on ACE2 surface expression. Both transfection conditions were analyzed: the Spike protein construct alone and co-transfected with a GFP-expressing construct.

Transfection efficiency was assessed by GFP detection in the co-transfected cells using the FITC channel; to assess intracellular FLAG-tagged viral protein expression, the Alexa 647 channel was used; and to determine surface ACE2 levels, the PE channel was used. The analyses were performed at 48 hours post-transfection. The cells were stained for surface ACE2, fixed, permeabilized, and intracellularly stained for FLAG, while GFP was assessed by exogenous expression.

As shown in Figure 40, flow cytometry analysis revealed a detectable FLAG signal in cells transfected with the redesigned Spike protein construct. As observed in HEK293T+ACE2 cells, the presence of a FLAG-positive population indicates that relocation of the epitope to the C-terminus improved Spike protein detection by antibody recognition. However, this experiment cannot distinguish whether the improved detection resulted from increased epitope accessibility, protein stability, altered folding, increased protein abundance, or another feature of the redesigned expression system.

The flow cytometry results supported successful expression of the redesigned sHCoV-NL63 Spike protein. Spike protein expression was detected in approximately 13.4% of the cells transfected with the Spike construct alone, a similar percentage to that observed with the FLAG-A2 control construct (15%). In the co-transfected cells, a small reduction in the percentage of FLAG-positive cells was observed, reaching 12.6%, while GFP expression was detected in 12.2% of the cells under the experimental conditions.

ACE2 receptor detection showed considerably limited signal intensity, which may be attributed to the use of a new antibody batch with reduced detection efficiency. Despite the lower overall signal, a difference in the percentage of ACE2-positive cells was observed between mock-stained cells and cells expressing the Spike protein, increasing from 2.7% to 4.1%, suggesting a potential difference in ACE2 surface detection following Spike protein expression. Interestingly, in contrast to the pattern observed in HEK293T+ACE2 cells, this difference was not maintained in cells co-transfected

with the GFP-expressing plasmid, which presented ACE2 surface levels similar to those of the mock cells.

Overall, these results should be interpreted with caution. The experiment was performed using a different antibody batch that resulted in weaker ACE2 receptor detection, and only a small percentage of cells were identified as ACE2 positive. In this experiment, only the Spike-alone condition presented a possible difference in ACE2 surface detection, which was not maintained in the Spike + GFP co-transfection condition. This result differed from that observed in HEK293T+ACE2 cells, where both Spike-alone and Spike + GFP conditions showed a similar increase in the percentage of ACE2-positive cells. Considering the low proportion of ACE2-positive cells detected in this LLC-MK2 experiment and the reduced antibody detection efficiency, the apparent difference observed following Spike transfection may reflect technical variability rather than a biological modulation of ACE2 surface expression. This experiment was performed once with two replicates and presented the technical limitations described above. Therefore, to allow a more reliable interpretation of these results, the experiment should be repeated using an antibody with improved detection efficiency.

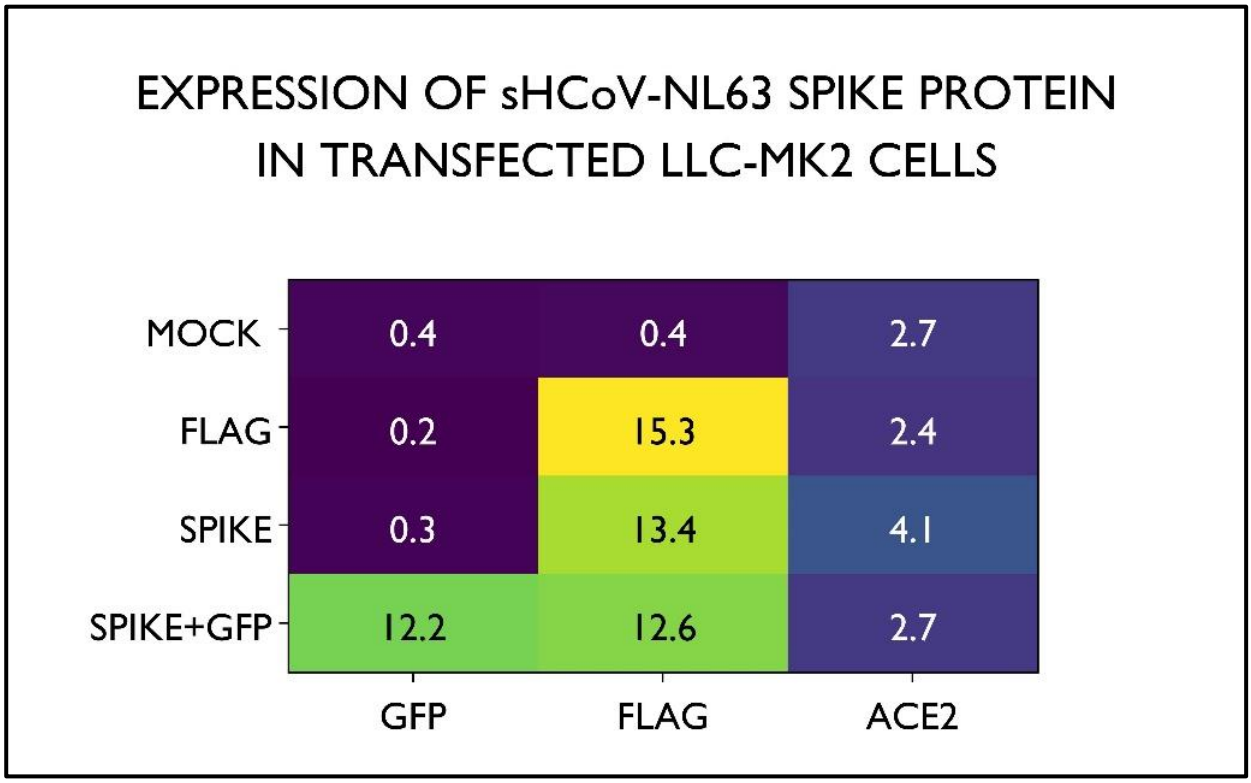

Figure 40. Flow cytometry analysis of the redesigned sHCoV-NL63 Spike construct expression in LLC-MK2 cells. Cells were transfected with the C-terminal FLAG-tagged sHCoV-NL63 Spike construct alone or co-transfected with a GFP-expressing plasmid as a transfection control. At 48 hours post-transfection, cells were analyzed by flow cytometry to evaluate GFP expression as an indicator of transfection efficiency by the FITC channel, FLAG expression as a measure of Spike protein expression by the Alexa647 channel, and ACE2 surface expression to assess potential receptor modulation by the PE channel. The heatmap represents the percentage of positive cells for each analyzed marker. Data are from a single experiment with two replicates.

In addition to the percentage of ACE2-positive cells, the ACE2 geometric mean fluorescence intensity (gMFI) was quantified among ACE2-positive cells.

Quantification of ACE2 receptor expression (%) and geometric mean fluorescence intensity (gMFI) for redesigned sHCoV-NL63 Spike construct

As shown in Figure 41, quantification of ACE2 geometric mean fluorescence intensity (gMFI) revealed increased ACE2-associated fluorescence in cells expressing the redesigned Spike construct compared with the control condition. However, this increase was observed only in the Spike-alone condition and was not reproduced in the Spike + GFP co-transfection condition.

Statistical analysis using one-way ANOVA demonstrated a significant difference among experimental groups ($p = 0.0006$; significance threshold, $p < 0.05$). Tukey's multiple-comparisons test confirmed a significant difference between mock-stained cells and Spike-expressing cells ($p = 0.0007$). In contrast, no significant difference was observed between mock-stained cells and cells co-expressing Spike and GFP ($p = 0.9667$). The statistical analyses are summarized in Table 2 (Appendices).

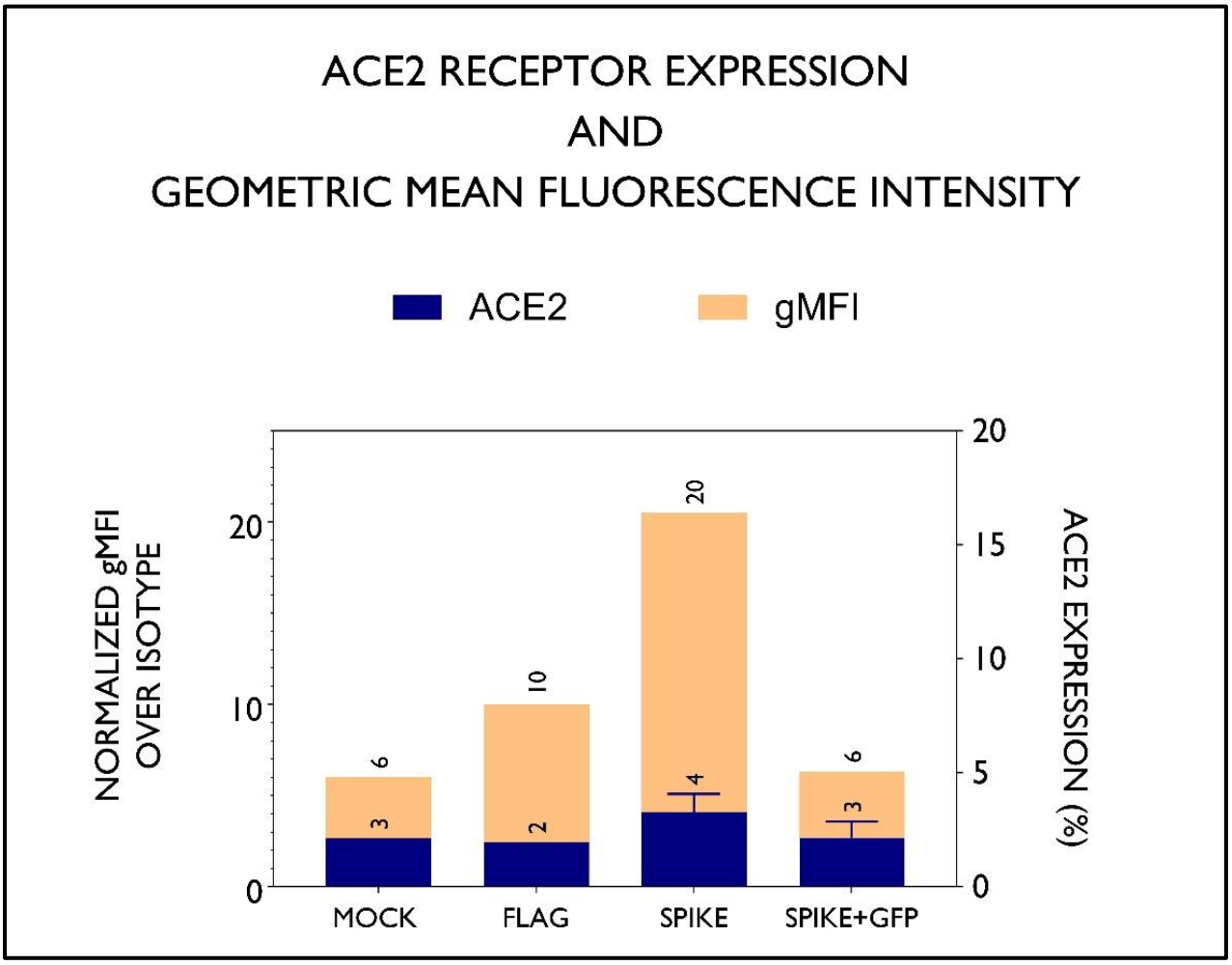

Figure 41. Quantification of ACE2 surface expression (%) and ACE2 geometric mean fluorescence intensity (gMFI) of the redesigned sHCoV-NL63 Spike construct expression in LLC-MK2 cells. Quantification of ACE2 percentage and gMFI following Spike expression. Values were normalized against the corresponding isotype control. Statistical analysis was performed using one-way ANOVA followed by Tukey's multiple comparisons test, as represented in table 2 (Appendices). Data are from a single experiment.

Due to the inconsistent ACE2 modulation observed between cells transfected with the sHCoV-NL63 Spike construct alone and cells co-transfected with the Spike and GFP-expressing plasmids, combined with the overall low ACE2 signal intensity that limited the analysis to a small number of ACE2-positive cells, this observation was considered insufficient to support a relevant effect.

Caution is required when comparing the HEK293T+ACE2 and LLC-MK2 results. Based on the HEK293T+ACE2 flow cytometry data (Figure 31), similar effects on ACE2 receptor expression might be expected following transfection with the Spike construct alone or co-transfection with the GFP reporter plasmid. However, this pattern was not reproduced in LLC-MK2 cells. Interpretation of these data is limited by reduced ACE2 antibody detection and the small positive cell population, which may have introduced substantial variability into the analysis and reduced the reliability of the observed difference. Therefore, these observations should not be considered conclusive evidence of Spike-mediated ACE2 receptor modulation.

Therefore, we considered that none of the isolated viral proteins tested demonstrated consistent and significant modulation of ACE2 surface receptor expression under the experimental conditions evaluated.

To further validate the expression of the redesigned sHCoV-NL63 Spike construct, western blot analysis was performed to determine whether the FLAG signal detected by flow cytometry corresponded to detectable Spike protein expression.

Western Blot analysis of the redesigned sHCoV-NL63 Spike construct

As shown in Figure 42, beta-tubulin detection supported comparable protein loading across all experimental conditions. However, detection of the FLAG-tagged Spike protein by western blot was not achieved under the evaluated conditions. In contrast to the results obtained in HEK293T+ACE2 cells, no diffuse or smearing signal was observed. The absence of a detectable FLAG signal may be associated with technical limitations such as extensive glycosylation, potential instability during sample preparation, aggregation or altered migration during electrophoresis. Therefore, western blot analysis was insufficient to confirm Spike protein expression in LLC-MK2 cells.

Nevertheless, when considered together with the positive FLAG staining detected by flow cytometry in Figure 40 and the subsequent dot blot analysis in Figure 43, these findings support

successful expression of the Spike construct while highlighting the technical challenges associated with its detection by western blot. Further optimization of protein extraction and electrophoresis conditions will be necessary to achieve a more robust and specific validation of Spike expression.

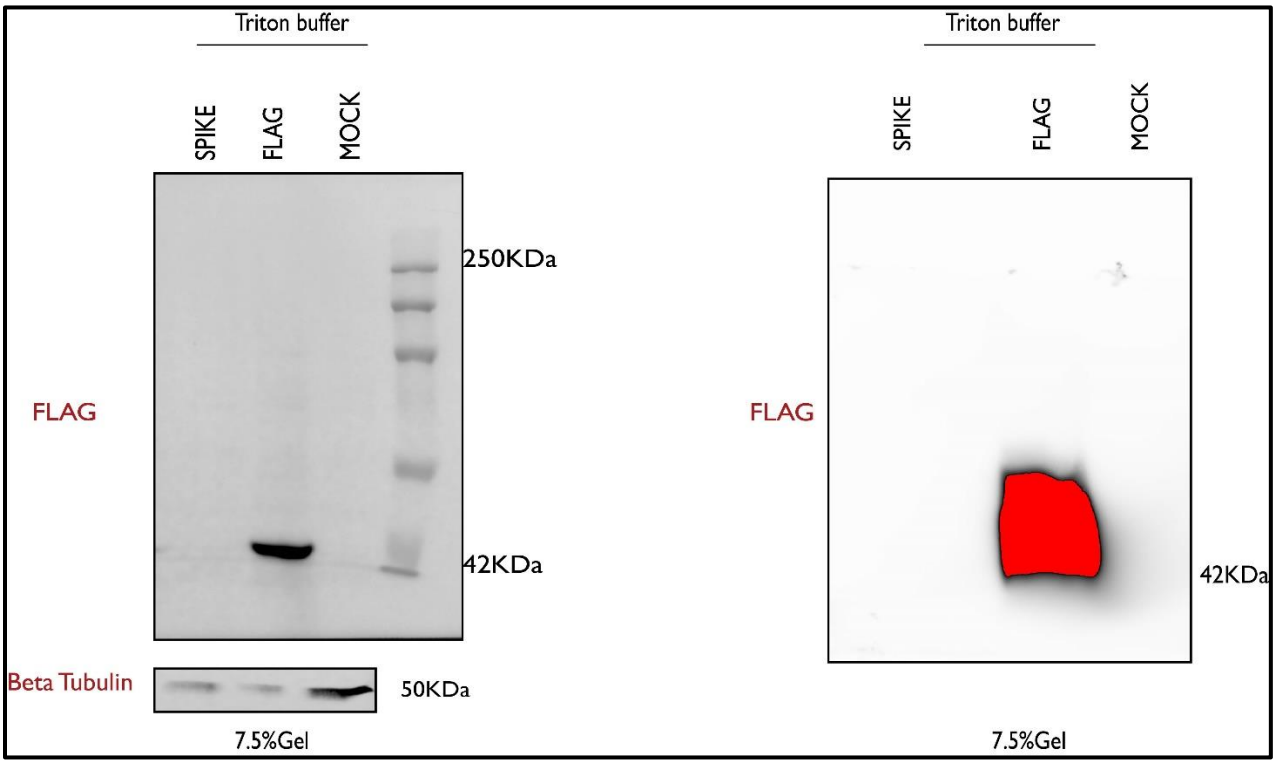

Figure 42. Western blot analysis of transfected LLC-MK2 cells with the redesigned sHCoV-NL63 Spike construct using anti-FLAG antibody. Cells were transfected with the redesigned sHCoV-NL63 Spike construct or the FLAG-A2 control plasmid. The cells were lysed in Triton Buffer + Protease inhibitor and analyzed by western blot using anti-FLAG antibody. β-Tubulin was used as a loading control to confirm comparable protein loading among samples. The FLAG control was detected, showing efficient protein extraction and transfer. However, no FLAG signal was detected for Spike protein under the experimental conditions.

Following the challenges encountered during western blot analysis for the detection of FLAG-tagged viral proteins, dot blot analysis was performed as an alternative approach to further evaluate protein expression. Unlike western blot, dot blot does not require protein separation by electrophoresis, allowing direct detection of the FLAG epitope and reducing potential limitations

associated with protein migration, aggregation, and poor resolution of high molecular weight proteins.

This approach was used to complement the flow cytometry and western blot results and to determine whether the FLAG-tagged sHCoV-NL63 and sHCoV-229E viral protein constructs were detectable in transfected LLC-MK2 cells.

Dot Blot analysis

As illustrated in Figure 43, dot blot analysis performed on a nitrocellulose membrane supported the expression of FLAG-tagged sHCoV-NL63 and sHCoV-229E proteins in transfected LLC-MK2 cells. FLAG was detected for all tested protein constructs at different and considerably lower intensities.

Overall, dot blot analysis provided complementary evidence supporting the expression of the FLAG-tagged viral proteins in LLC-MK2 cells.

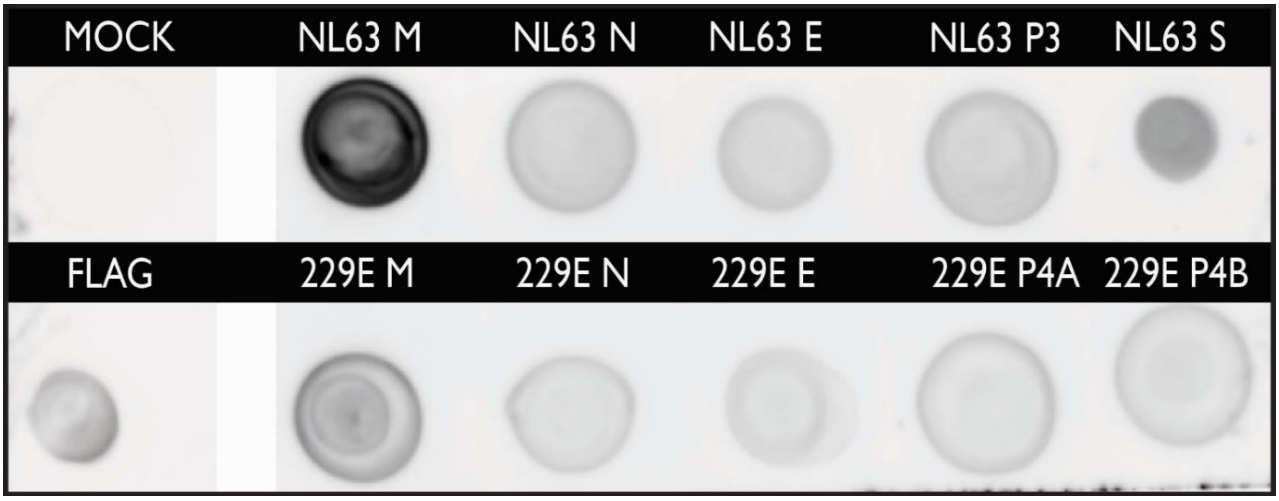

Figure 43. Dot blot validation of FLAG-tagged viral protein expression in transfected LLC-MK2 cells. Cell lysates from LLC-MK2 cells transfected with individual sHCoV-NL63 and sHCoV-229E viral protein constructs were analyzed by dot blot using an anti-FLAG antibody to confirm the expression of FLAG-tagged proteins. MOCK- non transfected cells; FLAG CTRL-peFLAG-A2; NL63 M – NL63 Membrane; NL63 N – NL63 Nucleocapsid; NL63 E – NL63 Envelope; NL63 P3- NL63 Protein 3; NL63 S – redesigned NL63 Spike construct; 229E M – 229E Membrane; 229E N – 229E Nucleocapsid; 229E E – 229E Envelope; 229E P4A – 229E Protein 4A; 229E P4B – 229E Protein 4 B; 229E S – 229E Spike. Data are from a single experiment using 10 µL of lysate per sample.

In conclusion, these findings demonstrate that the transient expression system successfully generated detectable expression of the majority of the sHCoV-NL63 and sHCoV-229E viral proteins in both HEK293T+ACE2 and LLC-MK2 cells, enabling assessment of their potential effects on ACE2 surface expression. Despite differences in transfection efficiency and protein detection among constructs and between cellular models, none of the successfully evaluated individual sHCoV-NL63 proteins consistently and significantly induced an increase in ACE2 surface expression.

The redesigned sHCoV-NL63 Spike construct provided an additional observation that requires further investigation. Although Spike expression did not significantly alter ACE2 gMFI in HEK293T+ACE2 cells, a statistically significant increase in ACE2 gMFI was detected in LLC-MK2 cells expressing the redesigned Spike construct. However, this effect was not reproduced in the Spike-plus-GFP condition and was observed in an experiment in which ACE2 antibody detection efficiency

was reduced. Therefore, while this result identifies Spike as a candidate that may deserve further investigation, the current data are insufficient to conclude that Spike alone is responsible for ACE2 upregulation.

In contrast to the transient-expression experiments, infection with the complete sHCoV-NL63 virus reproduced the dynamic pattern of ACE2 modulation previously reported in the literature, characterized by an increase in ACE2 surface expression during the early stages of infection followed by progressive downregulation as infection proceeded. The mechanism responsible for the early increase remains unresolved. However, the difference between the phenotype observed during productive infection and that obtained following isolated viral protein expression suggests that coordinated events associated with productive viral infection or effect of nsps and/or viral proteases activity may be required to ACE2 receptor modulation.

Together, these findings indicate that none of the individual viral proteins successfully evaluated in this study was sufficient to consistently reproduce the ACE2 upregulation observed during sHCoV-NL63 infection. Importantly, this conclusion cannot be extended to the complete viral proteome, as the non-structural proteins were not evaluated. Therefore, the infection-associated phenotype may depend on non-structural proteins, viral protease activity, interactions among multiple viral proteins, replication-associated processes, host antiviral responses, or a combination of these factors.

Overall, although this study did not identify a single viral protein responsible for ACE2 modulation, the findings suggest that the early increase in ACE2 surface expression may involve mechanisms associated with the broader context of productive sHCoV-NL63 infection. These findings provide a basis for future studies investigating the viral and host factors involved in this modulation and may contribute to a better understanding of how sHCoV-NL63 infection influences its cellular receptor.

Conclusion

The present study investigated whether individual proteins from sHCoV-NL63 can modulate cell-surface ACE2 receptor expression. To address this question, polycistronic expression vectors encoding individual viral proteins were generated and sequence-verified to confirm the expected sequences, followed by their expression and characterization in HEK293T+ACE2 and LLC-MK2 cells. Overall, the transient expression system generated detectable expression of the majority of the evaluated sHCoV-NL63 and sHCoV-229E viral protein constructs, allowing their potential effects on ACE2 surface expression to be investigated. However, none of the successfully evaluated individual sHCoV-NL63 proteins were sufficient to consistently induce an ACE2 upregulation. Therefore, under the experimental conditions evaluated in this study, the isolated expression of the structural and accessory proteins tested was not sufficient to reproduce the infection-associated ACE2 phenotype. Importantly, this conclusion should not be extended to all sHCoV-NL63 proteins, since ORF1a and ORF1b proteins could not be evaluated.

Optimization of the transfection and detection protocols in HEK293T+ACE2 cells provided an experimental system for simultaneously evaluating GFP fluorescence, intracellular FLAG-tagged viral protein detection, and cell-surface ACE2 receptor expression. However, an important observation throughout these experiments was that the different constructs did not produce equivalent GFP and FLAG levels. Most constructs exhibited a higher percentage of FLAG-positive than GFP-positive cells. This pattern was particularly evident for sHCoV-NL63 Membrane, Nucleocapsid, Envelope, and Protein 3 and for several sHCoV-229E constructs. Because the polycistronic vectors generate a bicistronic transcript in which translation of the FLAG-tagged viral protein is cap-dependent, whereas GFP translation is mediated by an IRES, the generally lower GFP signal is compatible with differences in translational efficiency between these two mechanisms. Thus, GFP was useful as an indicator of plasmid delivery and transcription but could not be interpreted as a direct quantitative measurement of viral protein abundance.

Nevertheless, some constructs showed the opposite profile, with relatively higher GFP detection but substantially lower FLAG detection. This was particularly evident for the polycistronic sHCoV-NL63 Spike construct, for which GFP was detected while FLAG detection was almost absent. Since GFP detection indicated successful plasmid delivery and synthesis of the bicistronic transcript, the low FLAG signal could not be explained simply by unsuccessful transfection. Instead, this discrepancy indicated a construct- or protein-specific limitation occurring post-plasmid delivery, potentially involving inefficient translation, protein stability, degradation, folding, or accessibility of the FLAG epitope. These mechanisms were not directly investigated in the present study and therefore cannot be distinguished based on the available data. The variation observed among constructs also emphasizes that reporter expression and viral protein detection should not be considered equivalent measurements of protein expression in our experiment.

Another technical factor influencing GFP quantification was the fixation and permeabilization required for intracellular FLAG staining. GFP fluorescence was considerably lower in fixed and permeabilized samples than in the corresponding non-fixed samples evaluated during optimization. This limitation is particularly relevant when interpreting differences between GFP and FLAG percentages and reinforces the importance of considering the three measurements (GFP, FLAG, and ACE2) as related but experimentally distinct parameters.

The inability to efficiently evaluate ORF1a and ORF1b represents an important limitation of this study. Both constructs showed no GFP detection together with high cytotoxicity, resulting in the recovery of a small and unhealthy cell population that was considered unsuitable for reliable analysis. The large size and complexity of these constructs likely contributed to the difficulty of establishing a suitable transient-expression system. This limitation is particularly important in relation to the central hypothesis because ORF1a and ORF1b encode 16 non-structural proteins involved in viral replication, polyprotein processing, replication-transcription complex formation, and modulation of cellular antiviral pathways. Studies of SARS-CoV-2 have demonstrated that

several nsps antagonize innate immune signalling by targeting key molecules involved in interferon induction and RNA sensing, including RIG-I, MDA5, MAVS, and IRF3. Consequently, failure to evaluate these proteins represents one of the main limitations of this work. Therefore, the present study cannot exclude the possibility that one or more non-structural proteins contribute to ACE2 modulation, either directly or indirectly.

Flow cytometry analysis of ACE2 further demonstrated the importance of distinguishing the percentage of ACE2-positive cells from receptor abundance within the positive population. Across the successfully evaluated polycistronic constructs, the percentage of ACE2-positive cells remained relatively stable, with only modest construct-dependent variation. Analysis of ACE2 gMFI provided an additional measurement and increased sensitivity of receptor-associated fluorescence among ACE2-positive cells and revealed some variation between experimental conditions. In HEK293T+ACE2 cells, sHCoV-NL63 proteins showed a modest tendency toward reduced ACE2 gMFI, whereas sHCoV-229E proteins showed a tendency toward increased gMFI; however, these differences were small and did not reach statistical significance (one-way ANOVA, $p = 0.8688$). Therefore, the combined analysis of ACE2-positive percentage and gMFI supports the conclusion that none of the successfully evaluated polycistronic sHCoV-NL63 constructs produced a consistent and statistically significant change in surface ACE2 under the experimental conditions tested.

Characterization of the viral proteins by western blot provided an additional level of validation, strengthening the flow cytometry findings, but also revealed important technical limitations. Conventional sample preparation using SDS-containing loading buffer and heat denaturation failed to consistently detect FLAG-tagged viral proteins despite evidence of successful transfection and FLAG detection by flow cytometry. Multiple extraction and electrophoresis conditions were therefore evaluated. Based on previous studies describing detergent- and heat-induced aggregation of membrane proteins, we hypothesize that sample preparation promoted protein aggregation, thereby impeding FLAG detection (Lee et al., 2005; Sagné et al., 1996). The best

condition for FLAG detection was obtained using non-SDS lysis buffer, non-SDS loading buffer, and non-heated samples followed by SDS-PAGE. Native-PAGE was also tested and produced more distinct FLAG signals but inconsistent protein migration and was consequently unsuitable for reliable molecular-weight comparison. Under the optimized conditions using SDS-PAGE, bands corresponding to the expected molecular weights were detected for several constructs, although additional bands were also observed, potentially reflecting the native conformation of the protein and SDS-aggregated forms generated from contact with SDS during SDS-PAGE electrophoresis.

An additional limitation of the western blot experiments was that total protein concentration was not quantified prior to gel loading. Because viral protein expression was limited for some constructs and, additionally, due to the aggregation factor encountered, the experimental priority was to maximize the amount of available lysate loaded onto the gel, characterizing protein presence and molecular weight rather than normalizing each sample to an identical total protein concentration. For this purpose, a fixed lysate volume was loaded, and β-tubulin was used as a loading control to assess comparability between samples. This approach allowed the limited material available from the transfected cells to be used for FLAG detection, but it reduced the suitability of these blots for quantitative comparison. Therefore, the western blot results should primarily be interpreted as qualitative evidence supporting protein detection at or near the expected molecular weight rather than as a quantitative comparison of expression levels.

The polycistronic sHCoV-NL63 Spike construct represented another technical limitation. Despite detectable GFP expression, FLAG detection was almost absent, suggesting that plasmid delivery and mRNA transcription were occurring; however, a limitation potentially related to protein folding, stability, or epitope accessibility may have affected FLAG detection. The Spike coding sequence was therefore redesigned in a monocistronic pcDNA3.1 vector, with the FLAG epitope repositioned from the N-terminus to the C-terminus. This modification substantially improved FLAG detection by flow cytometry, with approximately 30% FLAG-positive HEK293T+ACE2 cells and 13.4% FLAG-positive

LLC-MK2 cells following transfection with the redesigned Spike construct. This finding supports the interpretation that the configuration of the construct affected Spike detection. However, the experiment cannot distinguish whether the improvement resulted specifically from increased FLAG accessibility, improved protein stability, improved folding, or the change from a polycistronic to a monocistronic expression system.

Despite the improved detection of the redesigned Spike construct by flow cytometry, Spike remained difficult to characterize by western blot. In HEK293T+ACE2 cells, FLAG immunoblotting produced diffuse and poorly resolved signals without a clearly defined band at the expected Spike molecular weight, whereas in LLC-MK2 cells, no detectable FLAG band was obtained under the tested conditions. In contrast, FLAG-positive cells were detected by flow cytometry and dot blot. These differences illustrate that failure to obtain a well-resolved western blot band cannot, by itself, be interpreted as the absence of protein expression. Instead, the combined findings suggest that Spike detection was strongly influenced by the analytical method and sample-processing conditions.

The redesigned Spike construct also produced one inconsistent observation regarding ACE2 modulation. In HEK293T+ACE2 cells, the percentage of ACE2-positive cells increased from 43.7% in mock cells to 51.4% following Spike transfection and 52.7% following Spike + GFP co-transfection. However, this increase in percentage was not accompanied by a significant increase in ACE2 gMFI, with the overall comparison remaining non-significant ($p = 0.5954$). Moreover, this experiment was performed only once and used an antibody batch associated with weaker ACE2 detection. Therefore, these data were insufficient to conclude that Spike significantly increased ACE2 surface abundance in HEK293T+ACE2 cells.

A different result was obtained when the redesigned Spike construct was evaluated in LLC-MK2 cells. The percentage of ACE2-positive cells increased from 2.7% in mock cells to 4.1% following Spike transfection but this increase was not observed following Spike + GFP co-transfection, in

which the percentage of ACE2-positive cells remained at 2.7%, comparable to the mock condition. Analysis of ACE2 gMFI showed a significant increase in cells transfected with Spike alone compared with mock cells ($p = 0.0007$). However, this effect was not reproduced in cells co-transfected with Spike and GFP ($p = 0.9667$), despite both conditions containing the same Spike expression construct. Furthermore, ACE2 detection in this experiment was low, limiting the ACE2 and ACE2 gMFI analyses to a relatively small ACE2-positive population, and the experiment was performed only once. The lack of agreement between the Spike-only and Spike + GFP conditions is particularly important because a true and reproducible Spike-dependent effect would be expected to show a consistent direction across conditions in which Spike is expressed. Although a significant result was obtained with Spike alone, this experiment was performed once with two replicates and presented the technical limitations described above. Therefore, to allow a more reliable interpretation of these results, the experiment should be repeated using an antibody with improved detection efficiency.

It is also important to emphasize the cellular context when investigating host-virus interactions. Both cell lines used are permissive to sHCoV-NL63 infection. According to the literature, LLC-MK2 is the most commonly used cell line for NL63 infection studies. However, a few other cell lines are also susceptible to NL63 infection, such as Caco-2 and Vero E6. One study also tested modified HEK293T+ACE2 and A549+ACE2 cells, both of which showed efficient infection with comparable virus titers. In general, these cell lines can provide a relevant system for intracellular environment screening, virus propagation, and isolation, but they do not substitute for the physiological relevance of primary cells (Lednicky et al., 2013; Herzog et al., 2008; Milewska et al., 2014).

Both cell systems provided distinct but complementary experimental advantages. HEK293T+ACE2 cells exhibited considerably higher transfection efficiency and were therefore valuable for screening individual viral constructs. However, because these cells are engineered to stably express ACE2, they may have reduced biological sensitivity for detecting changes in ACE2 expression. To

partially address this limitation, ACE2 geometric mean fluorescence intensity (gMFI) was analyzed in addition to the percentage of ACE2-positive cells, allowing more subtle changes in receptor abundance within the ACE2-positive population to be evaluated. This model was further complemented by the use of LLC-MK2 cells, which do not rely on stable ectopic ACE2 expression and provided a system in which the effects of transient viral protein expression could be compared with those observed during productive sHCoV-NL63 infection. Transfection efficiency and overall viral protein detection were lower in LLC-MK2 cells, although expression remained sufficient for the analysis of most constructs. Alternative transfection approaches, such as electroporation, could potentially improve transfection efficiency in this cell line; however, due to resource limitations, lipid-based transfection was maintained because it provided sufficient expression for the analyses performed in this study. Consequently, differences observed between the two cell lines should not necessarily be interpreted as contradictory biological effects, as transfection efficiency, baseline ACE2 abundance, protein processing, and other host-cell-specific characteristics may influence the measured phenotype. Importantly, neither model fully reproduces the physiological environment of primary human respiratory epithelial cells. Therefore, future validation in more physiologically relevant systems would strengthen the biological interpretation of ACE2 regulation during sHCoV-NL63 infection.

While isolated expression of the successfully evaluated viral proteins did not significantly induce the ACE2 upregulation, sHCoV-NL63 infection produced a dynamic change in surface ACE2 receptor over time. In the infection kinetics experiment, ACE2 surface expression increased during the early stages of infection and subsequently declined as infection progressed, reproducing the general temporal pattern previously reported for sHCoV-NL63. The early increase was detectable before substantial cell loss, whereas the later decline occurred concomitantly with increasing CPE and loss of viable cells.

Although these observations initially raised the possibility that the apparent reduction in ACE2 could be influenced by cell loss, preliminary data from our laboratory suggest that this decline is not attributable to the loss of infected cells. In these experiments, sHCoV-NL63-infected cells were stained for the viral N protein together with a live/dead viability marker, and ACE2 expression was evaluated using both N protein-positive live cells and N protein-positive single cells as gating strategies. Both analyses showed reduced surface ACE2 in infected cells compared with mock non-infected cells, supporting the possibility of an active reduction in ACE2 surface expression during infection (Figure 14 – Appendices). Nevertheless, because these preliminary observations were not part of the experiments presented in this study, the mechanism underlying the later decrease in ACE2 cannot be conclusively determined. Biological processes including altered receptor trafficking, internalization, shedding, or degradation could contribute to the reduction in surface ACE2, but these mechanisms were not directly evaluated in this study.

Taken together, these findings do not support the identification of a single successfully evaluated structural or accessory sHCoV-NL63 protein as sufficient to induce significant ACE2 modulation. However, they also do not exclude a contribution from individual viral proteins that could not be adequately evaluated, particularly proteins derived from ORF1a and ORF1b. During productive infection, viral RNA synthesis, proteolytic processing of viral polyproteins, formation of replication-transcription complexes and replication organelles, simultaneous expression and interaction of viral proteins, cellular remodelling, and activation or antagonism of host antiviral responses occur within the same cellular environment. These processes are not reproduced by transient expression of a single structural or accessory protein and remain possible contributors to ACE2 modulation.

The present study narrows the original hypothesis by showing that isolated expression of the successfully evaluated sHCoV-NL63 structural and accessory proteins was not sufficient to consistently reproduce the ACE2 phenotype observed during infection. The mechanism responsible

for the early increase in ACE2 remains unresolved and represents an important direction for future investigation.

Future Directions

Since the isolated viral proteins successfully evaluated in this study were not sufficient to induce significant ACE2 modulation, future studies should investigate viral components and infection-associated processes that were not represented.

One important direction would be to investigate the contribution of viral proteases, particularly the papain-like protease (PLpro) and the main protease (3CLpro/Mpro), encoded within ORF1a and ORF1b. Beyond their essential roles in viral polyprotein processing, coronavirus proteases can also interfere with host signalling pathways involved in innate antiviral responses. In particular, PLpro possesses deubiquitinating and deISGylating activities that can interfere with proteins involved in antiviral signalling. Determining whether the expression or enzymatic activity of these proteases directly or indirectly influences ACE2 surface expression may provide important mechanistic insight into receptor regulation during sHCoV-NL63 infection. Evaluating these proteins individually, rather than attempting to express the complete ORF1a and ORF1b sequences, may also overcome the technical limitations encountered with the large constructs used in the present study. Investigating all 16 nsps individually could also provide insight.

Another important direction would be to investigate the possible indirect contribution of type I and type III interferon signalling to ACE2 modulation. Interferons induce a broad antiviral program and regulate the expression of numerous interferon-stimulated genes. In addition, interferon signalling has been associated with the induction of the truncated ACE2 isoform, dACE2, rather than necessarily increasing the expression of the full-length functional ACE2 receptor. Therefore, simultaneously evaluating interferon production, activation of downstream signalling pathways, expression of interferon-stimulated genes, and the different forms of ACE2 during sHCoV-NL63 infection could help determine whether the changes observed in ACE2 are directly induced by viral infection or are partially associated with the host antiviral response. This distinction may also help

clarify the difference observed in this study between changes in cell-surface ACE2 detected by flow cytometry and total ACE2-associated protein detected by western blot.

Future experiments should also consider the possibility that ACE2 modulation requires interactions among multiple viral proteins rather than the activity of one protein expressed in isolation. During productive infection, structural, accessory, and non-structural proteins are expressed within the same cellular environment and interact with each other while viral RNA replication, polyprotein processing, replication-transcription complex formation, and cellular membrane remodelling occur simultaneously. These conditions are not reproduced by transient expression of individual proteins. Therefore, co-expression experiments involving selected combinations of viral proteins could help determine whether cooperative protein-protein interactions contribute to ACE2 regulation.

The redesigned Spike construct should also be further investigated. Although the C-terminal FLAG configuration substantially improved Spike detection compared with the original polycistronic construct, the increase in ACE2 gMFI observed in LLC-MK2 cells was not reproduced in the Spike-plus-GFP condition and was obtained under conditions of reduced ACE2 antibody detection. Therefore, this observation should be independently replicated using standardized antibody batches. Additional confirmation of Spike expression would also strengthen the interpretation, given the difficulties encountered with its detection by western blot, the use of specific antibody against sHCoV-Spike could improve the detection efficiency and reliability.

Overall, future studies should prioritize the non-structural proteins that could not be evaluated in the present work, viral protease activity and polyprotein processing, interactions among simultaneously expressed viral proteins, and host antiviral signalling. A better understanding of these pathways may not only clarify fundamental aspects of coronavirus biology but also reveal potential therapeutic targets capable of modulating host susceptibility and limiting the consequences of respiratory viral co-infections.

Appendices

	HEK 293T+ACE2	P value	Significance	Method
	ALL SAMPLES	0.8688	NO	One-way ANOVA
sHCoV-NL63	MOCK VS MEMBRANE	0.9987	NO	Tukey's multiple comparisons test
	MOCK VS NUCLEOCAPSID	>0.9999	NO	Tukey's multiple comparisons test
	MOCK VS ENVELOPE	>0.9999	NO	Tukey's multiple comparisons test
	MOCK VS PROTEIN 3	>0.9999	NO	Tukey's multiple comparisons test
	ALL SAMPLES (SPIKE PROTEIN EXPERIMENT)	0.5954	NO	One-way ANOVA
	MOCK VS SPIKE	0.6815	NO	Tukey's multiple comparisons test
	MOCK VS SPIKE + GFP	0.9905	NO	Tukey's multiple comparisons test
sHCoV-229E	MOCK VS MEMBRANE	>0.9999	NO	Tukey's multiple comparisons test
	MOCK VS NUCLEOCAPSID	0.9993	NO	Tukey's multiple comparisons test
	MOCK VS ENVELOPE	0.9999	NO	Tukey's multiple comparisons test
	MOCK VS PROTEIN 4A	>0.9999	NO	Tukey's multiple comparisons test
	MOCK VS PROTEIN 4B	0.9997	NO	Tukey's multiple comparisons test
sHCoV-NL63 VS sHCoV-229E	MEMBRANE VS MEMBRANE CONTROL	0.9692	NO	Tukey's multiple comparisons test
	NUCLEOCAPSID VS NUCLEOCAPSID CONTROL	0.9967	NO	Tukey's multiple comparisons test
	ENVELOPE VS ENVELOPE CONTROL	0.9931	NO	Tukey's multiple comparisons test
	PROTEIN 3 VS PROTEIN 4A CONTROL	0.9997	NO	Tukey's multiple comparisons test
	PROTEIN 3 VS PROTEIN 4B CONTROL	>0.9999	NO	Tukey's multiple comparisons test

Table 1. Statistical analysis of ACE2-positive cells gMFI in transfected HEK293T+ACE2 cells. One-way ANOVA and Tukey's multiple comparisons test evaluating ACE2 geometric mean fluorescence intensity (gMFI) in HEK293T+ACE2 cells transfected with polycistronic viral protein and monocistronic spike protein constructs.

	LLC MK2	P value	Significance	Method
	ALL SAMPLES	0.6946	NO	One-way ANOVA
sHCoV-NL63	MOCK VS MEMBRANE	0.9905	NO	Tukey's multiple comparisons test
	MOCK VS NUCLEOCAPSID	0.9589	NO	Tukey's multiple comparisons test
	MOCK VS ENVELOPE	0.9687	NO	Tukey's multiple comparisons test
	MOCK VS PROTEIN 3	0.9408	NO	Tukey's multiple comparisons test
	ALL SAMPLES (SPIKE PROTEIN EXPERIMENT)	0.0006	YES	One-way ANOVA
	MOCK VS SPIKE	0.0007	YES	Tukey's multiple comparisons test
	MOCK VS SPIKE + GFP	0.9667	NO	Tukey's multiple comparisons test
sHCoV-229E	MOCK VS MEMBRANE	0.8573	NO	Tukey's multiple comparisons test
	MOCK VS NUCLEOCAPSID	0.7625	NO	Tukey's multiple comparisons test
	MOCK VS ENVELOPE	0.6583	NO	Tukey's multiple comparisons test
	MOCK VS PROTEIN 4A	0.8023	NO	Tukey's multiple comparisons test
	MOCK VS PROTEIN 4B	0.9524	NO	Tukey's multiple comparisons test
sHCoV-NL63 VS sHCoV-229E	MEMBRANE VS MEMBRANE CONTROL	0.9959	NO	Tukey's multiple comparisons test
	NUCLEOCAPSID VS NUCLEOCAPSID CONTROL	0.995	NO	Tukey's multiple comparisons test
	ENVELOPE VS ENVELOPE CONTROL	0.9692	NO	Tukey's multiple comparisons test
	PROTEIN 3 VS PROTEIN 4A CONTROL	0.999	NO	Tukey's multiple comparisons test
	PROTEIN 3 VS PROTEIN 4B CONTROL	>0.9999	NO	Tukey's multiple comparisons test

Table 2. Statistical analysis of ACE2-positive cells gMFI in transfected LLC-MK2 cells. One-way ANOVA and Tukey's multiple comparisons test evaluating ACE2 geometric mean fluorescence intensity (gMFI) in HEK293T+ACE2 cells transfected with polycistronic viral protein and monocistronic spike protein constructs.

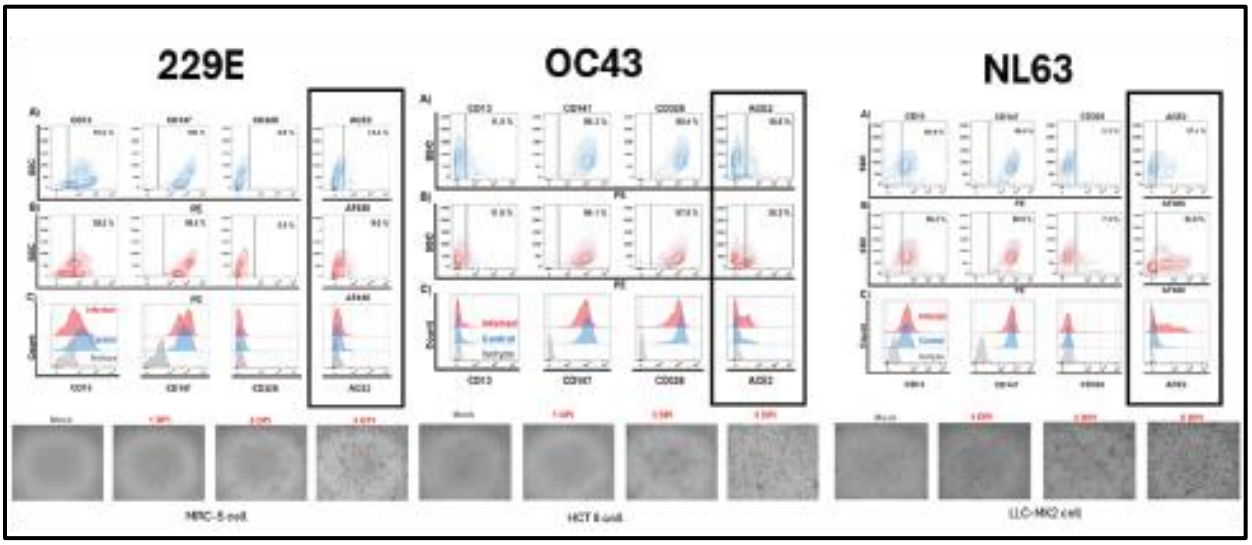

Figure 1. Differential Cytopathic Effects and ACE2 Receptor Modulation Induced by Human Coronaviruses 229E, OC43, and NL63 in Permissive Cells. (Adapted figures from Siragam et al., 2023).

One of our laboratory's previous studies revealed that sHCoV-229E, sHCoV-OC43, and sHCoV-NL63 were capable of exhibiting CPE in their respective cell lines. Notably, only sHCoV-NL63 and sHCoV-OC43 lead to an upregulation of the ACE2 receptor. These findings highlighted the differential effects of sHCoVs on receptor modulation and their potential implications for viral entry and co-infection.

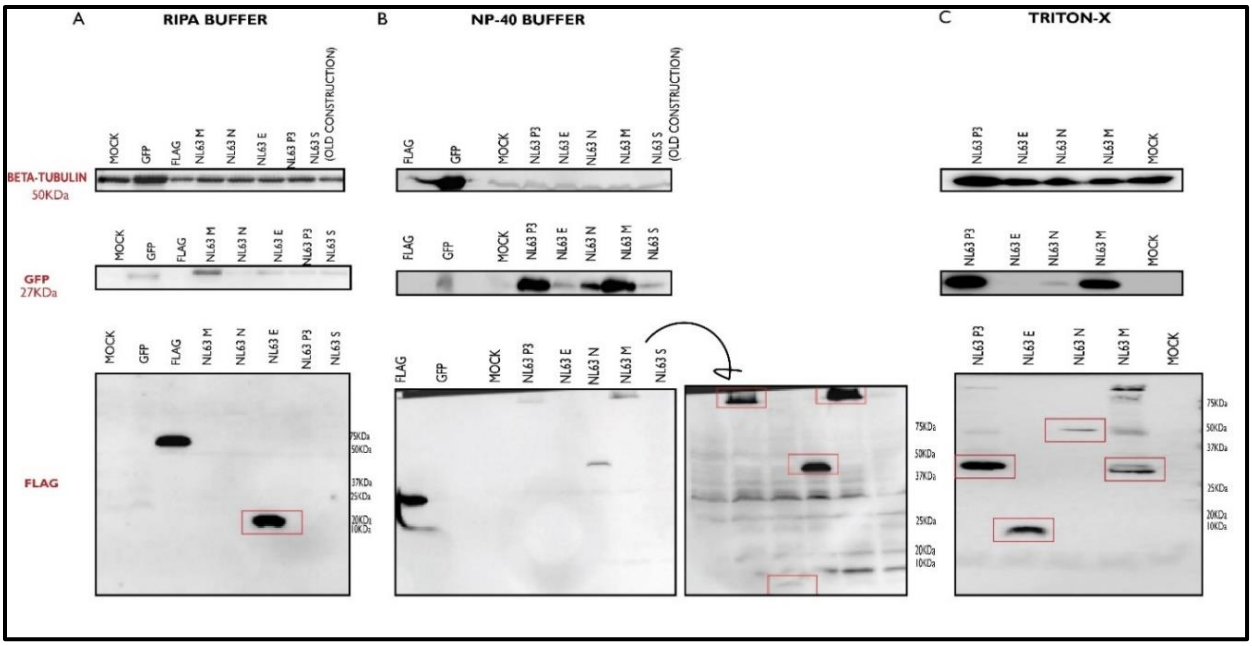

Figure 2. Western blot troubleshooting for FLAG-tagged viral protein detection in transfected HEK293T+ACE2 cells. HEK293T+ACE2 cells were transfected with control plasmids and individual sHCoV-NL63 viral protein constructs, and cell lysates were prepared using different lysis buffers to optimize protein recovery and FLAG detection. β-Tubulin was used as a loading control, GFP detection was used to support successful plasmid-associated expression, and FLAG immunodetection was used to evaluate the corresponding FLAG-tagged viral proteins. (A) Cells were lysed using RIPA buffer. (B) Cells were lysed using NP-40 buffer. (C) Cells were lysed using Triton-X buffer. Differences in FLAG detection and band resolution were observed among the tested extraction conditions. Red boxes indicate bands detected of the corresponding FLAG-tagged viral protein. The additional enlarged panel in B highlights FLAG bands that were more clearly visualized following image adjustment/increased image exposition.

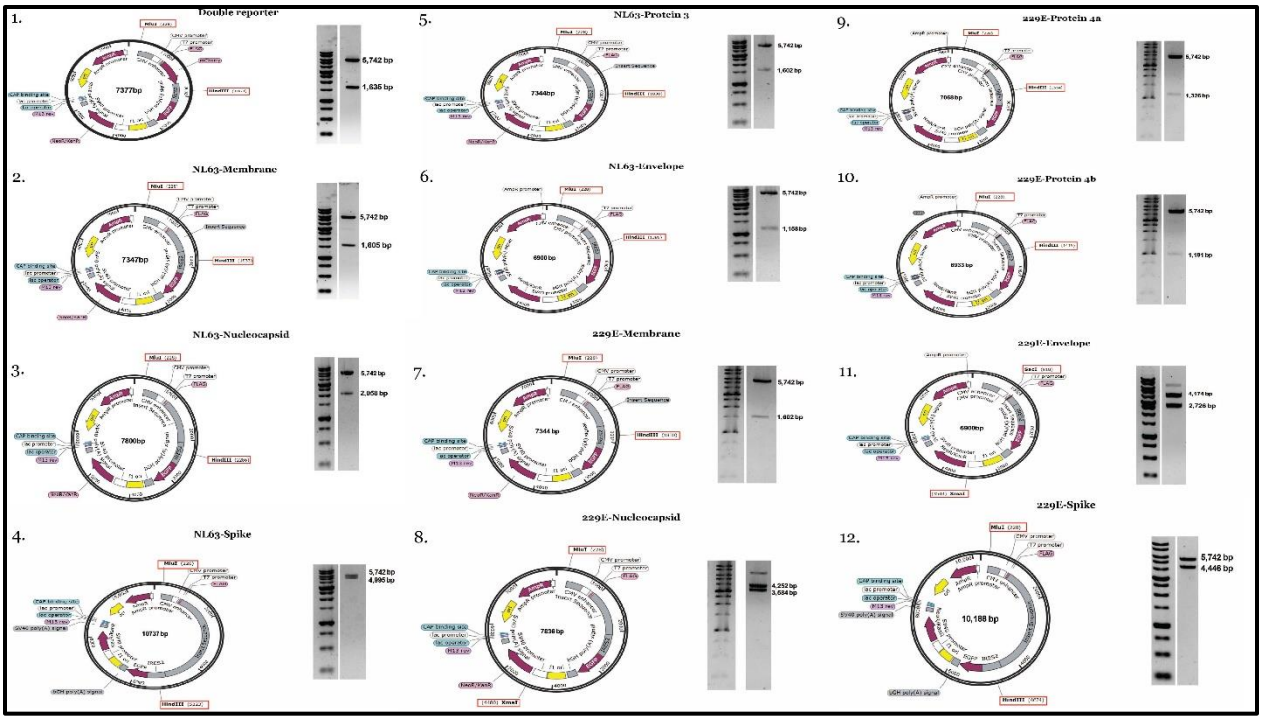

Figure 3. Restriction enzyme digestion analysis of the viral protein expression plasmids. Plasmid maps showing the restriction enzyme sites selected for construct validation and the corresponding agarose gel electrophoresis results following restriction digestion. MluI-HF and HindIII-HF were used for the digestion of the majority of the sHCoV-NL63 and sHCoV-229E structural and accessory protein plasmids. MluI-HF was used in combination with XmaI for 229E Nucleocapsid, whereas SacI-HF and XmaI were used for the 229E-Envelope construct. The resulting DNA fragments were separated by agarose gel electrophoresis, and the expected fragment sizes based on the plasmid maps are indicated next to the corresponding gel images. The constructs analyzed were: (1) double-reporter control plasmid; (2) sHCoV-NL63 Membrane; (3) sHCoV-NL63 Nucleocapsid; (4) sHCoV-NL63 Spike; (5) sHCoV-NL63 Protein 3; (6) sHCoV-NL63 Envelope; (7) sHCoV-229E Membrane; (8) sHCoV-229E Nucleocapsid; (9) sHCoV-229E Protein 4A; (10) sHCoV-229E Protein 4B; (11) sHCoV-229E Envelope; and (12) sHCoV-229E Spike. The observed digestion profiles were compared with the predicted fragment sizes for each construct to support confirmation of the expected plasmid organization.

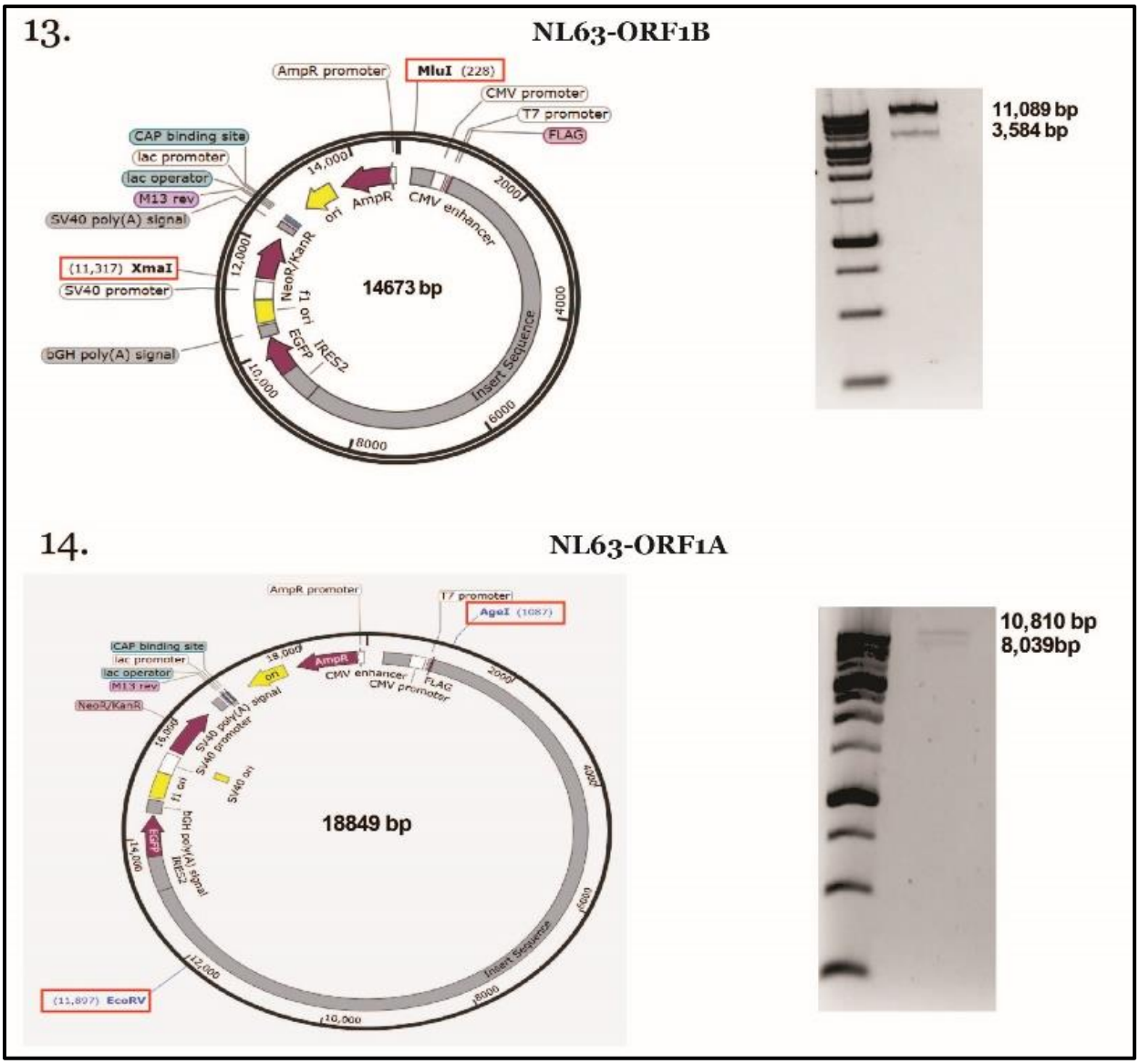

Figure 4. Restriction enzyme digestion analysis of the sHCoV-NL63 ORF1A and ORF1B expression plasmids. Plasmid maps showing the restriction enzyme sites selected for construct validation and the corresponding agarose gel electrophoresis results following restriction digestion. MluI-HF was used in combination with XmaI for the digestion of the sHCoV-NL63 ORF1B plasmid, whereas AgeI-HF and EcoRV-HF were used for the sHCoV-NL63 ORF1A construct. The resulting DNA fragments were separated by agarose gel electrophoresis, and the expected fragment sizes based on the plasmid maps are indicated next to the corresponding gel images. The constructs analyzed were: (13) sHCoV-NL63 ORF1B and (14) sHCoV-NL63 ORF1A. The observed digestion profiles were compared with the predicted fragment sizes for each construct to support confirmation of the expected plasmid organization.

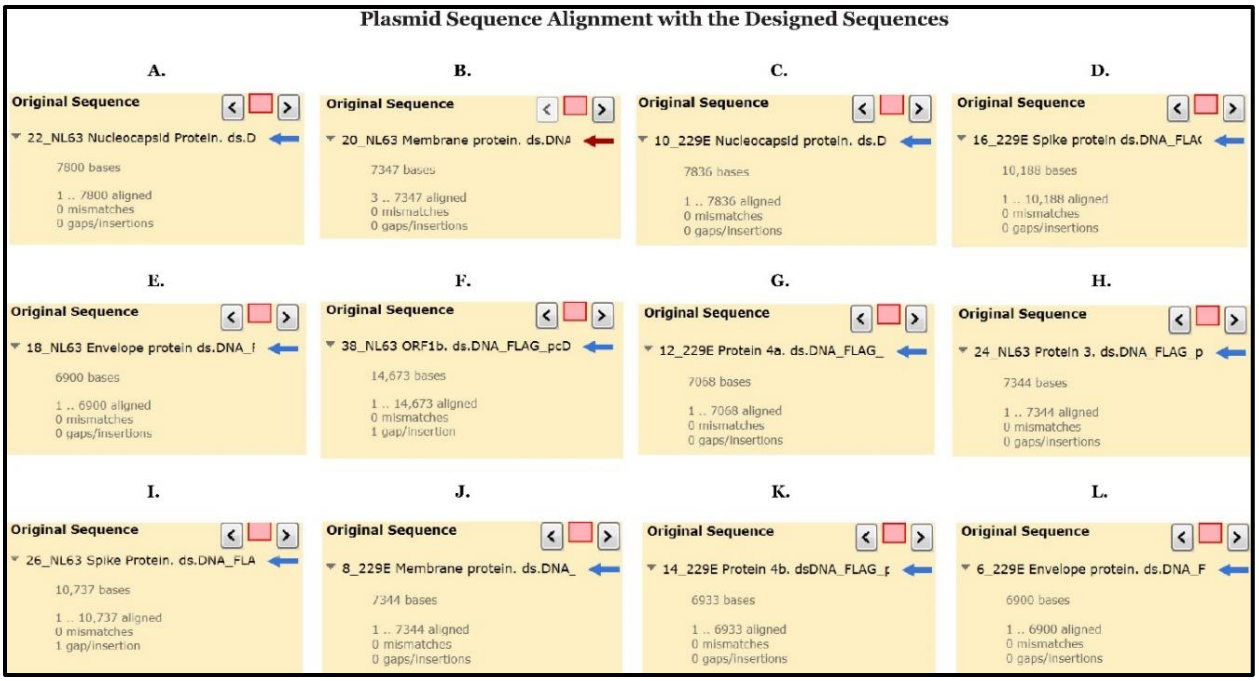

Figure 5. Plasmid sequencing alignment with the designed reference sequences. Summary of the reports from sequence alignments performed in SnapGene to validate the viral protein expression plasmids. Plasmid sequencing performed by Plasmidsaurus were aligned with the corresponding reference plasmid sequences originally designed by GeneScript. The alignment reports show the total number of bases analyzed and the number of mismatches and gaps/insertions identified between the sequenced plasmids and their corresponding designed sequences. The constructs analyzed were: (A) sHCoV-NL63 Nucleocapsid; (B) sHCoV-NL63 Membrane; (C) sHCoV-229E Nucleocapsid; (D) sHCoV-229E Spike; (E) sHCoV-NL63 Envelope; (F) sHCoV-NL63 ORF1B; (G) sHCoV-229E Protein 4A; (H) sHCoV-NL63 Protein 3; (I) sHCoV-NL63 Spike; (J) sHCoV-229E Membrane; (K) sHCoV-229E Protein 4B; and (L) sHCoV-229E Envelope. All analyzed constructs showed complete alignment with their corresponding designed sequences, with no mismatches detected. A single-nucleotide gap was reported for the sHCoV-NL63 ORF1B and Spike constructs. In both constructs, the gap was located outside the protein-coding sequence, downstream of the stop codon but upstream of the IRES site.

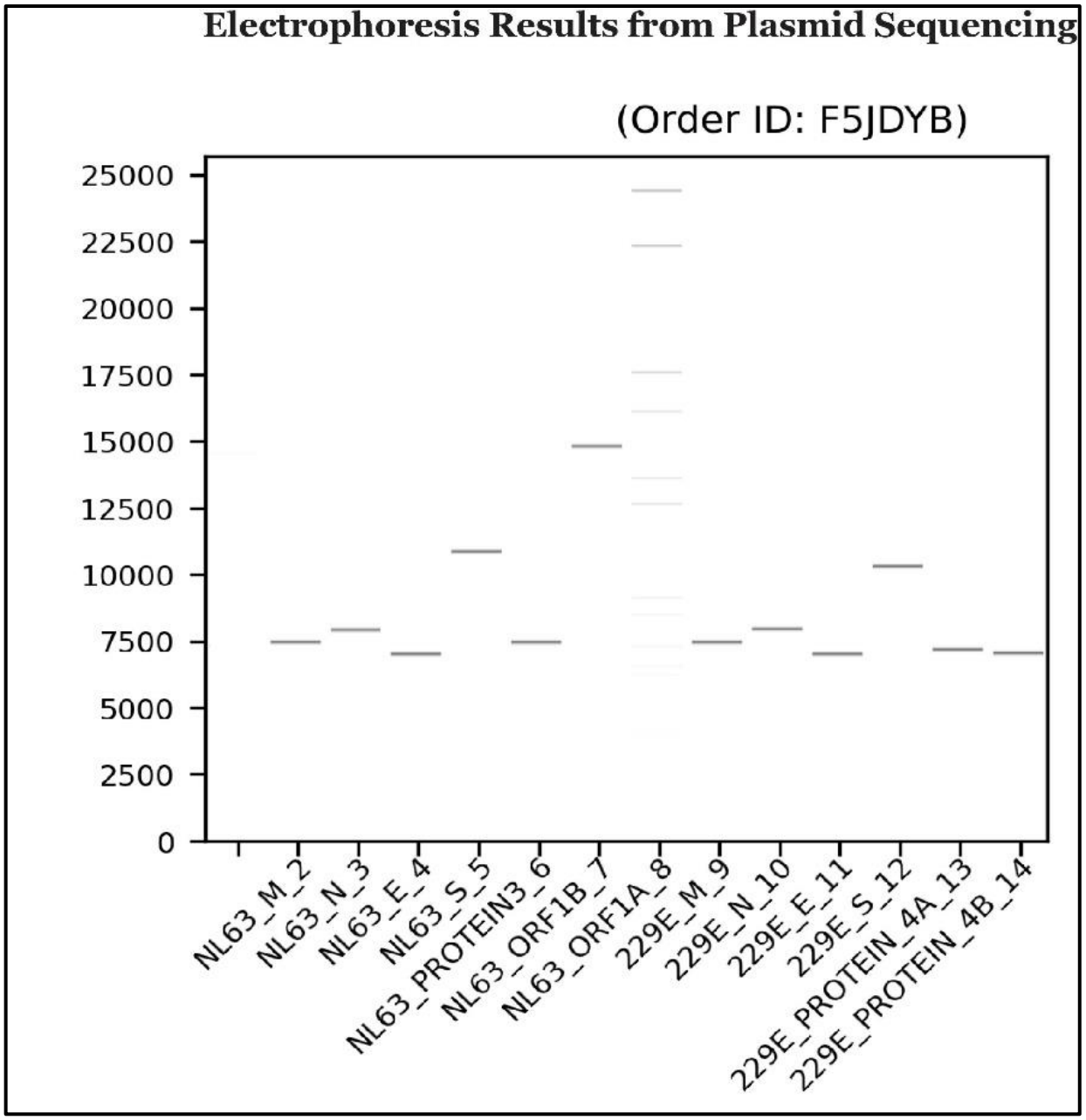

Figure 6. Electrophoresis results from whole-plasmid sequencing of the viral protein expression constructs. Electrophoresis results obtained from the plasmid sequencing performed by Plasmidsaurus for the sHCoV-NL63 and sHCoV-229E viral protein expression plasmids. The electrophoretic profiles represent the estimated size of each submitted plasmid following sequencing and were used as an additional assessment of plasmid size and integrity. The constructs analyzed were sHCoV-NL63 Membrane (NL63_M_2), Nucleocapsid (NL63_N_3), Envelope (NL63_E_4), Protein 3 (NL63_PROTEIN3_6), ORF1B (NL63_ORF1B_7), ORF1A (NL63_ORF1A_8), and sHCoV-229E Membrane (229E_M_9), Nucleocapsid (229E_N_10), Envelope (229E_E_11), Spike (229E_S_12), Protein 4A (229E_PROTEIN_4A_13), and Protein 4B (229E_PROTEIN_4B_14). The electrophoresis size profiles were evaluated together with the sequencing alignment results to support validation of the submitted plasmid constructs.

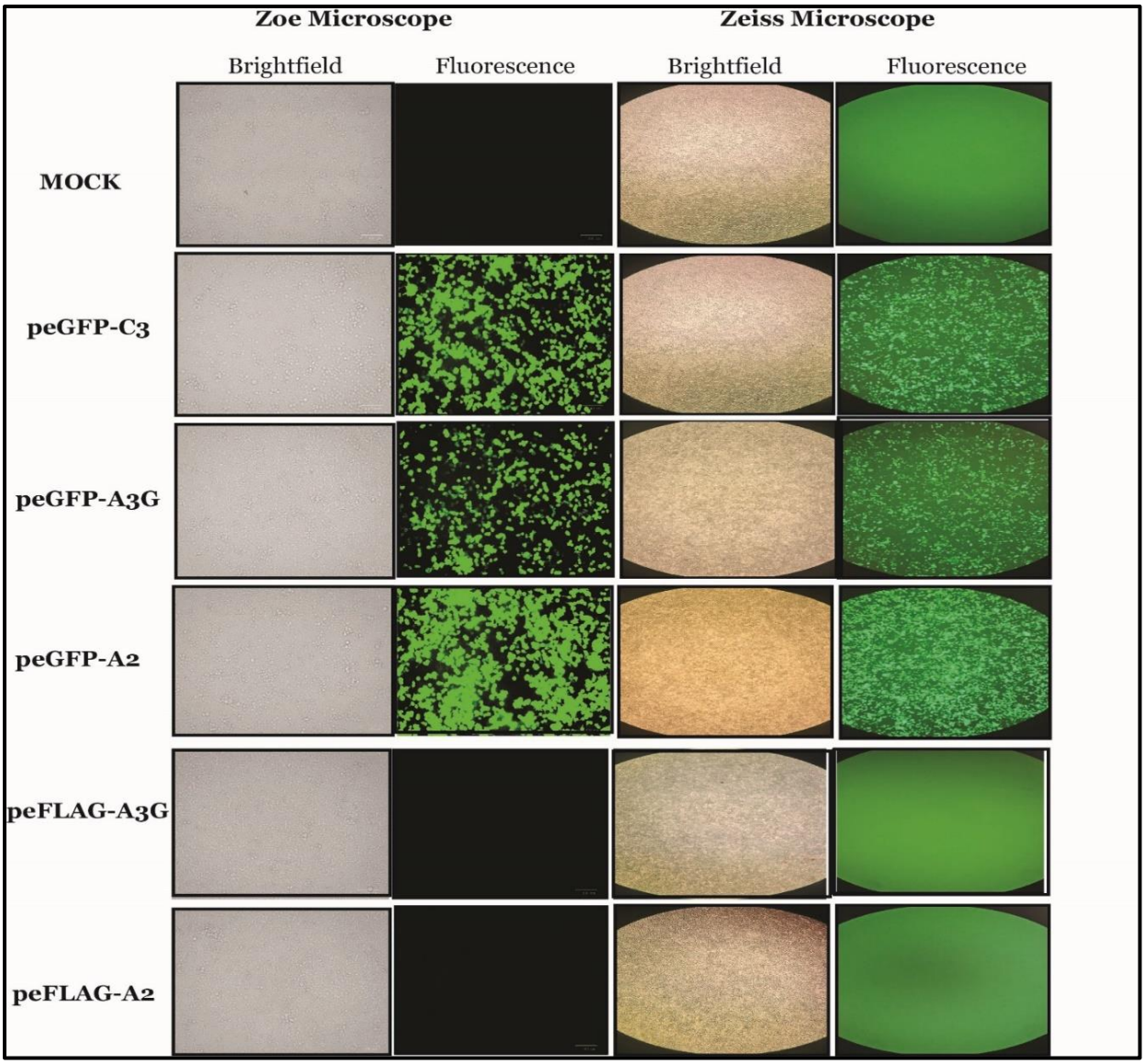

Figure 7. Fluorescence microscopy analysis of GFP-expressing control plasmids during optimization of the transfection and fluorescence detection system in HEK293T cells. Representative brightfield and fluorescence microscopy images of HEK293T cells transfected with GFP-expressing control plasmids (peGFP-C3, peGFP-A3G, and peGFP-A2) or FLAG-expressing control plasmids (peFLAG-A3G and peFLAG-A2). Mock cells were included as a negative control. Cells transfected with the GFP plasmids showed detectable green fluorescence, whereas mock cells and cells transfected with FLAG constructs showed no fluorescence. Images were acquired using Zoe and Zeiss fluorescence microscopes to qualitatively assess cell morphology and GFP fluorescence following transfection. For the Zeiss microscope, samples were visualized directly through the microscope; however, because the microscope-integrated image acquisition system was unavailable at the time of the experiment, the displayed brightfield and fluorescence images were photographed through the microscope eyepiece using a Samsung Galaxy S23 smartphone camera. These microscopy observations complemented the flow cytometry optimization experiments used to establish fluorescence detection parameters and the gating strategy for distinguishing GFP-positive from GFP-negative populations.

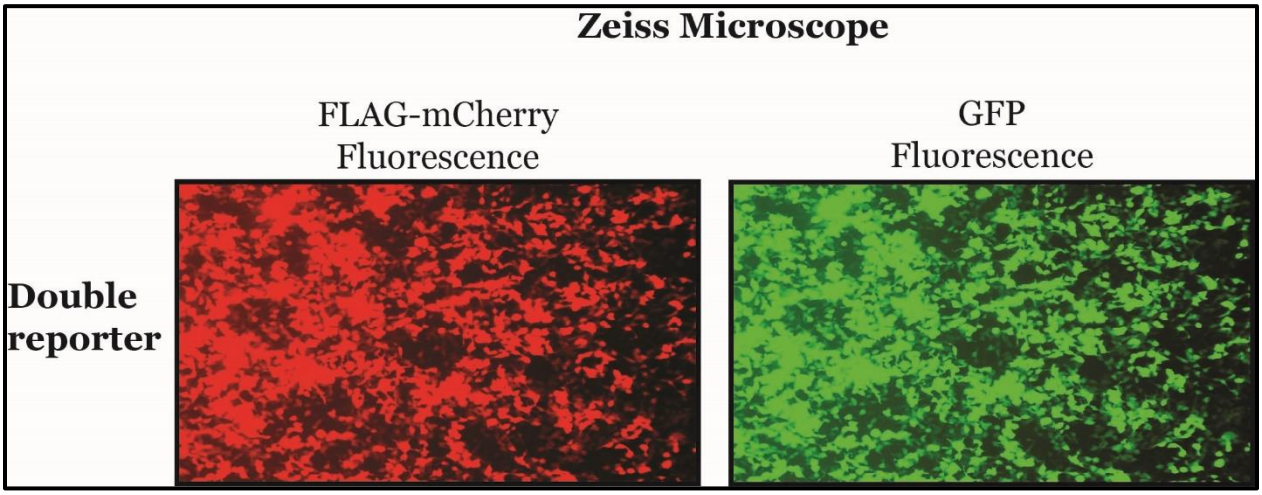

Figure 8. Fluorescence microscopy analysis of the double-reporter control in transfected HEK293T cells. Fluorescence microscopy images of HEK293T cells transfected with the double-reporter control plasmid expressing both mCherry in frame with FLAG and GFP fluorescent markers. Cells showed detectable mCherry fluorescence in the red channel and GFP fluorescence in the green channel, confirming the simultaneous expression and detection of both fluorescent markers. Images were visualized and acquired using a Zeiss inverted microscope. The images were used for qualitative visualization of fluorescence.

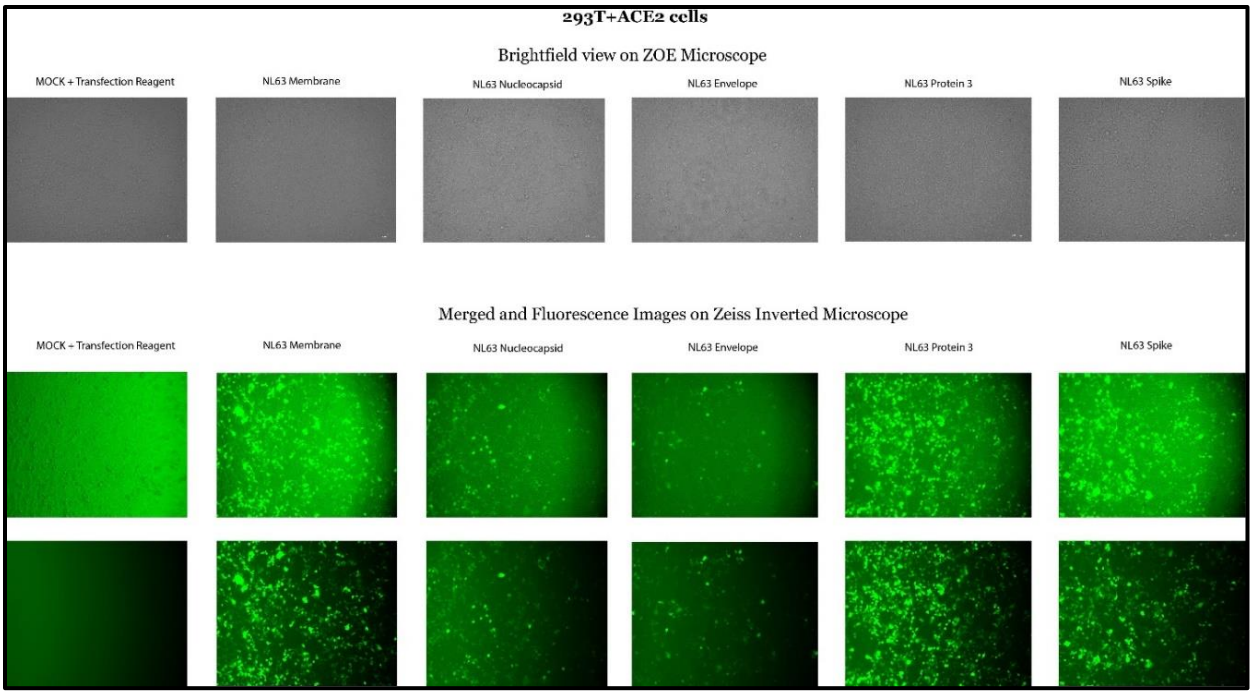

Figure 9. Brightfield and fluorescence microscopy analysis of sHCoV-NL63 viral protein constructs in transfected HEK293T+ACE2 cells. Microscopy images of HEK293T+ACE2 cells transfected with the sHCoV-NL63 Membrane, Nucleocapsid, Envelope, Protein 3, and Spike expression constructs. Mock cells exposed to the transfection reagent were included as a negative control. The **upper row** shows brightfield images acquired using the ZOE microscope to qualitatively assess cell morphology following transfection. The **middle and lower rows** show images acquired using the Zeiss inverted fluorescence microscope. The middle row represents merged brightfield and GFP fluorescence images, whereas the lower row shows the corresponding GFP fluorescence channel alone that was used to generate the merged images. The images were used for qualitative assessment of cell morphology and GFP fluorescence.

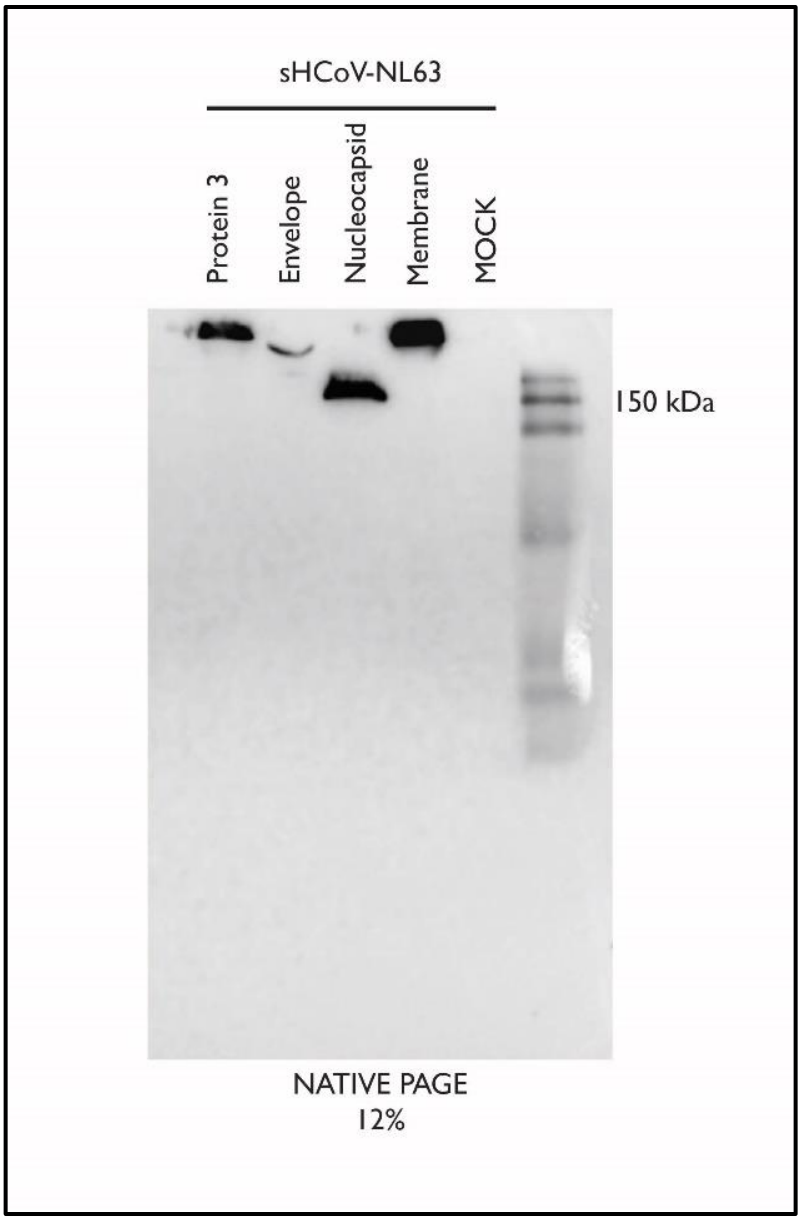

Figure 10. Native-PAGE analysis of FLAG-tagged sHCoV-NL63 viral proteins during optimization of protein detection. Native-PAGE was evaluated as an alternative electrophoretic approach during western blot troubleshooting to improve the detection of FLAG-tagged sHCoV-NL63 viral proteins. Lysates from HEK293T+ACE2 cells transfected with sHCoV-NL63 Protein 3, Envelope, Nucleocapsid, and Membrane constructs were separated under native conditions using a 12% polyacrylamide gel, with mock cells included as a negative control. Native-PAGE resulted in distinct FLAG bands for the evaluated viral proteins. However, protein migration did not correspond to the expected molecular weights. Therefore, although Native-PAGE improved visualization of FLAG bands, it was used only as part of the qualitative optimization of FLAG detection and was not selected for subsequent molecular-weight comparison of the viral proteins.

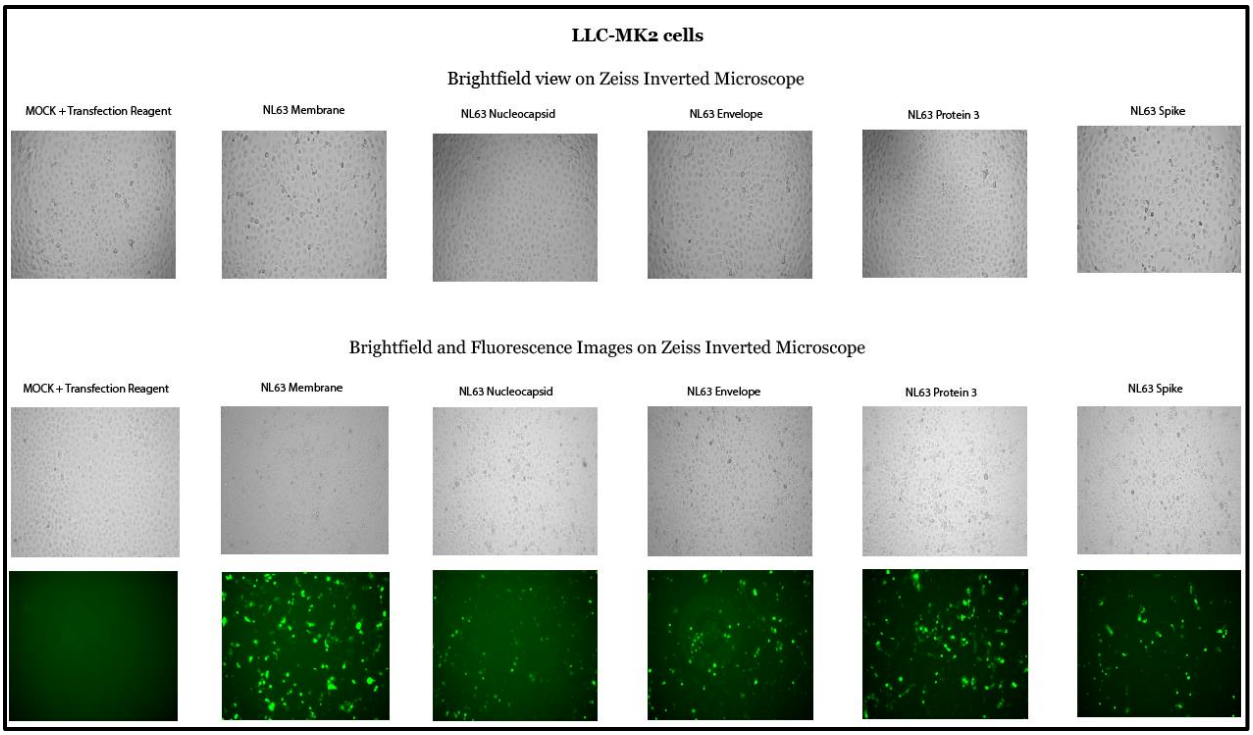

Figure 11. Brightfield and fluorescence microscopy analysis of sHCoV-NL63 viral protein constructs in transfected LLC-MK2 cells. Microscopy images of LLC-MK2 cells transfected with the sHCoV-NL63 Membrane, Nucleocapsid, Envelope, Protein 3, and Spike expression constructs. Mock cells exposed to the transfection reagent were included as a negative control. The **upper row** shows representative brightfield images acquired using the Zeiss inverted microscope to qualitatively assess cell morphology following transfection. The **middle and lower rows** show the corresponding brightfield and GFP fluorescence images, respectively, acquired during fluorescence microscopy analysis. Brightfield and fluorescence images are presented separately because the microscope acquisition system recorded the two imaging channels at different image dimensions, preventing accurate image alignment and merging. Images were therefore used for qualitative assessment of cell morphology and GFP fluorescence.

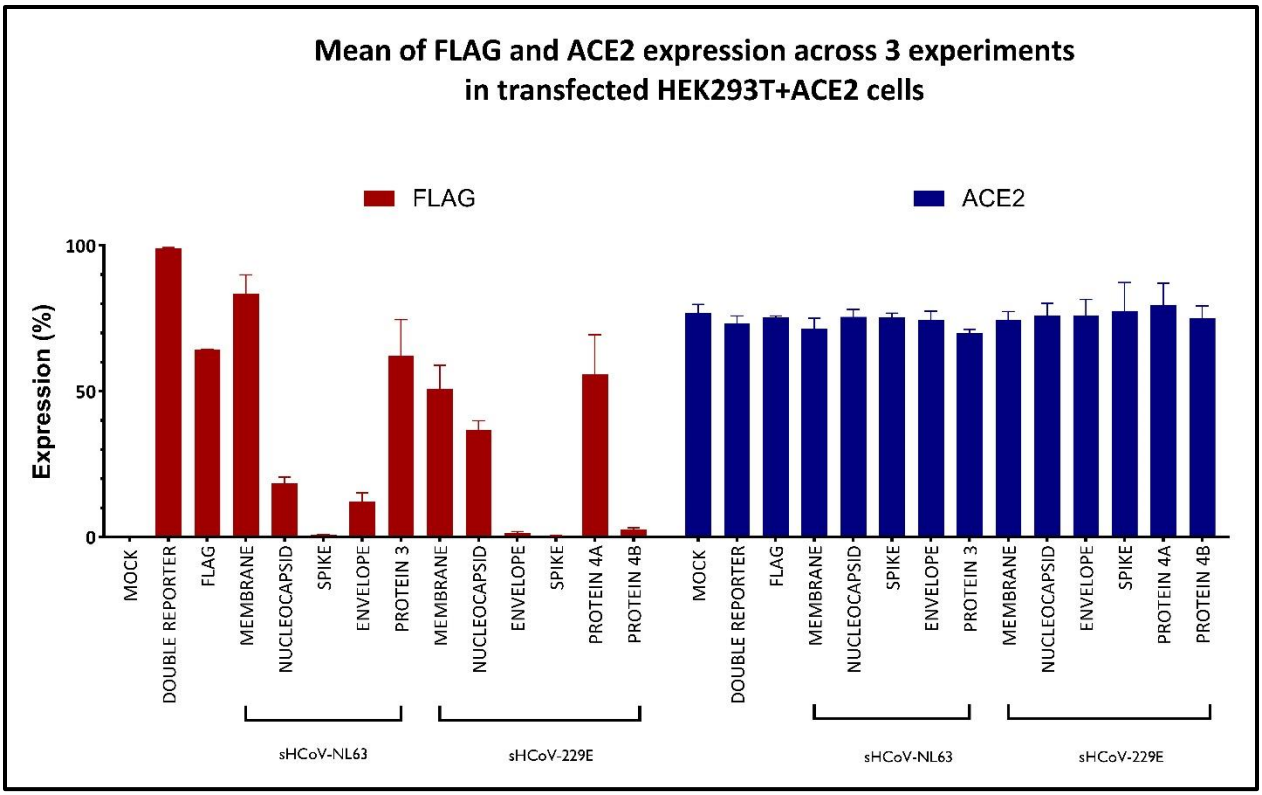

Figure 12. FLAG and cell-surface ACE2 expression in HEK293T+ACE2 cells transfected with individual sHCoV-NL63 and sHCoV-229E viral protein constructs. Flow cytometry analysis showing the average percentage of FLAG-positive cells and ACE2-positive cells across three independent experiments following transient transfection of HEK293T+ACE2 cells. FLAG detection was used to assess the presence of the FLAG-tagged viral proteins, whereas surface ACE2 staining was used to determine the percentage of ACE2-positive cells. Mock cells, the double-reporter control, and FLAG control were included as experimental controls. The sHCoV-NL63 constructs analyzed were Membrane, Nucleocapsid, Spike, Envelope and Protein 3, while the sHCoV-229E constructs included Membrane, Nucleocapsid, Envelope, Protein 4A, and Protein 4B. Data are presented as the mean ± standard deviation (SD) from three independent experiments (n = 3).

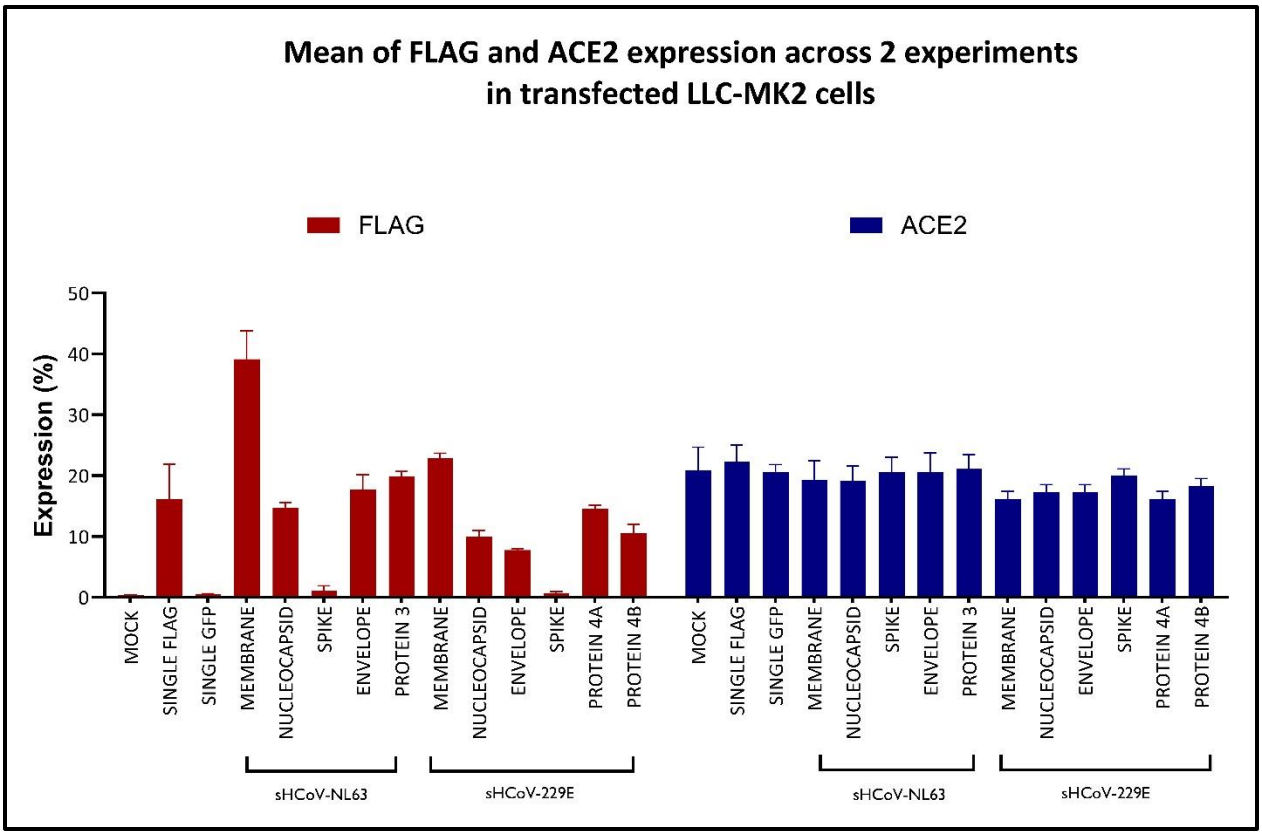

Figure 13. FLAG and cell-surface ACE2 expression in LLC-MK2 cells transfected with individual sHCoV-NL63 and sHCoV-229E viral protein constructs. Flow cytometry analysis showing the percentage of FLAG-positive and ACE2-positive cells following transient transfection of LLC-MK2 cells. FLAG detection was used to assess the presence of FLAG-tagged viral proteins, whereas surface ACE2 staining was used to determine the percentage of ACE2-positive cells. Mock-transfected cells, the single-FLAG control, and the single-GFP control were included as experimental controls. The sHCoV-NL63 constructs analyzed were Membrane, Nucleocapsid, Spike, Envelope, and Protein 3, while the sHCoV-229E constructs included Membrane, Nucleocapsid, Envelope, Spike, Protein 4A, and Protein 4B. Data are presented as the mean ± standard deviation (SD) from two independent experiments (n = 2).

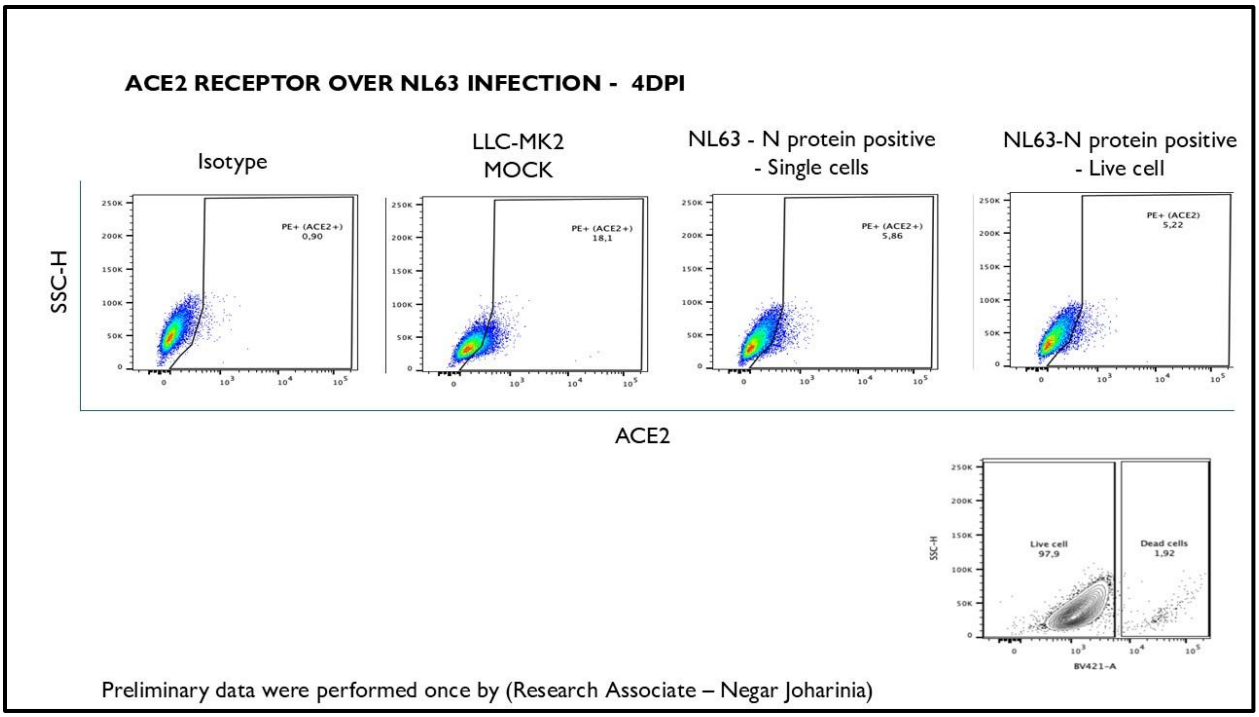

Figure 14. Preliminary assessment of ACE2 surface expression in sHCoV-NL63-infected LLC-MK2 cells after viability-based gating. LLC-MK2 cells were infected with sHCoV-NL63 and analyzed at 4 days post-infection (DPI) by flow cytometry. Cells were stained for surface ACE2 expression, intracellular sHCoV-NL63 N protein to identify infected cells, and with a viability marker to distinguish live and dead cells. Representative plots show the isotype control, mock uninfected cells, cells gated by N protein-positive and single cells, and N protein-positive and live cells. ACE2-positive mock cells represented 18.1% of ACE2 expression, compared with 5.86% of cells gated by N protein-positive and single cells, and 5.22% of cells gated by N protein-positive and live cells. The persistence of reduced ACE2 detection when the analysis was restricted to viable N protein-positive cells suggests that the decrease in surface ACE2 at this late stage of infection may not be attributable to cell death or loss of infected cells. These data are preliminary, were generated independently by Research Associate Negar Joharinia, and are not included in the experimental results of the present thesis. The author authorized the use of these data as a reference for this thesis.

Disclaimer

The thesis was grammatically reviewed and improved by ChatGPT AI and Grammarly AI, all modifications were carefully reviewed by the author. In Addition, the references were generated by AI in APA format, tested and reviewed by the author.

Bibliography (References)

Abdul-Rasool, S., & Fielding, B. C. (2010). Understanding human coronavirus HCoV-NL63. *The Open Virology Journal, 4*, 76–84. https://doi.org/10.2174/1874357901004010076

Amelimojarad, M., & Amelimojarad, M. (2025). The dual role of ACE2 in viral infections and neurodegeneration: Mechanisms and therapeutic opportunities. *Journal of Neurovirology, 31*(5), 397–406. https://doi.org/10.1007/s13365-025-01282-7

Arndt, A. L., Larson, B. J., & Hogue, B. G. (2010). A conserved domain in the coronavirus membrane protein tail is important for virus assembly. *Journal of Virology, 84*(21), 11418–11428. https://doi.org/10.1128/JVI.01131-10

Banach, B. S., Orenstein, J. M., Fox, L. M., Randell, S. H., Rowley, A. H., & Baker, S. C. (2009). Human airway epithelial cell culture to identify new respiratory viruses: Coronavirus NL63 as a model. *Journal of Virological Methods, 156*(1–2), 19–26. https://doi.org/10.1016/j.jviromet.2008.10.022

Bergmann, C. C., & Silverman, R. H. (2020). COVID-19: Coronavirus replication, pathogenesis, and therapeutic strategies. *Cleveland Clinic Journal of Medicine, 87*(6), 321–327. https://doi.org/10.3949/ccjm.87a.20047

Bio-Rad Laboratories. (n.d.). *Bulletin 6376: Protein assays: A comparison of the Bradford, BCA, and Lowry methods.* https://www.biorad.com/webroot/web/pdf/lsr/literature/Bulletin_6376.pdf

Boncristiani, H. F., Criado, M. F., & Arruda, E. (2009). Respiratory viruses. In M. Schaechter (Ed.), *Encyclopedia of microbiology* (3rd ed., pp. 500–518). Academic Press. https://doi.org/10.1016/B978-012373944-5.00314-X

Carstens, G., Kozanli, E., Bulsink, K., McDonald, S. A., Elahi, M., de Bakker, J., Schipper, M., van Gageldonk-Lafeber, R., van den Hof, S., van Hoek, A. J., & Eggink, D. (2025). Co-infection dynamics of SARS-CoV-2 and respiratory viruses in the 2022/2023 respiratory season in the Netherlands. *Journal of Infection, 90*(5), Article 106474. https://doi.org/10.1016/j.jinf.2025.106474

Castillo, G., Mora-Díaz, J. C., Breuer, M., Singh, P., Nelli, R. K., & Giménez-Lirola, L. G. (2023). Molecular mechanisms of human coronavirus NL63 infection and replication. *Virus Research, 327*, 199078. https://doi.org/10.1016/j.virusres.2023.199078

National Center for Immunization and Respiratory Diseases. (2020). *Common human coronaviruses*. Centers for Disease Control and Prevention. https://stacks.cdc.gov/view/cdc/112502

Chan, K. K., Tan, T. J. C., Narayanan, K. K., & Procko, E. (2021). An engineered decoy receptor for SARS-CoV-2 broadly binds protein S sequence variants. *Science Advances, 7*(8), eabf1738. https://doi.org/10.1126/sciadv.abf1738

Channappanavar, R., & Perlman, S. (2020). Age-related susceptibility to coronavirus infections: Role of impaired and dysregulated host immunity. *The Journal of Clinical Investigation, 130*(12), 6204–6213. https://doi.org/10.1172/JCI144115

Chaung, J., Chan, D., Pada, S., & Tambyah, P. A. (2020). Coinfection with COVID-19 and coronavirus HKU1—The critical need for repeat testing if clinically indicated. *Journal of Medical Virology, 92*(10), 1785–1786. https://doi.org/10.1002/jmv.25890

Chazal, N. (2021). Coronavirus, the king who wanted more than a crown: From common to the highly pathogenic SARS-CoV-2, is the key in the accessory genes? *Frontiers in Microbiology, 12*, 682603. https://doi.org/10.3389/fmicb.2021.682603

Chen, B., Tian, E. K., He, B., Tian, L., Han, R., Wang, S., Xiang, Q., Zhang, S., El Arnaout, T., & Cheng, W. (2020). Overview of lethal human coronaviruses. *Signal Transduction and Targeted Therapy, 5*(1), 89. https://doi.org/10.1038/s41392-020-0190-2

Chen, Y., Liu, Q., & Guo, D. (2020). Emerging coronaviruses: Genome structure, replication, and pathogenesis. *Journal of medical virology*, *92*(4), 418–423. https://doi.org/10.1002/jmv.25681

Chong, Z. X., Yeap, S. K., & Ho, W. Y. (2021). Transfection types, methods and strategies: A technical review. *PeerJ, 9*, e11165. https://doi.org/10.7717/peerj.11165

da Silva Torres, M. K., Bichara, C. D. A., de Almeida, M. N. S., Vallinoto, M. C., Queiroz, M. A. F., Vallinoto, I. M. V. C., dos Santos, E. J. M., de Carvalho, C. A. M., & Vallinoto, A. C. R. (2022). The complexity of SARS-CoV-2 infection and the COVID-19 pandemic. *Frontiers in Microbiology, 13*, 789882. https://doi.org/10.3389/fmicb.2022.789882

Datta, G., Miller, N. M., Halcrow, P. W., Khan, N., Colwell, T., Geiger, J. D., & Chen, X. (2021). SARS-CoV-2 S1 protein induces endolysosome dysfunction and neuritic dystrophy. *Frontiers in Cellular Neuroscience, 15*, 777738. https://doi.org/10.3389/fncel.2021.777738

de Breyne, S., Vindry, C., Guillin, O., Condé, L., Mure, F., Gruffat, H., Chavatte, L., & Ohlmann, T. (2020). Translational control of coronaviruses. *Nucleic Acids Research, 48*(22), 12502–12522. https://doi.org/10.1093/nar/gkaa1116

de Haan, C. A. M., Vennema, H., & Rottier, P. J. M. (2000). Assembly of the coronavirus envelope: Homotypic interactions between the M proteins. *Journal of Virology, 74*(11), 4967–4978. https://doi.org/10.1128/JVI.74.11.4967-4978.2000

De Pasquale, V., Quiccione, M. S., Tafuri, S., Avallone, L., & Pavone, L. M. (2021). Heparan sulfate proteoglycans in viral infection and treatment: A special focus on SARS-CoV-2. *International Journal of Molecular Sciences, 22*(12), 6574. https://doi.org/10.3390/ijms22126574

Devarakonda, C. K. V., Meredith, E., Ghosh, M., & Shapiro, L. H. (2021). Coronavirus receptors as immune modulators. *The Journal of Immunology, 206*(5), 923–929. https://doi.org/10.4049/jimmunol.2001062

Duan, T., Du, Y., Xing, C., Wang, H. Y., & Wang, R. F. (2022). Toll-like receptor signaling and its role in cell-mediated immunity. *Frontiers in Immunology, 13*, 812774. https://doi.org/10.3389/fimmu.2022.812774

EMD Millipore. (n.d.). *GeneJuice® transfection reagent*. Retrieved November 14, 2024, from https://www.sigmaaldrich.com/CA/en/product/mm/70967

Enjuanes, L., Zuñiga, S., Castaño-Rodriguez, C., Gutierrez-Alvarez, J., Canton, J., & Sola, I. (2016). Molecular basis of coronavirus virulence and vaccine development. *Advances in Virus Research, 96*, 245–286. https://doi.org/10.1016/bs.aivir.2016.08.003

Fahlberg, M. D., Forward, S., Assita, E. R., Mazzola, M., Kiem, A., Handley, M., Yun, S.-H., & Kwok, S. J. J. (2024). Overcoming fixation and permeabilization challenges in flow cytometry by optical barcoding and multi-pass acquisition. *Cytometry Part A, 105*(11), 838–848. https://doi.org/10.1002/cyto.a.24904

Fan, H., Tian, M., Liu, S., Ye, C., Li, Z., Wu, K., & Zhu, C. (2024). Strategies used by SARS-CoV-2 to evade the innate immune system in an evolutionary perspective. *Pathogens, 13*(12), 1117. https://doi.org/10.3390/pathogens13121117

Fausto, A., Otter, C. J., Torres, L., Blomqvist, E. K., Bracci, N., Renner, D. M., Tan, L. H., Mooring, D., Ebert, N., Trüeb, B., Thiel, V., Cohen, N. A., Burke, J. M., & Weiss, S. R. (2026). Human alphacoronavirus replication and innate immune induction in airway culture systems. *mBio, 17*(1), e03203-25. https://doi.org/10.1128/mbio.03203-25

Fehr, A. R., & Perlman, S. (2015). Coronaviruses: An overview of their replication and pathogenesis. In H. J. Maier, E. Bickerton, & P. Britton (Eds.), *Coronaviruses: Methods and protocols* (Methods in Molecular Biology, Vol. 1282, pp. 1–23). Humana Press. https://doi.org/10.1007/978-1-4939-2438-7_1

Gao, X., & Wu, Z. (2025). IRES-mediated translation: Expanding the toolkits of RNA therapy. *International Journal of Molecular Sciences, 26*(21), 10542. https://doi.org/10.3390/ijms262110542

Gerna, G., Percivalle, E., Sarasini, A., Campanini, G., Piralla, A., Rovida, F., Genini, E., Marchi, A., & Baldanti, F. (2007). Human respiratory coronavirus HKU1 versus other coronavirus infections in Italian hospitalised patients. *Journal of Clinical Virology, 38*(3), 244–250. https://doi.org/10.1016/j.jcv.2006.12.008

Glowacka, I., Bertram, S., Herzog, P., Pfefferle, S., Steffen, I., Muench, M. O., Simmons, G., Hofmann, H., Kuri, T., Weber, F., Eichler, J., Drosten, C., & Pöhlmann, S. (2010). Differential downregulation of ACE2 by the spike proteins of severe acute respiratory syndrome coronavirus and human coronavirus NL63. *Journal of Virology, 84*(2), 1198–1205. https://doi.org/10.1128/JVI.01248-09

Harrison, A. G., Lin, T., & Wang, P. (2020). Mechanisms of SARS-CoV-2 transmission and pathogenesis. *Trends in Immunology, 41*(12), 1100–1115. https://doi.org/10.1016/j.it.2020.10.004

Harrison, C. M., Doster, J. M., Landwehr, E. H., Kumar, N. P., White, E. J., Beachboard, D. C., & Stobart, C. C. (2023). Evaluating the virology and evolution of seasonal human coronaviruses associated with the common cold in the COVID-19 era. *Microorganisms, 11*(2), 445. https://doi.org/10.3390/microorganisms11020445

Hasöksüz, M., Kiliç, S., & Saraç, F. (2020). Coronaviruses and SARS-CoV-2. *Turkish Journal of Medical Sciences, 50*(SI-1), 549–556. https://doi.org/10.3906/sag-2004-127

Herzog, P., Drosten, C., & Müller, M. A. (2008). Plaque assay for human coronavirus NL63 using human colon carcinoma cells. *Virology Journal, 5*, 138. https://doi.org/10.1186/1743-422X-5-138

Hikmet, F., Méar, L., Edvinsson, Å., Micke, P., Uhlén, M., & Lindskog, C. (2020). The protein expression profile of ACE2 in human tissues. *Molecular Systems Biology, 16*(7), e9610. https://doi.org/10.15252/msb.20209610

Hoffmann, M., Kleine-Weber, H., Schroeder, S., Krüger, N., Herrler, T., Erichsen, S., Schiergens, T. S., Herrler, G., Wu, N.-H., Nitsche, A., Müller, M. A., Drosten, C., & Pöhlmann, S. (2020). SARS-CoV-2 cell entry depends on ACE2 and TMPRSS2 and is blocked by a clinically proven protease inhibitor. *Cell, 181*(2), 271–280.e8. https://doi.org/10.1016/j.cell.2020.02.052

Hopfner, K.-P., & Hornung, V. (2020). Molecular mechanisms and cellular functions of cGAS–STING signalling. *Nature Reviews Molecular Cell Biology, 21*(9), 501–521. https://doi.org/10.1038/s41580-020-0244-x

Huang, S. H., Su, M. C., Tien, N., Huang, C. J., Lan, Y. C., Lin, C. S., Chen, C. H., & Lin, C. W. (2017). Epidemiology of human coronavirus NL63 infection among hospitalized patients with pneumonia in Taiwan. *Journal of Microbiology, Immunology and Infection, 50*(6), 763–770. https://doi.org/10.1016/j.jmii.2015.10.008

Hulswit, R. J. G., Lang, Y., Bakkers, M. J. G., Li, W., Li, Z., Schouten, A., Ophorst, B., van Kuppeveld, F. J. M., Boons, G.-J., Bosch, B.-J., Huizinga, E. G., & de Groot, R. J. (2019). Human coronaviruses OC43 and HKU1 bind to 9-O-acetylated sialic acids via a conserved receptor-binding site in spike protein domain A. *Proceedings of the National Academy of Sciences of the United States of America, 116*(7), 2681–2690. https://doi.org/10.1073/pnas.1809667116

Huynh, J., Li, S., Yount, B., Smith, A., Sturges, L., Olsen, J. C., Nagel, J., Johnson, J. B., Agnihothram, S., Gates, J. E., Frieman, M. B., Baric, R. S., & Donaldson, E. F. (2012). Evidence supporting a zoonotic origin of human coronavirus strain NL63. *Journal of Virology, 86*(23), 12816–12825. https://doi.org/10.1128/JVI.00906-12

Islamuddin, M., Mustfa, S. A., Ullah, S. N. M. N., Omer, U., Kato, K., & Parveen, S. (2022). Innate immune response and inflammasome activation during SARS-CoV-2 infection. *Inflammation, 45*(5), 1849–1863. https://doi.org/10.1007/s10753-022-01651-y

Jia, H. P., Look, D. C., Tan, P., Shi, L., Hickey, M., Gakhar, L., Chappell, M. C., Wohlford-Lenane, C., & McCray, P. B., Jr. (2009). Ectodomain shedding of angiotensin converting enzyme 2 in human airway epithelia. *American Journal of Physiology-Lung Cellular and Molecular Physiology, 297*(1), L84–L96. https://doi.org/10.1152/ajplung.00071.2009

Kasuga, Y., Zhu, B., Jang, K.-J., & Yoo, J.-S. (2021). Innate immune sensing of coronavirus and viral evasion strategies. *Experimental & Molecular Medicine, 53*(5), 723–736. https://doi.org/10.1038/s12276-021-00602-1

Kawase, M., Shirato, K., van der Hoek, L., Taguchi, F., & Matsuyama, S. (2012). Simultaneous treatment of human bronchial epithelial cells with serine and cysteine protease inhibitors prevents severe acute respiratory syndrome coronavirus entry. *Journal of Virology, 86*(12), 6537–6545. https://doi.org/10.1128/JVI.00094-12

Keshavarz Valian, N., Pourakbari, B., Asna Ashari, K., Hosseinpour Sadeghi, R., & Mahmoudi, S. (2022). Evaluation of human coronavirus OC43 and SARS-CoV-2 in children with respiratory tract infection during the COVID-19 pandemic. *Journal of Medical Virology, 94*(4), 1450–1456. https://doi.org/10.1002/jmv.27460

Lagacé-Wiens, P., Bullard, J., Cole, R., & Van Caeseele, P. (2021). Seasonality of coronaviruses and other respiratory viruses in Canada: Implications for COVID-19. *Canada Communicable Disease Report, 47*(3), 132–138. https://doi.org/10.14745/ccdr.v47i03a02

Lambert, D. W., Yarski, M., Warner, F. J., Thornhill, P., Parkin, E. T., Smith, A. I., Hooper, N. M., & Turner, A. J. (2005). Tumor necrosis factor-alpha convertase (ADAM17) mediates regulated ectodomain shedding of the severe acute respiratory syndrome coronavirus (SARS-CoV) receptor, angiotensin-converting enzyme-2 (ACE2). *Journal of Biological Chemistry, 280*(34), 30113–30119. https://doi.org/10.1074/jbc.M505111200

Lamkiewicz, K., Esquivel Gomez, L. R., Kühnert, D., & Marz, M. (2023). Genome structure, life cycle, and taxonomy of coronaviruses and the evolution of SARS-CoV-2. In E. Domingo, P. Schuster, S. F. Elena, & C. Perales (Eds.), *Viral fitness and evolution* (Current Topics in Microbiology and Immunology, Vol. 439, pp. 305–339). Springer. https://doi.org/10.1007/978-3-031-15640-3_9

Latifi-Pupovci, H. (2022). Molecular mechanisms involved in pathogenicity of SARS-CoV-2: Immune evasion and implications for therapeutic strategies. *Biomedicine & Pharmacotherapy, 153*, 113368. https://doi.org/10.1016/j.biopha.2022.113368

Lau, S. K. P., Lung, D. C., Wong, E. Y. M., Aw-Yong, K. L., Wong, A. C. P., Luk, H. K. H., Li, K. S. M., Fung, J., Chan, T. T. Y., Tang, J. Y. M., Zhu, L., Yip, C. C. Y., Wong, S. C. Y., Lee, R. A., Tsang, O. T. Y., Yuen, K.-Y., & Woo, P. C. Y. (2021). Molecular evolution of human coronavirus 229E in Hong Kong and a fatal COVID-19 case involving coinfection with a novel human coronavirus 229E genogroup. *mSphere, 6*(1), e00819-20. https://doi.org/10.1128/mSphere.00819-20

Lednicky, J. A., Waltzek, T. B., McGeehan, E., Loeb, J. C., Hamilton, S. B., & Luetke, M. C. (2013). Isolation and genetic characterization of human coronavirus NL63 in primary human renal proximal tubular epithelial cells obtained from a commercial supplier, and confirmation of its replication in two different types of human primary kidney cells. *Virology Journal, 10*, 213. https://doi.org/10.1186/1743-422X-10-213

Lei, J., Kusov, Y., & Hilgenfeld, R. (2018). Nsp3 of coronaviruses: Structures and functions of a large multi-domain protein. *Antiviral Research, 149*, 58–74. https://doi.org/10.1016/j.antiviral.2017.11.001

Li, C.-X., Noreen, S., Zhang, L.-X., Saeed, M., Wu, P.-F., Ijaz, M., Dai, D.-F., Maqbool, I., Madni, A., Akram, F., Naveed, M., & Li, J.-H. (2022). A critical analysis of SARS-CoV-2 (COVID-19) complexities, emerging variants, and therapeutic interventions and vaccination strategies. *Biomedicine & Pharmacotherapy, 146*, 112550. https://doi.org/10.1016/j.biopha.2021.112550

Li, X., Luk, H. K. H., Lau, S. K. P., & Woo, P. C. Y. (2019). Human coronaviruses: General features. In *Reference module in biomedical sciences*. Elsevier. https://doi.org/10.1016/B978-0-12-801238-3.95704-0

Li, F. (2016). Structure, function, and evolution of coronavirus spike proteins. *Annual Review of Virology, 3*(1), 237–261. https://doi.org/10.1146/annurev-virology-110615-042301

Lim, Y. X., Ng, Y. L., Tam, J. P., & Liu, D. X. (2016). Human coronaviruses: A review of virus-host interactions. *Diseases, 4*(3), 26. https://doi.org/10.3390/diseases4030026

Liu, D. X., Liang, J. Q., & Fung, T. S. (2021). Human coronavirus-229E, -OC43, -NL63, and -HKU1 (Coronaviridae). In D. H. Bamford & M. Zuckerman (Eds.), *Encyclopedia of virology* (4th ed., pp. 428–440). Academic Press. https://doi.org/10.1016/B978-0-12-809633-8.21501-X

Liu, Y., Lu, H., Li, J., Xie, Y., Hu, G., Pang, S., Lian, S., Liu, J., Zhu, G., & Ding, X. (2025). A comprehensive view on the mechanisms of coronavirus escaping innate immunity. *Veterinary Sciences, 12*(12), 1156. https://doi.org/10.3390/vetsci12121156

Ljubin-Sternak, S., Meštrović, T., Lukšić, I., Mijač, M., & Vraneš, J. (2021). Seasonal coronaviruses and other neglected respiratory viruses: A global perspective and a local snapshot. *Frontiers in Public Health, 9*, 691163. https://doi.org/10.3389/fpubh.2021.691163

Lu, L., Zhong, W., Bian, Z., Li, Z., Zhang, K., Liang, B., Zhong, Y., Hu, M., Lin, L., Liu, J., Lin, X., Huang, Y., Jiang, J., Yang, X., Zhang, X., & Huang, Z. (2020). A comparison of mortality-related risk factors of COVID-19, SARS, and MERS: A systematic review and meta-analysis. *Journal of Infection, 81*(4), e18–e25. https://doi.org/10.1016/j.jinf.2020.07.002

Lu, C., Amin, M. A., & Fox, D. A. (2020). CD13/Aminopeptidase N is a potential therapeutic target for inflammatory disorders. *The Journal of Immunology, 204*(1), 3–11. https://doi.org/10.4049/jimmunol.1900868

Lubbe, L., Cozier, G. E., Oosthuizen, D., Acharya, K. R., & Sturrock, E. D. (2020). ACE2 and ACE: Structure-based insights into mechanism, regulation and receptor recognition by SARS-CoV. *Clinical Science, 134*(21), 2851–2871. https://doi.org/10.1042/CS20200899

Madaras, L., Anvari, R., Schuchardt-Peet, C., Hoskote, A., & Kashyap, R. (2025). Co-infection with severe acute respiratory syndrome coronavirus 2 (SARS-CoV-2) and human coronavirus HKU1 (HCoV-HKU1). *European Journal of Case Reports in Internal Medicine, 12*(2), 005068. https://doi.org/10.12890/2025_005068

Mahmood, T., & Yang, P.-C. (2012). Western blot: Technique, theory, and trouble shooting. *North American Journal of Medical Sciences, 4*(9), 429–434. https://doi.org/10.4103/1947-2714.100998

McCallum, M., Park, Y.-J., Stewart, C., Sprouse, K. R., Addetia, A., Brown, J., Tortorici, M. A., Gibson, C., Wong, E., Ieven, M., Telenti, A., & Veesler, D. (2024). Human coronavirus HKU1 recognition of the TMPRSS2 host receptor. *Cell, 187*(16), 4231–4245.e13. https://doi.org/10.1016/j.cell.2024.06.006

Menon, V., Thomas, R., Ghale, A. R., Reinhard, C., & Pruszak, J. (2014). Flow cytometry protocols for surface and intracellular antigen analyses of neural cell types. *Journal of Visualized Experiments*, (94), 52241. https://doi.org/10.3791/52241

Meyers, W. M., Hong, R. J., Sin, W. C., Kim, C. S., & Haas, K. (2023). A cell-based assay for rapid assessment of ACE2 catalytic function. *Scientific Reports, 13*, 14123. https://doi.org/10.1038/s41598-023-41389-7

Milewska, A., Zarebski, M., Nowak, P., Stozek, K., Potempa, J., & Pyrc, K. (2014). Human coronavirus NL63 utilizes heparan sulfate proteoglycans for attachment to target cells. *Journal of Virology, 88*(22), 13221–13230. https://doi.org/10.1128/JVI.02078-14

Mingaleeva, R. N., Nigmatulina, N. A., Sharafetdinova, L. M., Romozanova, A. M., Gabdoulkhakova, A. G., Filina, Y. V., Shavaliyev, R. F., Rizvanov, A. A., & Miftakhova, R. R. (2022). Biology of the SARS-CoV-2 coronavirus. *Biochemistry (Moscow), 87*(12–13), 1662–1678. https://doi.org/10.1134/S0006297922120215

Minkoff, J. M., & tenOever, B. (2023). Innate immune evasion strategies of SARS-CoV-2. *Nature Reviews Microbiology, 21*(3), 178–194. https://doi.org/10.1038/s41579-022-00839-1

Misbah, S., Ahmad, A., Butt, M. H., Khan, Y. H., Alotaibi, N. H., & Mallhi, T. H. (2020). A systematic analysis of studies on Corona Virus Disease 19 (COVID-19) from viral emergence to treatment. *Journal of the College of Physicians and Surgeons Pakistan, 30*(Suppl. 1), S9–S18. https://doi.org/10.29271/jcpsp.2020.Supp1.S9

Mizuguchi, H., Xu, Z., Ishii-Watabe, A., Uchida, E., & Hayakawa, T. (2000). IRES-dependent second gene expression is significantly lower than cap-dependent first gene expression in a bicistronic vector. *Molecular Therapy, 1*(4), 376–382. https://doi.org/10.1006/mthe.2000.0050

Mponponsuo, K., Murthy, Y., Kanji, J., Tremblay, A., Khan, D., Conly, J., & Somayaji, R. (2023). Co-infection of SARS-CoV-2 with human coronavirus OC43 in a patient with underlying lung disease: A case report. *Journal of the Association of Medical Microbiology and Infectious Disease Canada, 8*(2), 150–153. https://doi.org/10.3138/jammi-2022-0030

Müller, M. A., van der Hoek, L., Voss, D., Bader, O., Lehmann, D., Schulz, A. R., Kallies, S., Suliman, T., Fielding, B. C., Drosten, C., & Niedrig, M. (2010). Human coronavirus NL63 open reading frame 3 encodes a virion-incorporated N-glycosylated membrane protein. *Virology Journal, 7*(1), 6. https://doi.org/10.1186/1743-422X-7-6

Müller, N. F., Kistler, K. E., & Bedford, T. (2021). *Recombination patterns in coronaviruses* [Preprint]. bioRxiv. https://doi.org/10.1101/2021.04.28.441806

Naskalska, A., Dabrowska, A., Szczepanski, A., Milewska, A., Jasik, K. P., & Pyrc, K. (2019). Membrane protein of human coronavirus NL63 is responsible for interaction with the adhesion receptor. *Journal of Virology, 93*(19), e00355-19. https://doi.org/10.1128/JVI.00355-19

NC_005831.2. (n.d.). *Human coronavirus NL63, complete genome* [Nucleotide sequence]. NCBI Nucleotide. https://www.ncbi.nlm.nih.gov/nuccore/NC_005831.2

NC_002645.1. (n.d.). *Human coronavirus 229E, complete genome* [Nucleotide sequence]. NCBI Nucleotide. https://www.ncbi.nlm.nih.gov/nuccore/NC_002645.1

NC_006213.1. (n.d.). *Human coronavirus OC43 strain ATCC VR-759, complete genome* [Nucleotide sequence]. NCBI Nucleotide. https://www.ncbi.nlm.nih.gov/nuccore/NC_006213.1

Neerukonda, S. N., Vassell, R., Lusvarghi, S., Liu, S., Akue, A., Kukuruga, M., Wang, T. T., Weiss, C. D., & Wang, W. (2025). Characterization of spike S1/S2 processing and entry pathways of lentiviral pseudoviruses bearing seasonal human coronaviruses NL63, 229E, and HKU1 spikes. *Microbiology Spectrum, 13*(3), e02808-24. https://doi.org/10.1128/spectrum.02808-24

Nejat, R., Torshizi, M. F., & Najafi, D. J. (2023). S protein, ACE2 and host cell proteases in SARS-CoV-2 cell entry and infectivity: Is soluble ACE2 a two blade sword? A narrative review. *Vaccines, 11*(2), 204. https://doi.org/10.3390/vaccines11020204

Nor Rashid, N., Amrani, L., Alwan, A., Mohamed, Z., Yusof, R., & Rothan, H. (2025). Angiotensin-converting enzyme-2 (ACE2) downregulation during coronavirus infection. *Molecular Biotechnology, 67*(9), 3415–3427. https://doi.org/10.1007/s12033-024-01277-5

Nwokolo, G. C., Falconer, R. A., & Barnieh, F. M. (2025). Aminopeptidase N (CD13): Bridging physiology, pathology and therapeutic potential. *Advances in Clinical Chemistry, 129*, 207–269. https://doi.org/10.1016/bs.acc.2025.07.002

Ohto, U., & Shimizu, T. (2016). Structural aspects of nucleic acid-sensing Toll-like receptors. *Biophysical Reviews, 8*(1), 33–43. https://doi.org/10.1007/s12551-015-0187-1

Onabajo, O. O., Banday, A. R., Stanifer, M. L., Yan, W., Obajemu, A., Santer, D. M., Florez-Vargas, O., Piontkivska, H., Vargas, J. M., Ring, T. J., Kee, C., Doldan, P., Tyrrell, D. L., Mendoza, J. L., Boulant, S., & Prokunina-Olsson, L. (2020). Interferons and viruses induce a novel truncated ACE2 isoform and not the full-length SARS-CoV-2 receptor. *Nature Genetics, 52*(12), 1283–1293. https://doi.org/10.1038/s41588-020-00731-9

Otieno, J. R., Cherry, J. L., Spiro, D. J., Nelson, M. I., & Trovão, N. S. (2022). Origins and evolution of seasonal human coronaviruses. *Viruses, 14*(7), 1551. https://doi.org/10.3390/v14071551

Owczarek, K., Szczepanski, A., Milewska, A., Baster, Z., Rajfur, Z., Sarna, M., & Pyrc, K. (2018). Early events during human coronavirus OC43 entry to the cell. *Scientific Reports, 8*(1), 7124. https://doi.org/10.1038/s41598-018-25640-0

Piacentini, S., Riccio, A., Santopolo, S., Pauciullo, S., La Frazia, S., Rossi, A., Rossignol, J.-F., & Santoro, M. G. (2023). The FDA-approved drug nitazoxanide is a potent inhibitor of human seasonal coronaviruses acting at postentry level: Effect on the viral spike glycoprotein. *Frontiers in Microbiology, 14*, 1206951. https://doi.org/10.3389/fmicb.2023.1206951

Polyplus. (n.d.). *jetPRIME® transfection reagent: Short protocol—DNA transfection*. https://www.polyplus-sartorius.com/wp-content/uploads/2015/08/Polyplus-Short-Protocol-jetPRIME-DNA.pdf

Pouremamali, A., Babaei, A., Shatizadeh Malekshahi, S., Abbasi, A., & Rafiee, N. (2022). Understanding the pivotal roles of ACE2 in SARS-CoV-2 infection: From structure/function to therapeutic implication. *Egyptian Journal of Medical Human Genetics, 23*(1), 103. https://doi.org/10.1186/s43042-022-00314-9

Pyrc, K. (2005). *Molecular characterization of human coronavirus NL63* [Doctoral dissertation, University of Amsterdam]. https://hdl.handle.net/11245/1.243944

Ramos, S. G., Rattis, B. A. da C., Ottaviani, G., Celes, M. R. N., & Dias, E. P. (2021). ACE2 down-regulation may act as a transient molecular disease causing RAAS dysregulation and tissue damage in the microcirculatory environment among COVID-19 patients. *The American Journal of Pathology, 191*(7), 1154–1164. https://doi.org/10.1016/j.ajpath.2021.04.010

Roh, K. H., Kim, Y. K., Kim, S. W., Kang, E. R., Yang, Y. J., Jung, S. K., Lee, S. H., & Sung, N. (2021). Coinfections with respiratory pathogens among COVID-19 patients in Korea. *Canadian Journal of Infectious Diseases and Medical Microbiology, 2021*, 6651045. https://doi.org/10.1155/2021/6651045

Saponaro, F., Rutigliano, G., Sestito, S., Bandini, L., Storti, B., Bizzarri, R., & Zucchi, R. (2020). ACE2 in the era of SARS-CoV-2: Controversies and novel perspectives. *Frontiers in Molecular Biosciences, 7*, 588618. https://doi.org/10.3389/fmolb.2020.588618

Schoeman, D., & Fielding, B. C. (2019). Coronavirus envelope protein: Current knowledge. *Virology Journal, 16*(1), 69. https://doi.org/10.1186/s12985-019-1182-0

Shao, N., Zhang, C., Dong, J., Sun, L., Chen, X., Xie, Z., Xu, B., An, S., Zhang, T., & Yang, F. (2022). Molecular evolution of human coronavirus-NL63, -229E, -HKU1 and -OC43 in hospitalized children in China. *Frontiers in Microbiology, 13*, 1023847. https://doi.org/10.3389/fmicb.2022.1023847

Shen, C. R., Chen, Y. S., Hwang, Y. S., Chen, H. J., & Liu, C. L. (2021). Differential bicistronic gene translation mediated by the internal ribosome entry site element of encephalomyocarditis virus. *Biomedical Journal, 44*(6 Suppl. 1), S54–S62. https://doi.org/10.1016/j.bj.2020.06.006

Sherman, E. J., & Emmer, B. T. (2021). ACE2 protein expression within isogenic cell lines is heterogeneous and associated with distinct transcriptomes. *Scientific Reports, 11*(1), 15900. https://doi.org/10.1038/s41598-021-95308-9

Silhol, F., Sarlon, G., Deharo, J.-C., & Vaïsse, B. (2020). Downregulation of ACE2 induces overstimulation of the renin–angiotensin system in COVID-19: Should we block the renin–angiotensin system? *Hypertension Research, 43*(8), 854–856. https://doi.org/10.1038/s41440-020-0476-3

Siragam, V., Maltseva, M., Castonguay, N., Galipeau, Y., Srinivasan, M. M., Hernandez Soto, J., Dankar, S., & Langlois, M.-A. (2024). Seasonal human coronaviruses OC43, 229E, and NL63 induce cell surface modulation of entry receptors and display host cell-specific viral replication kinetics. *Microbiology Spectrum, 12*(7), e04220-23. https://doi.org/10.1128/spectrum.04220-23

Sučec, I., Pankratova, Y., Parasar, M., & Hong, M. (2024). Transmembrane conformation of the envelope protein of an alpha coronavirus, NL63. *Protein Science, 33*(4), e4923. https://doi.org/10.1002/pro.4923

Szczepanski, A., Owczarek, K., Bzowska, M., Gula, K., Drebot, I., Ochman, M., Maksym, B., Rajfur, Z., Mitchell, J. A., & Pyrc, K. (2019). Canine respiratory coronavirus, bovine coronavirus, and human coronavirus OC43: Receptors and attachment factors. *Viruses, 11*(4), 328. https://doi.org/10.3390/v11040328

Tanneti, N. S., Stillwell, H. A., & Weiss, S. R. (2025). Human coronaviruses: Activation and antagonism of innate immune responses. *Microbiology and Molecular Biology Reviews, 89*(1), e00016-23. https://doi.org/10.1128/mmbr.00016-23

Taves, M. D., Mittelstadt, P. R., Presman, D. M., Hager, G. L., & Ashwell, J. D. (2019). Single-cell resolution and quantitation of targeted glucocorticoid delivery in the thymus. *Cell Reports, 26*(13), 3629–3642.e4. https://doi.org/10.1016/j.celrep.2019.02.108

Tomris, I., Kimpel, A. L. M., Liang, R., van der Woude, R., Boons, G.-J. P. H., Li, Z., & de Vries, R. P. (2024). The HCoV-HKU1 N-terminal domain binds a wide range of 9-*O*-acetylated sialic acids presented on different glycan cores. *ACS Infectious Diseases, 10*(11), 3880–3890. https://doi.org/10.1021/acsinfecdis.4c00488

Tsai, Y.-X., Chien, Y.-C., Hsu, M.-F., Khoo, K.-H., & Hsu, S.-T. D. (2025). Molecular basis of host recognition of human coronavirus 229E. *Nature Communications, 16*(1), 2045. https://doi.org/10.1038/s41467-025-57359-8

Vabret, A., Dina, J., Gouarin, S., Petitjean, J., Corbet, S., & Freymuth, F. (2006). Detection of the new human coronavirus HKU1: A report of 6 cases. *Clinical Infectious Diseases, 42*(5), 634–639. https://doi.org/10.1086/500136

van der Hoek, L., Pyrc, K., & Berkhout, B. (2006). Human coronavirus NL63, a new respiratory virus. *FEMS Microbiology Reviews, 30*(5), 760–773. https://doi.org/10.1111/j.1574-6976.2006.00032.x

van der Hoek, L., Pyrc, K., Jebbink, M. F., Vermeulen-Oost, W., Berkhout, R. J. M., Wolthers, K. C., Wertheim-van Dillen, P. M. E., Kaandorp, J., Spaargaren, J., & Berkhout, B. (2004). Identification of a new human coronavirus. *Nature Medicine, 10*(4), 368–373. https://doi.org/10.1038/nm1024

Vieira, C., Nery, L., Martins, L., Jabour, L., Dias, R., & Simões e Silva, A. C. (2021). Downregulation of membrane-bound angiotensin converting enzyme 2 (ACE2) receptor has a pivotal role in COVID-19 immunopathology. *Current Drug Targets, 22*(3), 254–281. https://doi.org/10.2174/1389450121666201020154033

ViralZone. (n.d.). *Human coronavirus*. ExPASy Bioinformatics Resource Portal. Retrieved September 20, 2026, from https://viralzone.expasy.org/766?outline=all_by_species

Visser, E. A., Moons, S. J., Timmermans, S. B. P. E., de Jong, H., Boltje, T. J., & Büll, C. (2021). Sialic acid O-acetylation: From biosynthesis to roles in health and disease. *Journal of Biological Chemistry, 297*(2), Article 100906. https://doi.org/10.1016/j.jbc.2021.100906

Wang, Y., Li, P., Solanki, K., Li, Y., Ma, Z., Peppelenbosch, M. P., Baig, M. S., & Pan, Q. (2021). Viral polymerase binding and broad-spectrum antiviral activity of molnupiravir against human seasonal coronaviruses. *Virology, 564*, 33–38. https://doi.org/10.1016/j.virol.2021.09.009

Wang, Y., Shi, H., Rigolet, P., Wu, N., Zhu, L., Xi, X.-G., Vabret, A., Wang, X., & Wang, T. (2010). Nsp1 proteins of group I and SARS coronaviruses share structural and functional similarities. *Infection, Genetics and Evolution, 10*(7), 919–924. https://doi.org/10.1016/j.meegid.2010.05.014

Wells, D. A., Cantoni, D., Mayora-Neto, M., Di Genova, C., Sampson, A., Ferrari, M., Carnell, G., Nadesalingam, A., Smith, P., Chan, A., Raddi, G., Castillo-Olivares, J., Baxendale, H., Temperton, N., & Heeney, J. L. (2022). Human seasonal coronavirus neutralization and COVID-19 severity. *Journal of Medical Virology, 94*(10), 4820–4829. https://doi.org/10.1002/jmv.27937

Williams, T. L., Strachan, G., Macrae, R. G. C., Kuc, R. E., Nyimanu, D., Paterson, A. L., Sinha, S., Maguire, J. J., & Davenport, A. P. (2021). Differential expression in humans of the viral entry receptor ACE2 compared with the short deltaACE2 isoform lacking SARS-CoV-2 binding sites. *Scientific Reports, 11*(1), 24336. https://doi.org/10.1038/s41598-021-03731-9

Wilson, R., Kovacs, D., Crosby, M., & Ho, A. (2024). Global epidemiology and seasonality of human seasonal coronaviruses: A systematic review. *Open Forum Infectious Diseases, 11*(8), ofae418. https://doi.org/10.1093/ofid/ofae418

Xiao, T., Lu, J., Zhang, J., Johnson, R. I., McKay, L. G. A., Storm, N., Lavine, C. L., Peng, H., Cai, Y., Rits-Volloch, S., Lu, S., Quinlan, B. D., Farzan, M., Seaman, M. S., Griffiths, A., & Chen, B. (2021). A trimeric human angiotensin-converting enzyme 2 as an anti-SARS-CoV-2 agent. *Nature Structural & Molecular Biology, 28*(2), 202–209. https://doi.org/10.1038/s41594-020-00549-3

Yalcin, H. C., Sukumaran, V., Al-Ruweidi, M. K. A. A., & Shurbaji, S. (2021). Do changes in ACE-2 expression affect SARS-CoV-2 virulence and related complications: A closer look into membrane-bound and soluble forms. *International Journal of Molecular Sciences, 22*(13), 6703. https://doi.org/10.3390/ijms22136703

Ye, R.-Z., Gong, C., Cui, X.-M., Liu, J.-Y., Fan, H., Xie, H., Wang, Q., Ren, Z.-Y., Zhang, Y.-W., Xia, L.-Y., Zhang, M.-Z., Li, Y.-Y., Li, Z.-H., Du, L.-F., Zhang, J., Cheng, N., Shi, W., Li, M.-Z., Zhao, L., ... Cao, W.-C. (2023). Continuous evolution and emerging lineage of seasonal human coronaviruses: A multicenter surveillance study. *Journal of Medical Virology, 95*(6), e28861. https://doi.org/10.1002/jmv.28861

Ye, Z.-W., Yuan, S., Yuen, K.-S., Fung, S.-Y., Chan, C.-P., & Jin, D.-Y. (2020). Zoonotic origins of human coronaviruses. *International Journal of Biological Sciences, 16*(10), 1686–1697. https://doi.org/10.7150/ijbs.45472

Ye, Y., & Hogue, B. G. (2007). Role of the coronavirus E viroporin protein transmembrane domain in virus assembly. *Journal of Virology, 81*(7), 3597–3607. https://doi.org/10.1128/JVI.01472-06

Zhang, K., Li, S., Pintilie, G., Chmielewski, D., Schmid, M. F., Simmons, G., Jin, J., & Chiu, W. (2020). A 3.4-Å cryo-electron microscopy structure of the human coronavirus spike trimer computationally derived from vitrified NL63 virus particles. *QRB Discovery, 1*, e11. https://doi.org/10.1017/qrd.2020.16

Zhang, R., Wang, K., Lv, W., Yu, W., Xie, S., Xu, K., Schwarz, W., Xiong, S., & Sun, B. (2014). The ORF4a protein of human coronavirus 229E functions as a viroporin that regulates viral production. *Biochimica et Biophysica Acta (BBA) - Biomembranes, 1838*(4), 1088–1095. https://doi.org/10.1016/j.bbamem.2013.07.025

Zhao, X., Chen, D., Li, X., Griffith, L., Chang, J., An, P., & Guo, J.-T. (2022). Interferon control of human coronavirus infection and viral evasion: Mechanistic insights and implications for antiviral drug and vaccine development. *Journal of Molecular Biology, 434*(6), 167438. https://doi.org/10.1016/j.jmb.2021.167438

Zhuang, M.-W., Cheng, Y., Zhang, J., Jiang, X.-M., Wang, L., Deng, J., & Wang, P.-H. (2020). Increasing host cellular receptor—angiotensin-converting enzyme 2 expression by coronavirus may facilitate 2019-nCoV (or SARS-CoV-2) infection. *Journal of Medical Virology, 92*(11), 2693–2701. https://doi.org/10.1002/jmv.26139